UNIVERSITÀ DEGLI STUDI DI PALERMO

Dottorato in Energia e Tecnologie dell'Informazione
Dipartimento di Energia, Ingegneria dell'Informazione e Modelli Matematici
Settore Scientifico Disciplinare ING-INF/04

ROBUST AND MODEL PREDICTIVE CONTROL APPLIED TO DC/DC CONVERTERS AND SHUNT ACTIVE FILTERS

IL DOTTORE
Eng. ROBERTO RABBENI

IL COORDINATORE
Prof. MARIA STELLA MONGIOVI'

IL TUTOR
Prof. FRANCESCO ALONGE

CO-TUTOR
Prof. FILIPPO D'IPPOLITO

CO-TUTOR
Prof. GIANPAOLO VITALE
CNR-ISSIA UOS di Palermo

CO-TUTOR
Prof. MARCELLO PUCCI
CNR-ISSIA UOS di Palermo

CICLO XXIX
ANNO CONSEGUIMENTO TITOLO 2017

DOTTORATO

UNIVERSITÀ DEGLI STUDI DI PALERMO
Dottorato in Energia e Tecnologie dell'Informazione
Dipartimento di Energia, Ingegneria dell'Informazione e Modelli Matematici
Settore Scientifico Disciplinare ING-INF/04

ROBUST AND MODEL PREDICTIVE CONTROL APPLIED TO DC-DC CONVERTERS AND SHUNT ACTIVE FILTERS

IL DOTTORE
Eng. ROBERTO RABBENI

IL COORDINATORE
Prof. MARIA STELLA MONGIOVI'

IL TUTOR
Prof. FRANCESCO ALONGE

CO TUTOR
Prof. FILIPPO D'IPPOLITO

CO TUTOR
Prof. GIANPAOLO VITALE
CNR-ISSIA UOS di Palermo

CO TUTOR
Prof. MARCELLO PUCCI
CNR-ISSIA UOS di Palermo

CICLO XXIX.
ANNO CONSEGUIMENTO TITOLO 2017

Contents

List of Figures

List of Tables

Acknowledgments

Firstly, I would like to express my sincere gratitude to my supervisors, Prof. Francesco Alonge, Prof. Filippo D'Ippolito, Prof. Gianpaolo Vitale and Prof. Marcello Pucci, for their support and encouragements during my PhD. I owe them most of the successful results obtained in the past three years and my scientific and personal growth.

My gratitude is also due to all the other people of the research group of: the University of Palermo, Dr. Antonino Sferlazza and Eng. Stefania Maria Collura; the CNR ISSIA U.O.S Palermo, Dr. Massimiliano Luna, Lab.T. Giuseppe Scordato and Lab.T. Antonio Sauro; the University of Nottingham, Prof. Pericle Zanchetta, Dr. Alberto Gaeta, Dr. Andrea Formentini, Dr. Giovanni Lo Calzo and Eng. Luca Rovere; R&D Electrolux spa: Dr. Mariano Tartuferi, Eng. Marco Spada, Eng. Giorgio Pattarello, Eng. Davide Moscatelli, Eng. Marco Bossi and Eng. Paolo Posa. All of them have been a valuable source of suggestions and stimulus for my research activity, and dear friends.

I want to thank all the people met during these years. Somebody only for a short time, somebody else for a longer period but all have been a fundamental human value added to the experience of my PhD. A special mention goes to the friends of Palermo: Stefania, Stefano, Andrea, Antonino, Anna, Gioacchino, Luca; and of Nottingham: Geraldo and Luca.

Last but not the least, I would like to say thanks to the pillars of my family: my parents, Ignazio and Mariuccia; they have always spent precious time, words, and energies with love. Moreover, thanks to all my family for their support: my brother Francesco, my little nephew Riccardo; and finally, in name of all, my grandfather Damiano and Giuseppe…

For better or worse, what I am today is your merit…

Pordenone, December 2016

Abstract

Nowadays, the electricity demand increases day by day. People often use it with superficiality and underestimating how much it is valuable. Until a few decades ago, the power generation was centralized and depended on the exploitation of fossil resources. The finite nature of fossil fuels, along with the environmental effects of their exploitation, have brought the scientific community to find alternative energy sources less polluting and easily available. The development and dissemination of renewable energy sources have marked the end of a centralized electricity grid in favor of a distributed one, which allows: bi-directional power flows, priority dispatching of renewable sources, flattening of the load diagram, energy trade between micro smart-grids, active users in the production and management process.

In the generation of electrical energy from renewable sources is necessary the use of power electronic converters to adapt source and load needs. In fact, the sources have variable levels of voltage and current in dependence of the source and the weather conditions; the load instead requires a constant value of current or voltage even if it changes itself.

In the generation of electricity from fuel cells, photovoltaic and wind power, the step-up DC/DC converters are really important. In this class of direct current converters belong different circuit topologies which differ in: the number of components, the efficiency, the volume, the weight, the number of the switching elements, the reliability.

The interconnection between the elements that make up a given circuit topology determines the electrical characteristics of the system: the converter gain expressed as ratio of the output voltage and the input; the ripple of the input current; ripple of the output voltage. The characteristics of the power source are necessary to interface the converter that allows the optimal use and management of the source.

Generally, the step-up converter has an inductance which is connected in series with the source. This fact, for one hand ensures a reduction of the input current ripple and for another hand it is source of Joule losses due to its parasitic resistance, ESR. Anyway, the use of inductors with small parasitic resistance introduces control

system issues because it affects the static gain and its sensitivity to parameter variations.

In literature, there are different topologies of high-gain step-up converters which were not considered for technological reasons. The technology development has allowed and will allow, now and even more in the future, the presence of low-loss inductors in the market that will allow the design of converters with high-gain and efficiency (Yang et al. 2007), (Li & Lee 2012). With this fact, will be possible to review many topologies that have been discarded in the past.

In this thesis, the class of quadratic boost converters, QBC, it has been studied. More exactly, two new topologies of QBCs for fuel cells and photovoltaic or wind power have been studied. Defined the principle of operation and the equations which allow to design the power stage, the mathematical model has been determined considering and comparing different modeling approaches.

The mathematical model of the power stage has been determined using a classical (Middlebrook & Cuk 1976) and modern (Goebel et al. 2009) circuit oriented control system approach and a black-box approach by nonlinear parameter identification techniques (Haber & Keviczky 2012; Haber & Keviczky 1999). The mathematical model of the converters has been used for the tuning of linear and robust controllers in order to face up with the parametric and modeling uncertainty.

In order to improve the power quality in the case of grid-connected applications, it is analyzed an active filter which is controlled using finite state model predictive control and a new finite state model predictive control technique with control signal modulation.

Abstract

Al giorno d'oggi, la domanda di energia elettrica incrementa giorno per giorno. La gente spesso la usa con superficialità sottovalutando quanto essa sia preziosa. Fino a qualche decennio fa, la generazione di energia elettrica era centralizzata e dipendeva dallo sfruttamento delle risorse fossili. La limitatezza delle fonti fossili, insieme agli effetti ambientali del loro sfruttamento, hanno portato la ricerca a trovare vettori energetici alternativi poco inquinanti e facilmente reperibili. Lo sviluppo e la diffusione delle fonti energetiche rinnovabili hanno sancito la fine di una rete elettrica centralizzata a favore di una nuova idea di rete elettrica di tipo distribuita che permette di avere: flussi di potenza bidirezionali, priorità di dispacciamento delle fonti rinnovabili, appiattimento del diagramma di carico, scambi energetici tra le micro smart-grid, utilizzatori attivi nel processo di produzione e gestione.

Nella generazione di energia elettrica da fonti rinnovabili è necessario l'uso di convertitori elettronici di potenza per adattare le esigenze della sorgente a quelle del carico. Infatti, le sorgenti presentano livelli di tensione e corrente variabili in dipendenza della tipologia stessa ma anche dalle condizioni meteo-climatiche; di contro, il carico richiede livelli di tensione o corrente costanti a fronte di variazioni anche brusche del carico stesso.

Nell'ambito delle generazione di energia elettrica da celle a combustibile, impianti fotovoltaici ed eolici, grande importanza rivestono i convertitori elettronici di potenza dc/dc di tipo elevatore. A questa categorie di convertitori a corrente continua appartengono diverse topologie circuitali che differiscono per il numero di componenti, l'efficienza, il volume, il peso, il numero degli elementi di commutazione, l'affidabilità.

L'interconnessione tra gli elementi che costituiscono una data topologia circuitale determina inoltre le caratteristiche elettriche del sistema: guadagno del convertitore espresso come rapporto tra la tensione d'uscita e quella d'ingresso; ondulazione della corrente d’ingresso; ondulazione della tensione d'uscita. Note le caratteristiche della sorgente elettrica, è necessario interfacciare il convertitore che consente l'uso e la gestione ottimale della fonte stessa.

I convertitori innalzatori presentano generalmente un'induttanza, connessa in serie con la sorgente, che da un lato assicura una riduzione delle ondulazioni della corrente d'ingresso e dall'altro è fonte di perdite Joule a causa della sua resistenza parassita, ESR. L'utilizzo d'induttori con resistenza parassita piccola tuttavia introduce delle problematiche relative al controllo del convertitore stesso poiché influenza il guadagno statico e la sua sensibilità rispetto alle variazioni parametriche.

Esistono diverse topologie di convertitori elevatori ad elevato guadagno che per motivi tecnologici in passato non sono stati considerati. Lo sviluppo tecnologico ha permesso e permetterà, oggi e ancora di più nel futuro, la presenza nel mercato di induttori aventi basse perdite (Yang et al. 2007), (Li & Lee 2012) che consentiranno di progettare convertitori ad elevati guadagni ed efficienza, e di riconsiderare molte topologie che in passato sono state abbandonate.

In questo lavoro di tesi è stato approfondito lo studio della classe dei convertitori dc/dc elevatori quadratici. In particolare sono state studiate due nuove topologie che presentano caratteristiche differenti e trovano applicazione nella generazione di energia da celle a combustibile e da impianti fotovoltaici/eolici. Definito il principio di funzionamento e le equazioni che consentono il progetto dello stadio di potenza è stato determinato il modello matematico valutando e confrontando diversi approcci di modellazione.

Il modello matematico dello stadio di potenza è stato determinato seguendo un approccio sistemistico classico (Middlebrook & Cuk 1976) e moderno (Goebel et al. 2009) orientato al circuito e, attraverso tecniche di identificazione parametrica non lineare (Haber & Keviczky 2012; Haber & Keviczky 1999). Il modello matematico dei convertitori è stato utilizzato per la sintesi di controllori lineari classici e di tipo robusto per contrastare l'incertezza parametrica e di modellazione del sistema.

Al fine di migliorare la qualità della potenza iniettata in rete nel caso di impianti connessi alla rete, viene analizzato il controllo di un filtro attivo mediante controllo predittivo a stati finiti e una innovativa tecnica di controllo predittivo a stati finiti con modulazione del segnale di commando.

Chapter 1

Introduction

1.1. Introduction to power converters

Power electronics converters are circuits used in the conversion, control and conditioning of the electric power. They convert the power flow between two systems by changing the electrical parameters. Reliability, efficiency, size and cost are the most important features of the power electronic converters because they have to be robust and efficient in the higher useful time, small and lightweight in order to improve the power density.

Among all power converters, the most efficiency technology is the switched-mode power converters (Pressman 1997; Mohan et al. 1995; Robert W. 2002). In these converters, the power is controlled by controlling the "on" and "off" timing of the switching devices.

The most common classification of the power electronic converters is based on the waveform of the input and output signals. Therefore, in the case whether they are direct current, DC, or alternating current, AC, there are:

- DC/DC converters;
- DC/AC converters (inverters);
- AC/DC converters (rectifiers);
- AC/AC converters (transformers and cycloconverters).

At the same time, the power devices within the converters can be switched at the line frequency, *naturally commutated converters*, or per high-frequency switching, *forced-commutated converters*. Moreover, there is another classification based on the character of the input source, *voltage-source converters* or *current-source converters*.

In this thesis only the static conversion with semiconductor power devices is analyzed. The efficiency of these converters is high because they work in switching-mode. Nowadays, these devices are based on the mature Silicon technology.

However, silicon exhibits some important limitations regarding its switching frequency, operation temperature, voltage blocking capability. A new generation of power devices is required in applications where Si power devices cannot operate. It is worldwide accepted today that the use of the novel and innovative Wide Band Gap, WBG, semiconductor devices can play a main role in energy efficient systems because the allow operation at high-switching speed, high-voltage and high temperature (Millán et al. 2012). WBG semiconductors such as SiC, GaN and diamond show better material properties than silicon. The diamond exhibits the best properties of all the WBG semiconductors. Nevertheless, there are critical problems related with the crystal growth and there is not a diamond power device in the market. GaN and SiC are the main WBG materials candidates to replace silicon in the next generation and they are already competing in the semiconductor market with Si devices. Currently, there is a sort of competition between SiC and GaN in a battle of performances versus cost. Anyway, academics and industrial are agree in considering that both will find their respective application fields (Coffa et al. 2016).

These novel devices represent a real breakthrough in the power device market. Moreover, the development of modeling and electro-thermal characterization tools of these devices, the design of their packaging, drivers and controllers need a great research effort and they represent a world-class innovation.

1.2. DC/DC converters

DC/DC converters are electronic circuits that change a voltage coming from a DC source into another DC signal with different properties. Nowadays, they have several applications in different civil and industrial fields.

In distributed power architecture systems because they are more efficiency and reliability compared to a central multiple outputs supply.

The simplest way to obtain a DC voltage by a DC source consists on using a voltage divider but it presents: a very poor efficiency, an output voltage that depends on the load, and a DC voltage always less than the input voltage. Another way consists on using a linear regulator. Also in this case, the output voltage is lower than the input one because it is obtained subtracted a voltage to the input generator by means a

power BJT ($V_{OUT} = V_{IN} - V_{CE}$, where V_{CE} is the collector to emitter voltage). In order to obtain the desired output voltage, the base voltage of the BJT is usually derived by stable negative feedback action. These kinds of circuits are used only for low power applications because the efficiency is low. All the power supplied by the source that is not utilized by the load have to be dissipated by the power BJT.

The switching regulators are circuits that use a power switch, an inductor and a diode to transfer energy from an input to an output. The power switch works in switching mode, it means that only two fundamental states are present: the *on* state and the *off* state. During the *on* state the voltage of the power switch is null and its current is imposed by the external circuitry. During the *off* state, on the contrary, the current is null and the voltage of the power switch is imposed by the external devices. With this approach, a dissipated power in the power switch is present only during the transitions between the *on* state and the *off* state. During these transitions the product voltage per current is not null because the power switch is not ideal and a time is required to pass from a status to the other one.

The inductor's main function is to limit the current slew rate of the power switch that otherwise would be limited by the switch resistance alone. The linear regulators, instead, use a resistive drop to regulate the voltage, losing power in the form of heat. In a switching regulator, the converter stores energy because the inductor voltage drop is associated to a current that is 90 degrees late. This energy E is equal to $\frac{1}{2}LI^2$ and can be recovered during the discharging phase of the switching cycle.

The basic components of the DC/DC switching regulator can be rearranged to form a buck converter (step-down), a boost converter (step-up), a buck-boost converter (inverting topology), see from Figure 1 to Figure 3. All of these topologies are non-isolated. Starting from the non-isolated topologies, it is possible obtain the isolated topologies adding a transformer or a mutual inductor.

The power switch pass from the *on* state to the *off* state periodically. This periodicity is called switching period, T_{sw}. The ratio between the time in which the switch is *on* and the switching period is the duty-cycle[1]. It represents the control input of the

[1] $D = \frac{T_{ON}}{T_{sw}}$ is the duty-cycle of a DC/DC switching converter.

conversion stage. By this input, the output voltage can be regulated in open and closed loop.

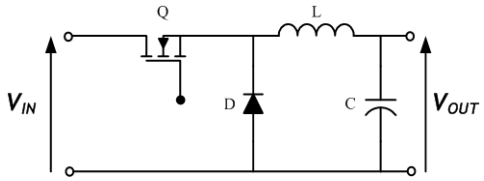

Figure 1 Buck topology.

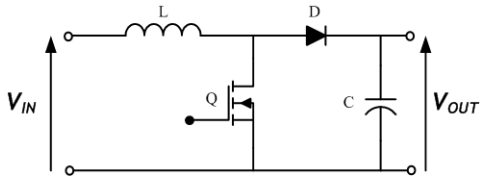

Figure 2 Boost topology.

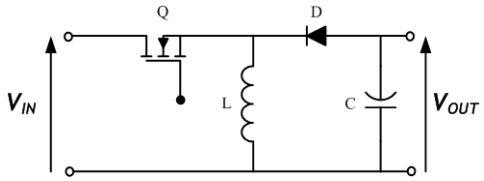

Figure 3 Buck-Boost topology.

All in all, DC/DC switching power supplies offer higher efficiency than traditional linear power supplies. They can step-up, step-down and invert the output voltage. Moreover, some topology can isolate the output voltage from the input by means a transformer. Although the switching converters have all these advantages, they can be noisy and require a control loop for the energy management. Furthermore the DC/DC conversion implies the generation of harmonic that are not present in the supply. Because of this, for low power and less expensive solutions, the linear regulators are used because they have a simple structure, a lower noise and a higher bandwidth.

The feedback and control circuits of the switching converters can be nested around these non-linear circuits to regulate the energy transfer and maintain a constant output within normal operating conditions.

1.3. DC/DC Boost converter

The DC/DC Boost converter allows to step-up the DC input power supply. In this topology the voltage generator is always connected in series to the inductor that store and release energy. The inductor imposes a smooth input current of the generator and it is connected, periodically, to the zero voltage reference by a power switch and to the load by a diode. The capacitor has a filter function of the output voltage. The circuit of the ideal DC/DC Boost converter is shown in Figure 4.

Under the assumption that the convert is ideal[2] and the current of the inductor is always greater than or equal to zero, the Boost converter works in the so called continuous conduction mode, CCM. This operation mode depends from the size of the electric tank, the inductor.

In CCM, when the power switch is in conduction, the diode is reverse biased and the load is supplied only by the capacitor (*on* state). On the contrary, when the switch is turned off, the voltage source supplies the inductor and the load by means the diode (*off* state). The two equivalent circuits of the Boost converter are shown in Figure 5 and Figure 6.

In CCM, the inductor voltage is defined by:

$$v_L = \begin{cases} V_{IN} & \text{during } T_{ON} \\ V_{IN} - V_{OUT} & \text{during } T_{OFF} \end{cases} \quad (1)$$

where T_{ON} is the time in which the power switch is turned on, T_{OFF} is the time in which it is turned off. The sum of the two times is always equal to the switching period, T_{sw} Using the fundamental relationship of the inductor, $v_L = L\dot{i_L}$, it is possible draw the inductor current trend. More exactly, during T_{ON} the current increase linearly with slope V_{IN}/L (the inductor store energy, $E > 0$); during T_{OFF} the inductor current linearly decrease with slope $(V_{IN} - V_{OUT})/L$ because in a step-up converter the output voltage is greater than input one. During this phase the inductor energy is less than zero so the inductor discharges the previous stored energy. Moreover, it should be noted that the mean current of the inductance corresponds to the input current.

[2] A converter is ideal when the input power is always equal to the output power. It means that all the components of the converter are ideals (power switches, diodes, inductors, capacitors) and so the efficiency is always 100%.

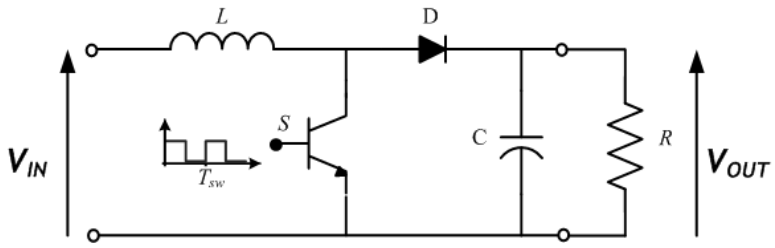

Figure 4 *Boost converter.*

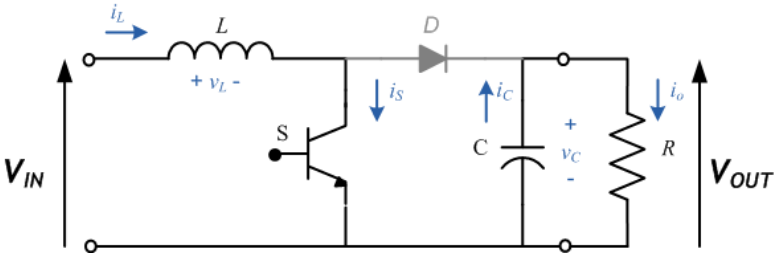

Figure 5 *Boost converter during on state.*

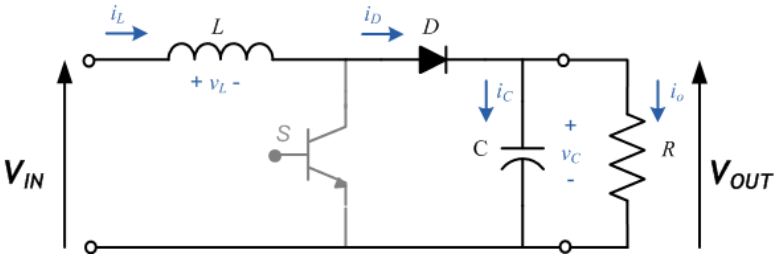

Figure 6 *Boost converter during off state.*

The conversion ratio *M* of the boost converter can be obtained by considering that, at steady-state, the average voltage of the inductor is null ($i_L(k) = i_L(kT_{sw})$ with $k \epsilon \mathbb{Z}^+$):

$$\frac{V_{IN} T_{ON}}{T_{sw}} = \frac{(V_{IN} - V_{OUT}) T_{OFF}}{T_{sw}} \tag{2}$$

From which:

$$M = \frac{V_{OUT}}{V_{IN}} = \frac{1}{1 - D} \tag{3}$$

For an ideal converter, the ratio between the input and output current is given by:

$$\frac{I_{OUT}}{I_{IN}} = 1 - D \tag{4}$$

From eq. (4) it is possible evaluate the input current as function of the input voltage supply and the duty-cycle as following:

$$I_{IN} = I_L = \frac{V_{IN}}{R(1-D)^2} \tag{5}$$

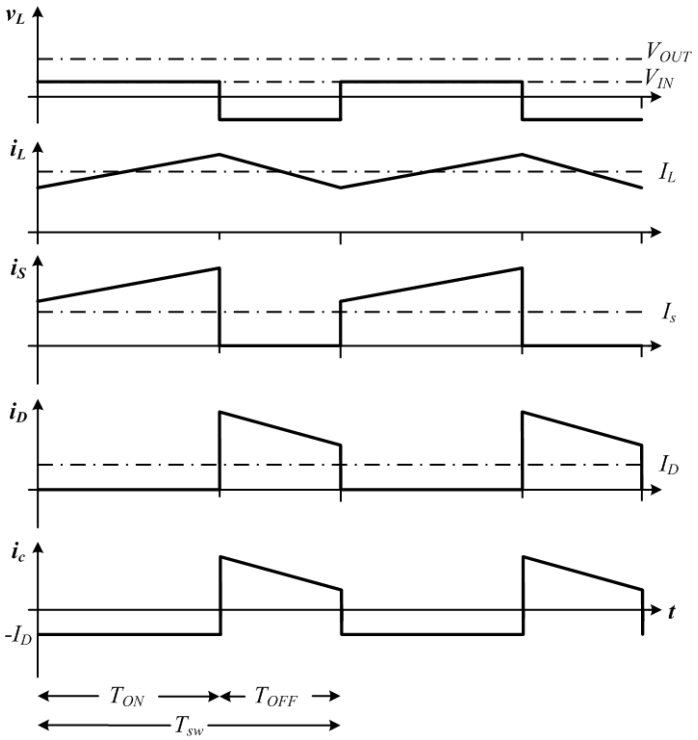

Figure 7 Time domain waveforms of the Boost in CCM: inductor voltage, inductor current, power switch current, diode current, and capacitor current.

The diode and switch current can be obtained from the knowledge of the inductor current:

$$i_S = \begin{cases} i_L & \text{during } T_{ON} \\ 0 & \text{during } T_{OFF} \end{cases} \tag{6}$$

$$i_D = \begin{cases} 0 & \text{during } T_{ON} \\ i_L & \text{during } T_{OFF} \end{cases} \tag{7}$$

Assuming that the capacitive impedance is much lower than the load one, all the ripple current of the diode flows through the capacitor meanwhile the average value through the load. In conclusion, the output current of the Boost converter is equal to the average value of the diode current and the capacitor current has the same waveform of the diode current with a null average value. By the knowledge of the capacitor current, integrating, it is possible obtain the trend of the output voltage.

The output voltage ripple can be calculated by the charge variation in the capacitor:

$$\Delta V_{OUT} = \frac{\Delta Q}{C} = \frac{I_{OUT} T_{ON}}{C} = \frac{V_{OUT}}{R} \frac{D}{C f_{sw}} \quad (8)$$

It depends on the load value, linearly by the duty-cycle, the capacitor tank and the switching frequency.

The peak to peak inductor current, Δi_L, can be evaluated by integrating the inductor equation during T_{ON}:

$$\Delta i_L = \frac{V_{IN}}{L} T_{ON} = \frac{V_{IN}}{L} \frac{D}{f_{sw}} \quad (9)$$

It should be noted that the current ripple depends by the inductor tank and the switching frequency. The entity of the current ripple defines the operating mode of the converter: continuous conduction mode (CCM), boundary conduction mode (BCM) and discontinuous conduction mode (DCM), see Figure 8.

In discontinuous mode, during T_{OFF} there are two equivalent circuits, see Figure 9. The converter switches between these two equivalent circuits at the time t^* where the inductor current become null. For $T_{ON} < t < t^*$ the time domain waveforms of the Boost converter are equivalents to the waveforms in CCM. Instead, for $t^* < t < T_{sw}$ the time domain trends of the converter are different because the inductance stored energy is null and the current is null as well. In this configuration the load is supplied only by the capacitor because the diode current is null.

In Figure 8, it should be noted that for the same switching frequency and average inductor current, I_L, the operating mode depends on the inductor ($L_{CCM} > L_{BCM} > L_{DCM}$). The mathematical inequality, that ensures at least a BCM, is given by:

$$I_{L,min} \geq \frac{\Delta i_L}{2} \quad (10)$$

From which:

$$\mathrm{L} \geq \frac{1}{2} \frac{V_{IN}}{I_{L,min}} \frac{D}{f_{sw}} \quad (11)$$

Where $I_{L,min}$ represents the minimum average value of the input current of the converter. Using eq. (5), the inductor inequality is given by:

$$\mathrm{L} \geq \frac{1}{2} \frac{R}{f_{sw}} \mathrm{D}(1 - D)^2 \quad (12)$$

Defining the design constant K equal to $\frac{2L}{RT_{sw}}$, it is possible rewrite the equation (12) as follow:

$$\mathrm{K} \geq \mathrm{D}(1-D)^{2} = k(D) \qquad (13)$$

The analysis of the function $k(D)$ is useful to design the power inductor because, if we know the maximum point of the function, we can choice the inductor that ensures the CCM in all the range of duty-cycle. The maximum point of the function $k(D)$ is equal to 4/27 for duty-cycle equals to 1/3.

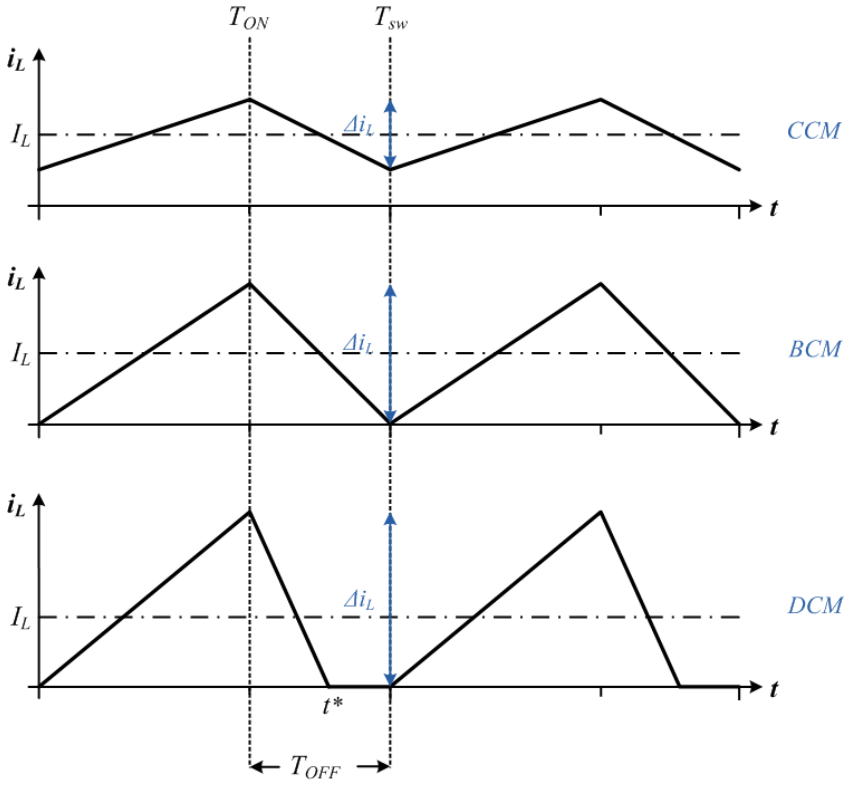

Figure 8 Time domain waveform of the inductor current: CCM, BCM, DCM.

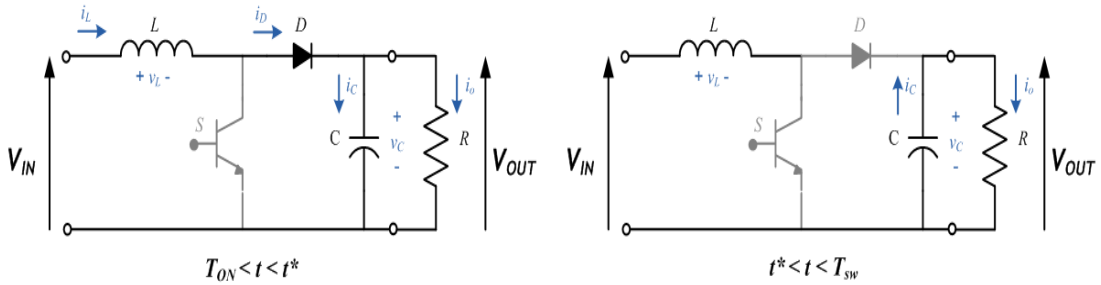

Figure 9 Equivalent circuits of the Boost converter during T_{OFF} in DCM.

1.4. DC/DC Boost Applications

Nowadays, with the higher attention to green technologies, the liberalization of the electricity market, and the increasing power demand, the power system infrastructure evolves toward a smart-grid. This phenomena is partially due to the penetration of Distributed Generation (DG) systems into the electrical grid (Püttgen et al. 2003; Malinowski et al. 2015; Ramakumar & Chiradeja 2002; Blaabjerg et al. 2015; Blaabjerg et al. 2006). DG technologies can be divided into renewable or RES (Renewable Energy Sources) such as solar (photovoltaic (PV) or thermal), wind, geothermal, ocean, and non-renewable such as internal combustion engines, combustion turbines, combined cycle systems, micro turbines and fuel cells (FCs), (Püttgen et al. 2003). In the last years the use of DG systems is increasing as results of many benefits that these technologies may offer in terms of infrastructure reliability and flexibility, reduction of the pollution and the transmission losses.

Power electronics plays a key role in the generation-storage-distribution cycle of the electric energy. This is because the generated electric energy is consumed after undergoing several transformations. Figure 10 shows a typical power electronic system consisting of a power converter, a load/source and a control unit. The power converter is the interface between the load/generator and the grid. The power flow is bidirectional and it depends on the topology and the applications.

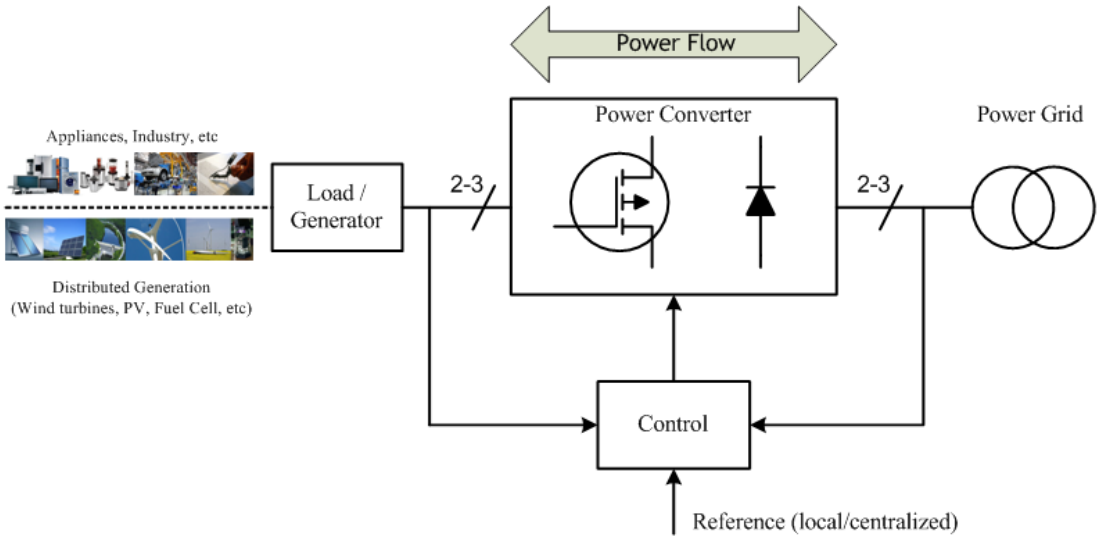

Figure 10 Power electronic system with the grid, load/source, power converter and control.

In this architecture there are three important issues. The first one is the reliability, the second is the efficiency and the third one is the cost of the power electronic system. For the moment the cost of the power semiconductor devices is decreasing from 1 to 5% every day for the same performance and price per KW. As result, the power electronics conversion is shrinking in volume and weight As result, the power electronics conversion is shrinking in volume and weight and finally in cost thanks to the national incentives. The key driver of this development is that the power electronics technology is still in progress. The only power device which is not under development is the silicon devices because better performance can be achieve with wide band-gap semiconductor devices such as the silicon carbide and the gallium nitride.

In the distributed generation, the class of DC/DC boost converters is present essentially in the:

- Wind energy conversion, WEC;
- Solar energy power conversion, SEPC;
- Fuel cell conversion, FCC;
- Active Power Factor Correction, A-PFC;

1.4.1. Wind Energy Conversion

Wind turbines (WTs) capture energy from the wind by means aerodynamic blades and convert it to rotating mechanical power. The number of the blades of the rotor is usually three and the rotating axis can be horizontal or vertical. A gear-box or a multi-pole generator is typically used in a wind turbine to increase rotational speed from a low speed rotor to a higher speed electrical generator. Between the generator and the grid a power converter can be inserted. The possible technical solutions are many and it depends on the transmission, the machine type, the rotor type and the electrical output (ac with fixed frequency or dc).

In the last decades, five generations of wind turbines have been developed. In this development it was important make the system able to control and limit the converted mechanical power at higher wind speed because the power in the wind is proportional to the cube of the wind speed. The power saturation may be done either by stall control, active control or pitch control. In the stall control the blade position

is fixed but stall of the wind appears along the blade at higher wind speed. In the active stall instead, the blade angle is adjusted in order to create a stall condition along the blades. Finally, in the pitch control, the blades are turned out of the wind at higher wind speed.

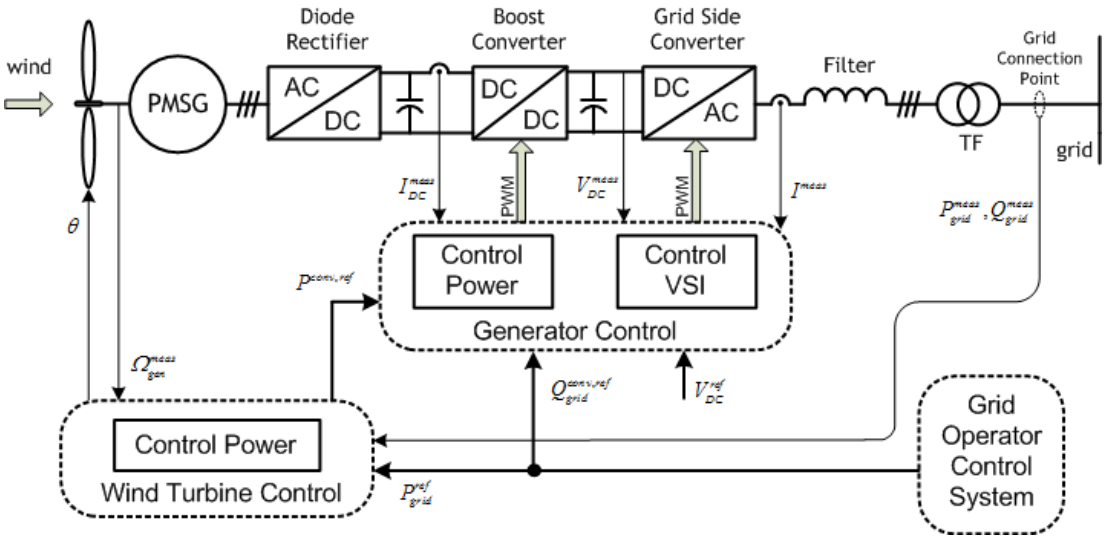

Figure 11 Control of active and reactive power in a wind turbine with multi-pole synchronous generator.

The performances of the WTs depend on the wind power harvest capability. The harvest of the wind energy is strictly linked to the used wind energy conversion technology. Referring to the rotation speed, WTs can be classified into:

- fixed speed;
- limited variable speed;
- variable speed.

In addition, referring to the drive transmission components, exist the following classification:

- geared-drive WTs;
- direct-drive WTs.

An overview and a comparison of the different wind generator systems is treated in (Li & Chen 2007).

The control of the WTs involves mechanical and electric dynamics. The power has to be controlled by means aerodynamic systems in relationship to the set-point given by

the dispatched center with the goal to maximize the power production. The power controller should also be able to limit the power.

Figure 11 shows a direct-drive variable speed solution able to control the active and reactive power in a WT. In the WEC system, the synchronous generator converts the mechanical energy into electrical energy but the voltage and frequency output vary along the wind speed change. In this technology architecture the passive rectifier and the boost converter are used to step-up the voltage at low speed. In order to achieve this task a boost converter with a higher conversion gain is desirable. Moreover the input dc current can be regulated by the Boost converter in order to follow the optimized current reference for the maximum power point operation of the wind turbine. The VSI is the grid side converter used to supply currents into the utility line. It is also used to power quality purpose. The active power, P, is controlled by q-axis whereas the reactive power, Q, can be controlled by d-axis current. The phase angle grid side is usually detected by software PLL (Phased Locked Loop) in d-q synchronous reference frame.

1.4.2. Solar Energy Power Conversion

In the last years, through the national incentives, the photovoltaic systems are gaining more and more visibility. With a continuous reduction of PV modules, DC/AC inverters, cables, fitting and manpower, the PV technology has the potential to become one of the main RES for the future electricity supply.

PV solar cells are basically semiconductor diodes which produce electrical power when exposed to sunlight and connected to a load. In this photogeneration step, the key parameter is the band gap energy of the semiconductor.

The lifetime of the PV cells is higher than 20/25 years because without any moving parts inside the tear and wear is very low. However, the aging of the power module produce a reduction of the power generation, 75/80 % of the rated power. A typical PV module is made up of around 36 or 72 cells connected in series and also encapsulated in structure made for example in aluminum and tedlar.

There are several kinds of PV technologies with different light to electricity efficiency (crystalline silicon, multi-crystalline silicon, amorphous silicon, thin-film, polymer solar cell). An overview of the photovoltaic materials with present

efficiencies and future challenges is treated in (Polman et al. 2016), an update efficiency table is instead shown in (Green et al. 2015). The reason to maintain a high level of research in new PV technologies is due to the fact that the microelectronic processes of high efficiency PV cells are still rather costly. The elementary PV cells are connected in series and parallel in order to make up a PV power module. The series/parallel connection gives a higher output voltage/current at the power module. PV fields are given by a set of series/parallel connected modules. The overall electrical characteristic of a PV fields is obtained by the composition of the electrical characteristics of its modules.

In a series connection the weakest cell/module determines the current seen at the power terminals. This weakest PV element can causes a reduction of the available power. The same drawback can be achieved with a non-ideal parallel connection under some operating or fault condition. In order to reduce possible mismatching in series and parallel connection bypass diode and block diodes are used in real PV configuration. The bypass diodes are used to guarantee a series connection whereas the block diodes, for each string, are used to avoid reverse current generated by other strings.

The PV current-voltage and power-voltage characteristics depend either on the solar irradiation and the PV cell temperature. Moreover the captured power is determined be the loading conditions.

A grid connected PV system is composed by a set of PV array, a power converter with a filter, a controller and finally the grid. The architecture of the PV system depends on its rated power. The most common structures for PV system are the central inverter, string inverter and module integrated inverter. In the central inverter structure there is a high efficiency and low cost VSI but with a single component the reliability of the plant is limited. Moreover the energy harvesting depends from module mismatching and partial shading conditions. In the string inverter configuration each PV string of the PV field is assigned to a *string inverter*. Every single string inverter has the capability to track the maximum power point of the string. In this way increase the reliability and the energy yield. An evolution of the string technology is the multi-string inverter. It allows the connection of several strings with separate MPPT (maximum power point tracking) via DC/DC Boost

converter and the presence of a common multi-string inverter. All in all, the module integrated inverter uses one inverter for each PV module. With this solution every module has a MPPT algorithm.

Figure 12 shows the PV inverter topology. The question of having a Boost converter or not is first of all related to the output voltage level of the PV string. Having more module and a lower grid voltage (120 V ac, 60 Hz) it is possible to avoid the boost function. The issue of the isolation is instead mainly related to safety standards and it is typically obtained using a transformer placed on the grid frequency side (LF) or on the high frequency side (HF). The isolation on the HF side is the more compact solution but high care should be taken in the transformer design in order to keep the losses low.

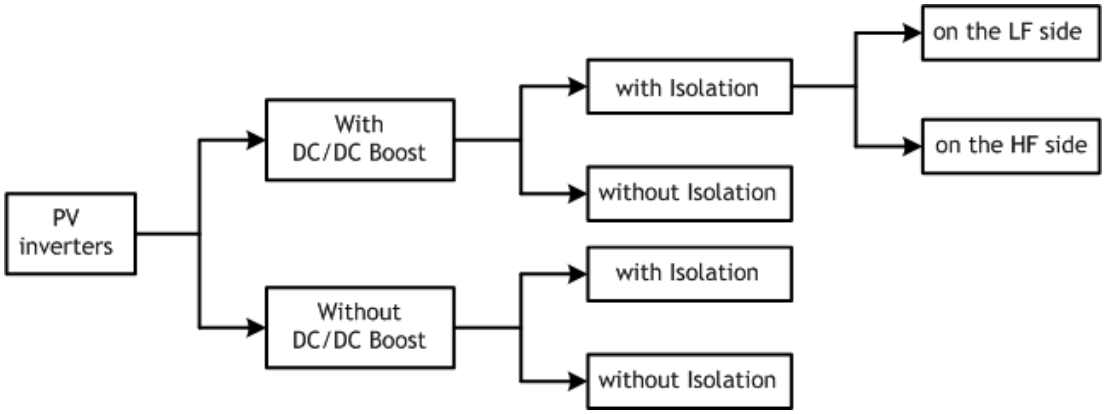

Figure 12 Power configurations for PV inverters.

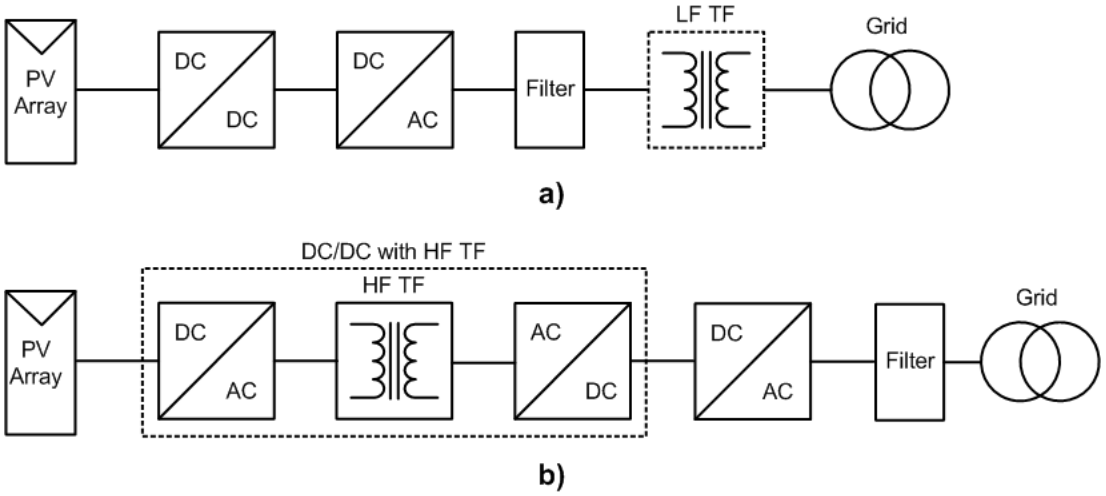

Figure 13 Power PV inverter topologies: a) PV system with or without LF transformer and boost convert; b) PV system with HF transformer.

In the PV inverters with DC/DC Boost converter is really important the gain of the converter especially when there are frequently partial shading condition in a string. Furthermore, if the converter has a high gain it is possible to reduce the number of the series modules and the MPPT procedure become easier.

1.4.3. Fuel Cell Conversion

The Fuel cell is a static device that converts chemical energy into electrical energy. Externally, at the power terminals, similarly to a battery system, the fuel cell produces power as long as fuel and oxidant are continuously fed. The FC systems are more reliability compared to diesel generator because there is not any moving part. Basically, FC consists of two electrodes, anode and cathode, separated by an electrolyte region. Usually, the fuel is the hydrogen and the oxidant is the oxygen. The fuel cells produce electricity directly by a chemical reaction that does not alter the electrodes and the electrolyte materials. If the fuel is pure hydrogen, water and heat are the only byproducts.

More exactly, the gaseous fuel is fed continuously to the anode (it is also the oxidant); the oxygen, from air, is fed to the cathode. When hydrogen is passes across the anode it is possible to separate hydrogen into electrons and protons. The electrons will pass through an external circuit as an electric current whereas the protons will go through the electrolyte. The electrons that come back from the external circuit with protons and oxygen produce water and heat.

A very complete overview of hydrogen FC systems is treated in (Sharaf & Orhan 2014); the state of art of FC technology for domestic built environment applications is discussed in (Elmer et al. 2015).

Even if there are many types of fuel cells, the proton exchange membrane (PEM) is the most promising technology for small-scale applications. The success of the PEM-FC is due to the fact that the operating temperature is low, the power density, the specific power, the longevity and the efficiency are high; and also the ability to adjust the electric power to the power demand is good.

Typically, in a FC the chemical reaction is given by:

$$H_2 + ½O_2 \rightarrow H_2O \tag{14}$$

The output voltage of the FC system is given as:

$$V_{cell} = E - \Delta V_{act} - \Delta V_{ohm} - \Delta V_{trans} \quad (15)$$

where E is the open circuit voltage, ΔV_{act} is the anode to cathode voltage drop, ΔV_{ohm} is the ohmic voltage drop resulting from the resistance of the electrolyte and the resistance of the electrodes; finally, ΔV_{trans} is the voltage drop resulting from the reduction of reactants gases. In (15) the open circuit voltage is given by the Nernst's equation which depends on the number of the cell connected in series in the stack. A detailed description of PEM-FC modeling can be found in (Uzunoglu & Alam 2007).

Similarly to the PV cells, the fuel cells are combined in a various series and parallel configurations to constitute a fuel cell system. The fuel cell system is connected to local utility system by means a power electronic DC/DC Boost converter. This power converter is mandatory because on the output terminals of a FC system there is a high current level and a low voltage level, see Figure 14. One of the main weak points of the fuel cell is its time constant dominated by the hydrogen controller (pumps, valves, compressors). For this reason, fast load demand will cause a high voltage drop in a short time (fuel starvation phenomena) that is harmful for the FC. As a consequent, a slope limitation ($A \cdot s^{-1}$) of the output current is necessary in order to guarantee a safe operating mode of the FC. Other safety conditions are: impose a unidirectional FC current and, keep the FC current within an interval (minimum value, rated value).

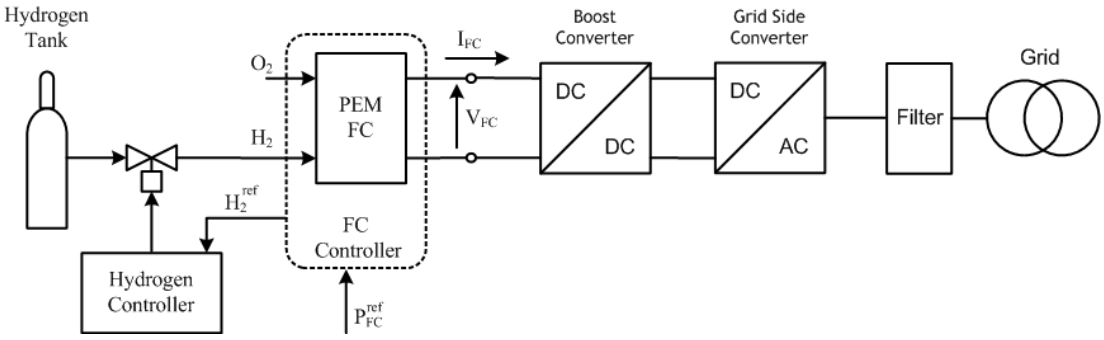

Figure 14 Fuel cell conversion system.

1.4.4. Active Power Factor Correction

AC/DC power conversion systems are widely used in several applications. Unfortunately, these non-linear systems introduce a harmonic distortion in the power

grid. It is well known that these unwanted harmonic currents cause several problems such as voltage distortion, heating, noise and reduce the capability of the line to provide energy.

In order to reduce the harmonic pollution and fulfill the strictly power quality standard, there are passive and active power factor correction (PFC). Passive solutions, typically LC filters, are cheaper and also they do not satisfy the EN 61000-3-2 standard for each load conditions. The active solutions, by means an electronic controller, can modify the shape of the input current proportionally to the grid voltage. In this way, it is possible to draw a sinusoidal input current perfectly in phase with the grid voltage. In (O.Garcia et al. 2001) there is classification and a comparison of several converters for AC/DC conversion with PFC. For high power level, these active PFC consist on a diode bridge rectifier followed by a step-up converter. Thanks to their high efficiency, the continuous conduction mode boost converter is the preferred topology for implementing a front end with power-factor correction (PFC). As a result, recently, significant efforts have been made to improve the dynamic performance (Alonge et al. 2015), the reverse-recovery characteristic of the boost rectifier (Huber et al. 2008; Choi et al. 2007) and also the electromagnetic compatibility (EMC) (Rossetto, Spiazzi, et al. 2000; Rossetto, Buso, et al. 2000).

1.5. Limits of the Boost converter

The ideal DC/DC Boost converter allows to step-up any DC input power supply to any desired output voltage following the equation (3). In the real life, the output to input conversion ratio is not an increasing monotone function because the power losses are always around the corner. The efficiency of a switching converter depends essentially on the conduction power losses and the switching power losses.

In the assumption that the power devices are ideals (the switching power losses are null) the equation (3) is given by:

$$M = \frac{V_{OUT}}{V_{IN}} = \frac{1}{(1-D) + \frac{r_C}{R} + \frac{r_L}{R}\frac{1}{(1-D)}} \tag{16}$$

Where r_C and r_L are respectively the parasitic resistances of the capacitor and the inductor, R is the ohmic load. Typically, the parasitic resistances $r_C$and r_L are much

less than the load. Therefore, basically, the static gain is influenced by the ratio $r_L/R(1-D)$, see Figure 15, and obviously by the power demand, see Figure 16.

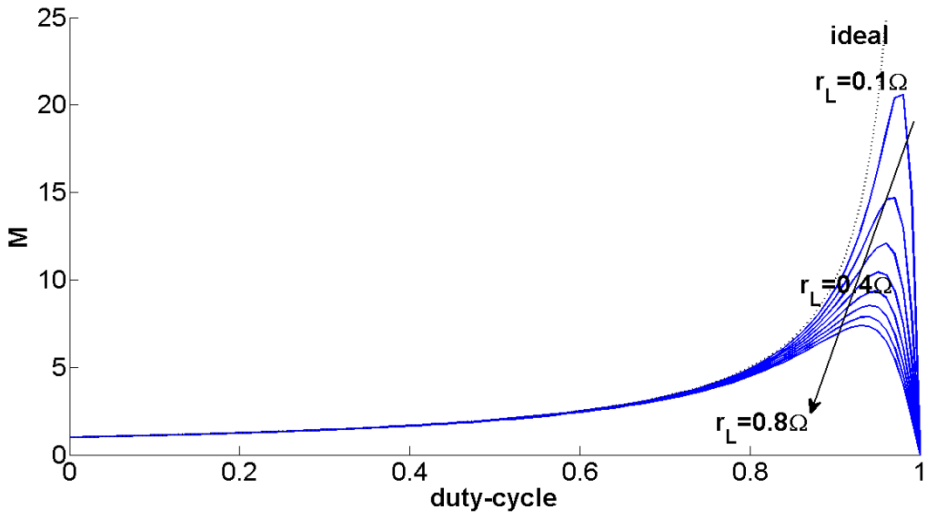

Figure 15 Ideal and real Boost converter conversion ratio versus r_L variations.

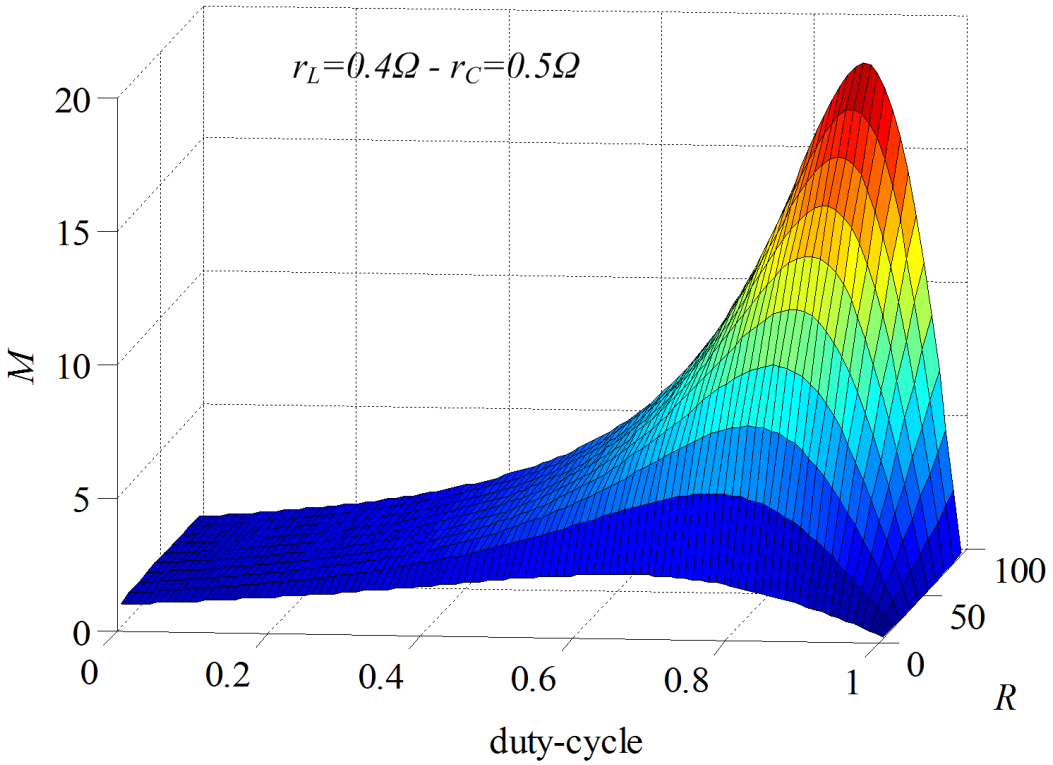

Figure 16 Real Boost converter conversion ratio versus load variations.

The analysis of the real gain, underline one limit of the Boost converter. It is not possible step-up an input voltage to any desired output voltage. Typically, for high

power demand the limit value of the conversion ratio is 5. In this limitation, the key component is the power inductor. In last year, significant efforts have been made to improve the Q-factor of the power inductor and the power density (Yang et al. 2007). In Figure 17 an example of a planar inductor. The exploded view shows that the spirals are made directly on the printed circuit board.

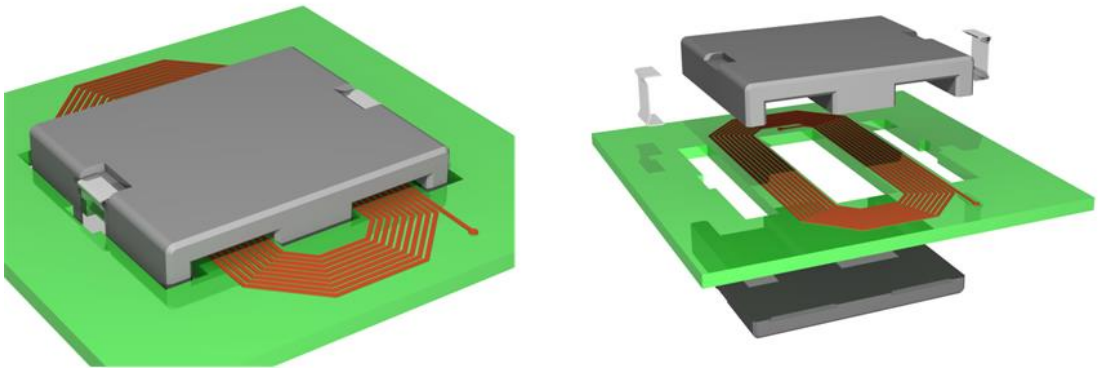

Figure 17 Example of planar inductor with printed circuit board spirals.

1.6. Conclusion

Distributed generation systems, in the last years, has increased the interest on power conversion circuits able to optimize the power transfer from the source to the load. As matter of fact, some sources as photovoltaic cells and fuel cells exhibit low voltages compared to those required by the input of the inverter stage. For this reason, among DC/DC converters, Boost topologies have attracted attention thanks to their inherent capacity to perform the maximum power point tracking. On the other hand, the traditional one-switch Boost converter reveals its limits for elevate value of boosting, since a high duty-cycle is needed. Anyway, it often cannot be adopted because of both the minimum off time of the power switch and the influence of the parasitic parameters.

Chapter 2

Quadratic Boost Converter

2.1. Introduction to the QBCs

In the conclusion of the first chapter has been stressed the importance of a high voltage boosting. In the development of high gain step-up converters, there are a lot of arrangements. For instance, Voltage Lift (VL) or Super Lift (SL) techniques are good methods to lift the output voltage of a DC-DC converter using capacitors and diodes (Zhang et al. 2012), (Bhaskar et al. 2014), (Fang Lin Luo & Hong Ye 2003), (Fang Lin Luo 2001). With these approaches the output voltage increases stage by stage along an arithmetic progression or geometric progression respectively. Super Lift technique increases the voltage transfer gain in geometric progression but the circuits, for increasing values of the gain, can become complex. Moreover using this technique the efficiency worsens because there are a lot of power diodes. Another class of converters are the switched component converters (Axelrod et al. 2008), Switched-Capacitor (SC) and Switched-Inductor (SI) (Bhaskar et al. 2014).

The current-fed full-bridge boost converters (Chen et al. 2010), (Arivazhagan & Prakash 2011) are very attractive in applications where there is a big difference between the input and the output voltages, such as: FCs, PV systems, and medical power supplies applications. They present high values of the gain because their structure consists of a boost converter plus a step-up transformer. The disadvantage of this category of converters lies in the presence of the transformer that increases the cost and the size, as well as the absence of a bulk capacitor connected to their transformer primary-side DC bus, suppressing high voltage overshoots and ringing across the switches.

The coupled inductors converters are attractive for their extremely high conversion ratio, due to the presence of coupled inductors (Ci-Ming Hong et al. 2009), (Chen et al. 2013). These converters are subjected to higher current stress on the switches and higher input current ripple than that of a conventional Boost converter.

The non-isolated single-switch topologies are very interesting solutions, since the transformer increases cost, volume and losses; and also the single-switch make the driver a simpler circuits and reduce the power losses. The Cascade Boost Converters (CBC) overcomes the drawbacks of the SL converters because they enhance the voltage transfer gain in power-law with a simple structure and a reduced number of diodes. In principle, a high voltage boosting could be achieved by the cascade connection of traditional Boost converters, see Figure 18 a). Anyway this solution lessens efficiency and requires more control loops.

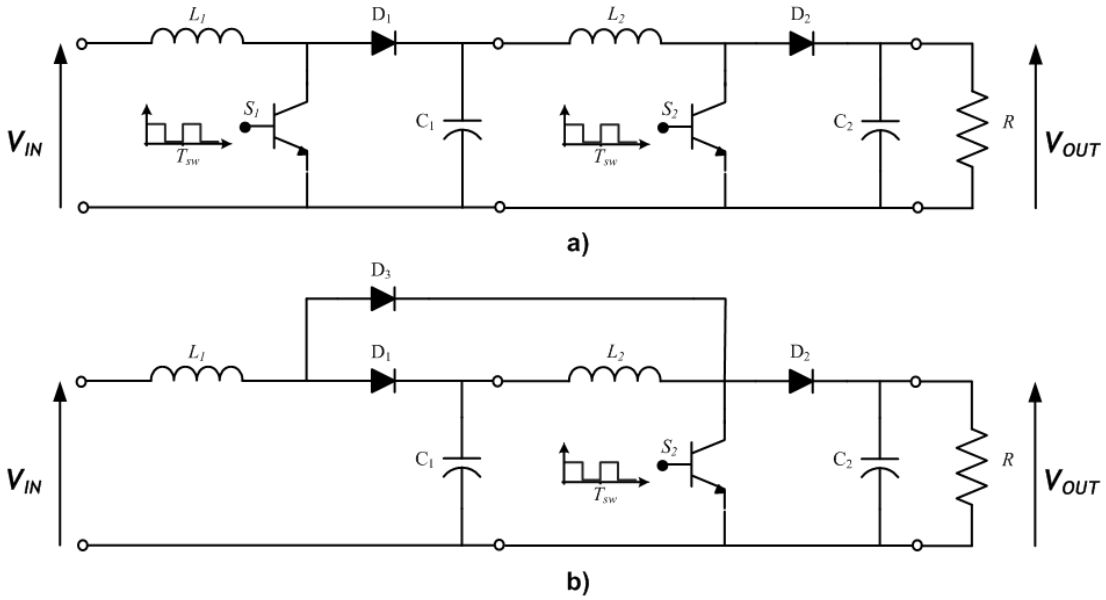

Figure 18 Quadratic Boost converter: a) double-switch (2nd order CBC) b) single-switch (classic QBC).

The Quadratic Boost Converters (QBCs) have a static gain equivalent to a second order CBC. The classic QBC can be obtained by cascading two traditional Boost converters in series and then eliminating redundant switches, see Figure 18 b). A comparison between the 2nd order CBC and the classic QBC is treated in (Choudhury & Byamakesh 2015). For the classic QBC: (Lopez-santos et al. 2016) defines the steady-state analysis of the four inductor conduction modes (DCL_1, DCL_2, DCL_{12}, DCL_{21}); (Leyva-Ramos et al. 2009) defines the ideal state space average model (non-linear and linear), the small-signal transfer function versus the duty-cycle of the output voltage and the two inductor currents, and also shows some experimental results about an analogic current mode controller; (Nava-Cruz et al.

2016) shows a comparative study of two Lyapunov controllers (complete state controller and partial state controller) with a load observer(Nava-cruz et al. 2015).

In literature, different step-up converter topologies belonging to the class of the quadratic Boost converters exist (de Novaes et al. 2007; Kadri et al. 2010; Yang et al. 2012). Typically, power electronic researchers propose QBC topologies with or without supplementary circuits used to improve the conversion gain. For instance, (Saadat & Abbaszadeh 2016) proposes a quadratic Boost converter with a coupler inductor and a switch capacitor cell, see Figure 19. In this topology, in CCM, the input to output conversion ratio is equal to:

$$M = \frac{n(3D+2)+(2-D)}{2(1-D)^2} \tag{17}$$

where n is the turn ratio (N_s/N_p) and the coupling coefficient is unitary. (Zhang et al. 2015) proposes instead a QBC with coupler inductor and a voltage multiplier, see Figure 20. In this case, in ideal condition and continuous conduction mode, the static gain is given by:

$$M = \frac{n+2}{(1-D)^2} \tag{18}$$

(Lee et al. 2013) presents another topology of QBC with an active snubber (S_2 and C_s) in order to perform a zero-voltage switching on the low voltage side of the coupled inductor. In this converter the front stage is composed by the inductor L_{i1}, the two diodes (D_{i1} and D_{i2}), the capacitor C_i and the power switch. The second stage is constructed using a charge pump Boost and a Flyback conversion scheme; see Figure 21 a). The clamping capacitor C_c can be reconstructed using multiple switched-capacitor cells, see Figure 21 b). In CCM and ideal condition the output voltage conversion ratio is the following:

$$M = \frac{(m+1)+(n+1)D}{(1-D)^2} \tag{19}$$

where m is the number of the switched capacitor cells.

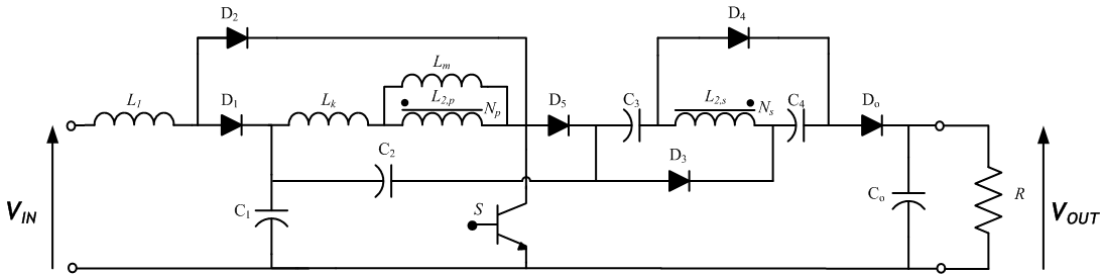

Figure 19 Quadratic Boost converter with coupler inductor and switched capacitor.

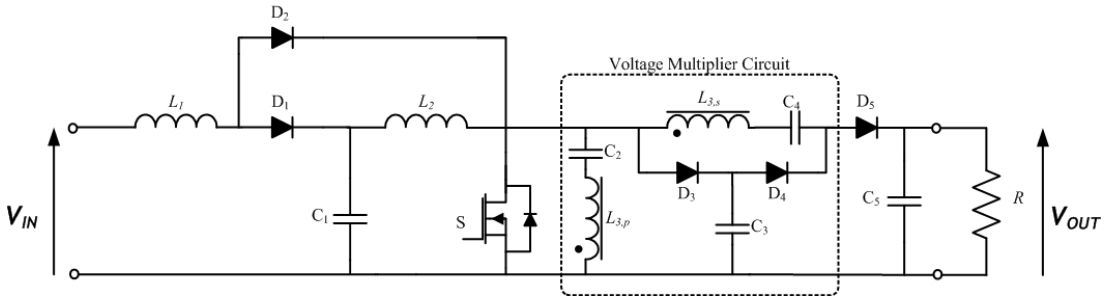

Figure 20 Quadratic Boost converter with coupler inductor and voltage multiplier circuit.

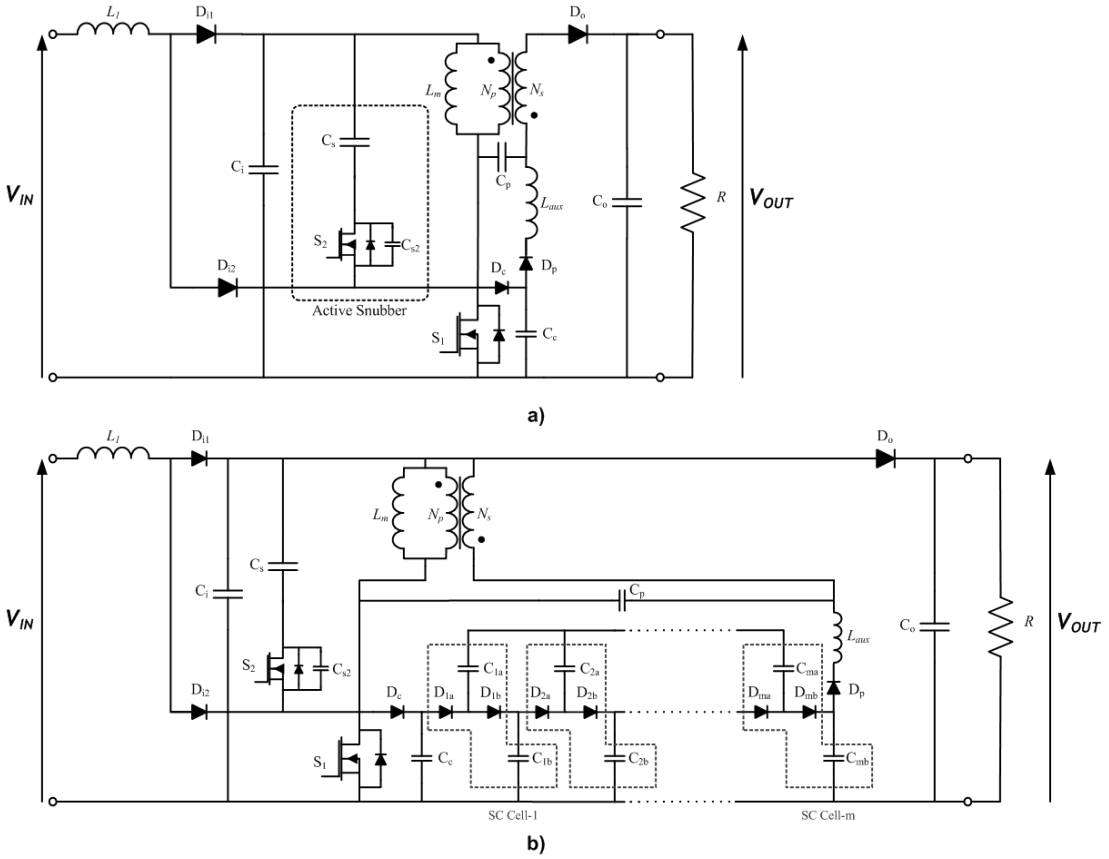

Figure 21 Quadratic Boost converter: a) QBC with coupler inductor b) QBC with coupler inductor and *m* switched capacitor cells.

This chapter introduces two transformer-less and single-switch topologies of Quadratic Boost converter: *QBC1* and *QBC2*. The two QBCs are been treated in a basic configuration, but obviously it is possible use techniques such as the switched capacitors or voltage multiplier in order to step-up even more the static gain. The *QBC1* topology have been proposed for the first time in the scientific literature by the author in (Rabbeni et al. 2011). The *QBC2* topology has been proposed in (Gaubert & Chanedeau 2009) but the scientific knowledge is really poor. In the author opinion, it is important understand the potentiality of these QBCs and so their industrial applications.

2.2. QBC1

The electric scheme of the *QBC1* is shown in Figure 22. This topology presents two inductors, two capacitors, four power diodes and a single power switch. The *QBC1* is derived from two stage of Boost converter in which the second is supplied by the output voltage of the first one. Furthermore, the output voltage of the second stage is added to the output of the first one. In this way, it is possible obtain a quadratic conversion ratio. The two elementary stages of the *QBC1* are shown in Figure 23 a) and b); in Figure 23 c) and d) are respectively shown the *QBC1* double-switch and single-switch.

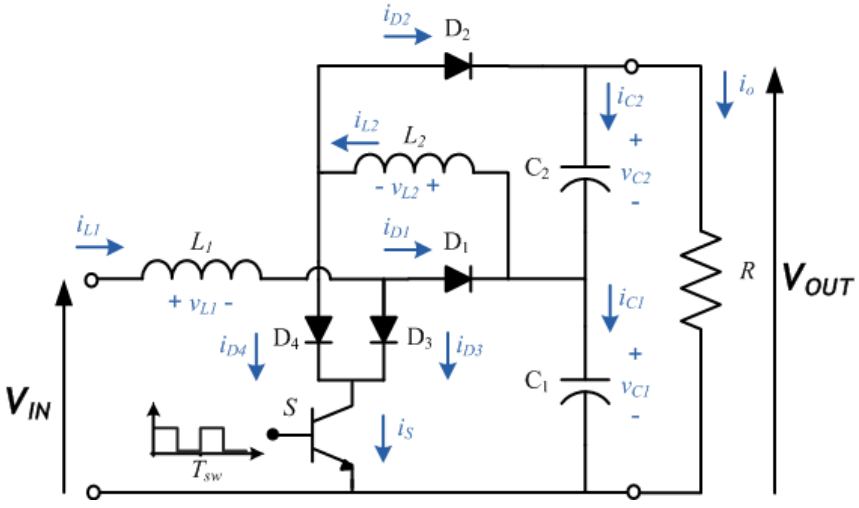

Figure 22 Electric scheme of the ideal *QBC1*.

Using the operating principle of the traditional Boost and the circuits of Figure 23, it is possible to obtain the CCM time domain waveforms of the *QBC1*, see Figure 24. In ideal conditions and a continuous conduction mode operation, as the traditional Boost converter, the *QBC1* is described by two topological circuits. The inductor voltages are defined by:

$$v_{L1} = \begin{cases} V_{IN} & \text{during } T_{ON} \\ V_{IN} - V_{C1} & \text{during } T_{OFF} \end{cases} \tag{20}$$

$$v_{L2} = \begin{cases} V_{C1} & \text{during } T_{ON} \\ V_{C1} - V_{OUT} = -V_{C2} & \text{during } T_{OFF} \end{cases} \tag{21}$$

Using the fundamental relationship of the inductor, it is possible to draw the inductor current trends. More exactly, during T_{ON} the currents increase linearly with slopes V_{IN}/L_1 and V_{C1}/L_2 (the two inductors store energy, $E > 0$); during T_{OFF} the inductor currents linearly decrease with slopes $(V_{IN} - V_{C1})/L$ and $-V_{C2}/L$ because in the two step-up stages the output voltage is greater than input one. During this phase the inductors energy is less than zero so the two inductors discharge the previous stored energy. Moreover, it should be noted that the mean current of the first inductance corresponds to the input current.

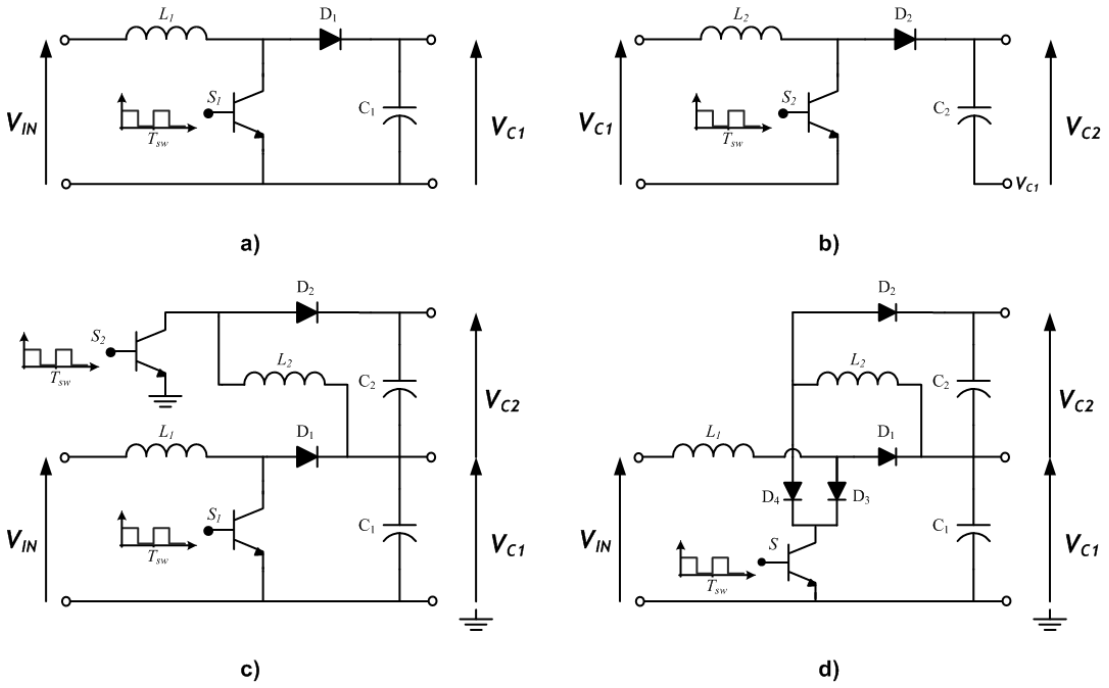

Figure 23 Quadratic Boost converter *QBC1* step by step: a) first stage of the *QBC1*; b) second stage of the *QBC1*; c) double-switch *QBC1*; d) single-switch *QBC1*.

The voltage average value of the capacitor C_1 can be obtained by considering that, at steady-state, the average voltage of the first inductor is null:

$$V_{C1} = \frac{V_{IN}}{(1-D)} \tag{22}$$

Similarly for the capacitor C_2, using equation (22), the C_2 average value is given by:

$$V_{C2} = \frac{V_{IN} D}{(1-D)^2} \tag{23}$$

The output voltage is given by the sum of the two capacitor voltages:

$$M_{QBC1} = \frac{V_{OUT}}{V_{IN}} = \frac{1}{(1-D)^2} \tag{24}$$

From which it is possible to obtain the input to output current gain:

$$\frac{I_{OUT}}{I_{IN}} = {M_{QBC1}}^{-1} \tag{25}$$

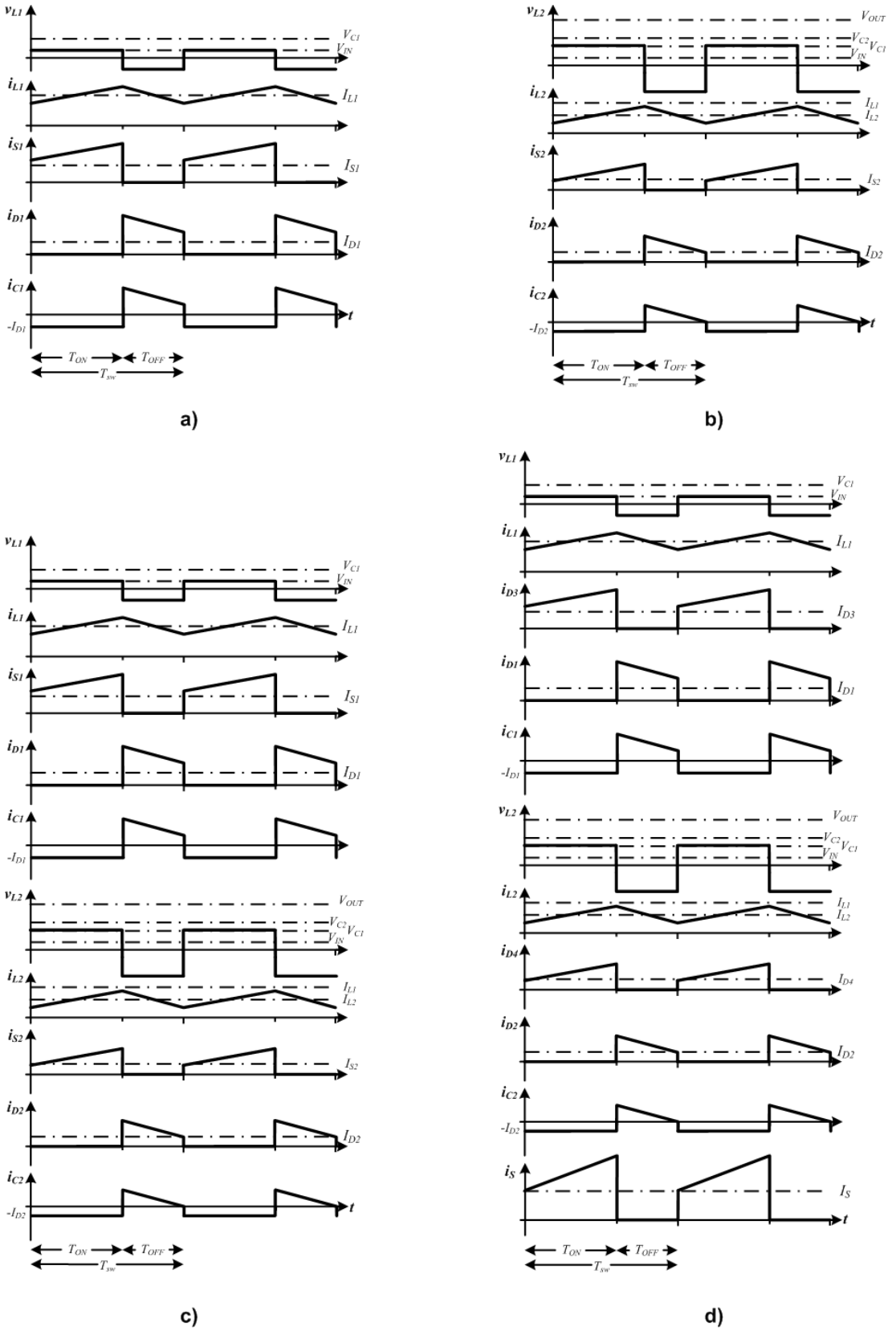

Figure 24 Time domain waveform of the *QBC1* step by step in CCM: a) first stage of the *QBC1*; b) second stage of the *QBC1*; c) double-switch *QBC1*; d) single-switch *QBC1*.

From eq. (25) it is possible evaluate the input current as function of the input voltage supply and the duty-cycle as following:

$$I_{IN} = I_{L1} = \frac{V_{IN}}{R(1-D)^4} \tag{26}$$

By imposing the power balance in the first stage of the *QBC1* it is possible obtain the current average value of the second inductor:

$$I_{L2} = \frac{V_{IN}}{V_{C1}} I_{L1} = (1-D) I_{L1} \tag{27}$$

The diodes and switch current can be obtained from the knowledge of the inductor currents:

$$i_{D1} = \begin{cases} 0 & \text{during } T_{ON} \\ i_{L1} & \text{during } T_{OFF} \end{cases} \tag{28}$$

$$i_{D2} = \begin{cases} 0 & \text{during } T_{ON} \\ i_{L2} & \text{during } T_{OFF} \end{cases} \tag{29}$$

$$i_{D3} = i_{S1} = \begin{cases} i_{L1} & \text{during } T_{ON} \\ 0 & \text{during } T_{OFF} \end{cases} \tag{30}$$

$$i_{D4} = i_{S2} = \begin{cases} i_{L2} & \text{during } T_{ON} \\ 0 & \text{during } T_{OFF} \end{cases} \tag{31}$$

$$i_S = i_{D3} + i_{D4} = \begin{cases} i_{L1} + i_{L2} & \text{during } T_{ON} \\ 0 & \text{during } T_{OFF} \end{cases} \tag{32}$$

Assuming that the capacitive impedances are much lower than the loads one, all the ripple current of the diodes D_1 and D_2 flows respectively through the capacitors C_1 and C_2 meanwhile the average value through the respective loads (the output current of the first stage of the *QBC1* is I_{L2} whereas the output current of the second stage is I_{OUT}). In conclusion, the output current of the first stage of the *QBC1* is equal to the average value of the diode current D_1; the output current of the second one is equal to the average value of the diode current D_2; the capacitor currents have the same waveform of the diode currents with a null average value. By the knowledge of the capacitor current, integrating, it is possible obtain the trend of the output voltage as sum of the capacitor voltages.

The output voltage ripple can be calculated by the charge variation on the two capacitors:

$$\Delta V_{OUT} = \Delta V_{C1} + \Delta V_{C2} \tag{33}$$

with:

$$\Delta V_{C1} = \frac{\Delta Q_{C1}}{C_1} = \frac{I_{L2} T_{ON}}{C_1} = \frac{V_{OUT}}{R(1-D)} \frac{D}{C_1 f_{sw}} \tag{34}$$

$$\Delta V_{C2} = \frac{\Delta Q_{C2}}{C_2} = \frac{I_{OUT} T_{ON}}{C_2} = \frac{V_{OUT}}{R} \frac{D}{C_2 f_{sw}} \tag{35}$$

In general, the output voltage ripple depends on the load value, the capacitor tank and the switching frequency. In equation (33), the contribution of the capacitor C_2 is linear with the duty-cycle, whereas for C_1 depends on the known non-linear function $D/(1-D)$ (it is the gain of the Buck/Boost converter).

The peak to peak inductor currents can be evaluated by integrating the inductor equation during T_{ON}:

$$\Delta i_{L1} = \frac{V_{IN}}{L_1} T_{ON} = \frac{V_{IN}}{L_1} \frac{D}{f_{sw}} \tag{36}$$

$$\Delta i_{L2} = \frac{V_{C1}}{L_2} T_{ON} = \frac{V_{IN}}{(1-D) L_2} \frac{D}{f_{sw}} \tag{37}$$

It should be noted that the current ripples depend by the inductor tank and the switching frequency. Moreover $\Delta i_{L1}$is linear with the duty-cycle, Δi_{L2} is instead non-linear versus the duty-cycle.

As for all the DC/DC switching converters, the entity of the current ripple defines the operating mode of the converter: CCM, BCM and DCM.

The mathematical inequality, that ensures at least a BCM, is given by:

$$I_{Li,min} \geq \frac{\Delta i_{Li}}{2} \qquad \text{with } i=1,2 \tag{38}$$

From which:

$$L_1 \geq \frac{1}{2} \frac{V_{IN}}{I_{L1,min}} \frac{D}{f_{sw}} \tag{39}$$

$$L_2 \geq \frac{1}{2} \frac{V_{IN}}{I_{L2,min}} \frac{D}{(1-D) f_{sw}} \tag{40}$$

Where $I_{Li,min}$ represents the minimum average value of the inductor currents of the converter. Its values depend on the load, R. Using equations (26) and (27), the inductor inequalities are given by:

$$\mathrm{L}_1 \geq \frac{1}{2}\frac{R}{f_{sw}}\mathrm{D}(1-D)^4 \tag{41}$$

$$\mathrm{L}_2 \geq \frac{1}{2}\frac{R}{f_{sw}}\mathrm{D}(1-D)^2 \tag{42}$$

Defining the design constant K_i equal to $\frac{2L_i}{RT_{sw}}$, with *i*=1,2; it is possible rewrite the equations (41) and (42) as follow:

$$\mathrm{K}_1 \geq \mathrm{D}(1-D)^4 = k_1(D) \tag{43}$$

$$\mathrm{K}_2 \geq \mathrm{D}(1-D)^2 = k_2(D) \tag{44}$$

The analysis of the function $k_1(D)$ and $k_2(D)$ is useful to design the two power inductors because, on the bases of the the maximum points of the functions, the inductors that ensure the CCM in all the range of duty-cycle can be chosen. The design of the second inductor it is the same of the Boost converter inductor, eq.(13); furthermore, the maximum point of the function $k_2(D)$ is equal to *4/27* for duty-cycle equal to *1/3*. For the primary inductor, the function $k_1(D)$ has a maximum point equal to $2^8/5^5$ for a duty-cycle value equal to *1/5*.

2.3. QBC2

The electric scheme of the ideal Quadratic Boost Converter *QBC2* is shown in Figure 25. It exhibits the presence of two inductors, two capacitors and three diodes; furthermore, like in the traditional Boost converter, only a power switch is required.

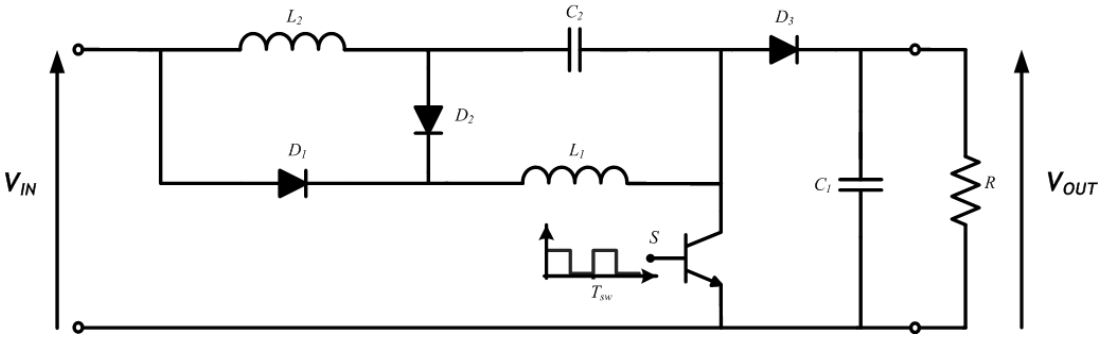

Figure 25 Ideal electric scheme of the quadratic boost converter *QBC2*.

The following analysis has been made under the assumptions that converter works in CCM. In this case, the *QBC2* presents two modes within a switching

period: *mode on* and *mode off*. The converter works in *mode on* when the switching device *S* is turned on, otherwise it works in *mode off*, if *S* is turned off.

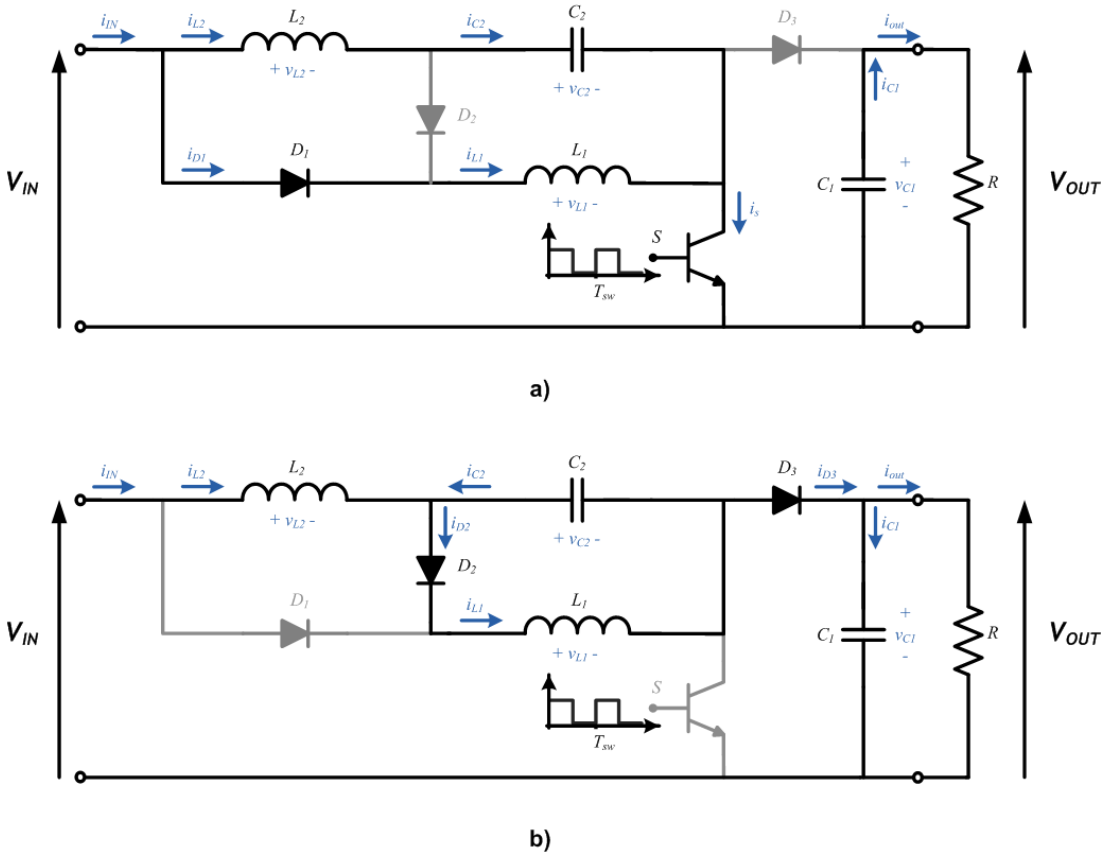

Figure 26 Continuous conduction mode configuration of the *QBC2*: a) *mode on*, b) *mode off*.

During the *mode on*, see Figure 26 a), the diode D_1 is turned on and the diodes D_2 and D_3 are turned off. In this phase the input voltage source is directly connected to the inductors L_1 and L_2. It results in accumulating energy in L_1 and L_2. Moreover, since the capacitor C_2 is connected in series with L_2, C_2 stores energy as well. In this stage the capacitor C_1 supply energy to the output load, under a progressive discharge.

In *mode off*, see Figure 26 b), the diode D_1 is turned off and instead the diodes D_2 and D_3 are turned on. In this configuration of the converter the inductors L_1 and L_2 and the capacitor C_2 release the energy previously stored in the *mode on*; on the contrary, the capacitor C_1 stores energy.

Under the assumption of continuous conduction operation, Figure 27 shows the qualitative trend of the inductor voltages and all the currents of the *QBC2*. Looking

at these waveforms, it can be easily noted that several differences related to other QBCs single switch occur. For example as far as the input current is concerned, it can be observed that even the theoretical waveform presents a well-defined discontinuity, differently from the *QBC1*, where it is smoother. Moreover, Table 1 summarizes the main signals of the *QBC2*.

Table 1 Outline of the main signals of the *QBC2* in CCM.

	Symbol	Mode ON	Mode OFF	Average Value
(45)	i_{L1}	$i_{IN} - i_{C2}$	$i_{IN} - i_{C2}$	I_{IN}
(46)	i_{L2}	$i_{IN} - i_{L1}$	i_{IN}	$I_{IN}(1\text{-}D)$
(47)	v_{L1}	V_{IN}	V_{C2}	0
(48)	v_{L2}	$V_{IN} - V_{C2}$	$V_{IN} - (V_{C2} + V_{OUT})$	0
(49)	i_{IN}	$i_{L1} + i_{L2}$	i_{L2}	I_{IN}
(50)	i_{D1}	i_{L1}	0	$I_{IN}D$
(51)	i_{D2}	0	i_{L1}	$I_{IN}(1\text{-}D)$
(52)	i_{D3}	0	i_{L2}	$I_{IN}(1\text{-}D)^2$
(53)	i_{C1}	$- I_{OUT}$	$i_{L2} - I_{OUT}$	0
(54)	i_{C2}	i_{L2}	$i_{L1} - i_{L2}$	0
(55)	i_S	$i_{L1} + i_{L2}$	0	$I_{IN}(2\text{-}D)D$

During the *mode on*, the i_{L1} and i_{L2} currents increases with a slope equals respectively to V_{IN}/L_1 and $(V_{IN} - V_{C2})/L_2$ while in the *mode off* decreases with V_{C2}/L_1 and $(V_{IN} - V_{C2} - V_{OUT})/L_2$. Imposing that at steady-state the voltage average values of the inductors are equal to zero, the average voltage value of the capacitor C_2 can be obtained, as well as the ideal conversion ratio M of the converter, as follows:

$$V_{L1} = \frac{1}{T_{sw}} \int_0^{T_{sw}} v_{L1} dt = V_{IN} D + V_{C2}(1 - D) = 0 \quad \Rightarrow$$

$$V_{C2} = -V_{IN} \frac{D}{(1 - D)} \tag{56}$$

$$V_{L2} = \frac{1}{T_{sw}} \int_0^{T_{sw}} v_{L2} dt = (V_{IN} - V_{C2}) - V_{OUT}(1 - D) = 0 \quad \Rightarrow$$

$$M_{QBC2} = \frac{V_{OUT}}{V_{IN}} = \frac{1}{(1 - D)^2} \tag{57}$$

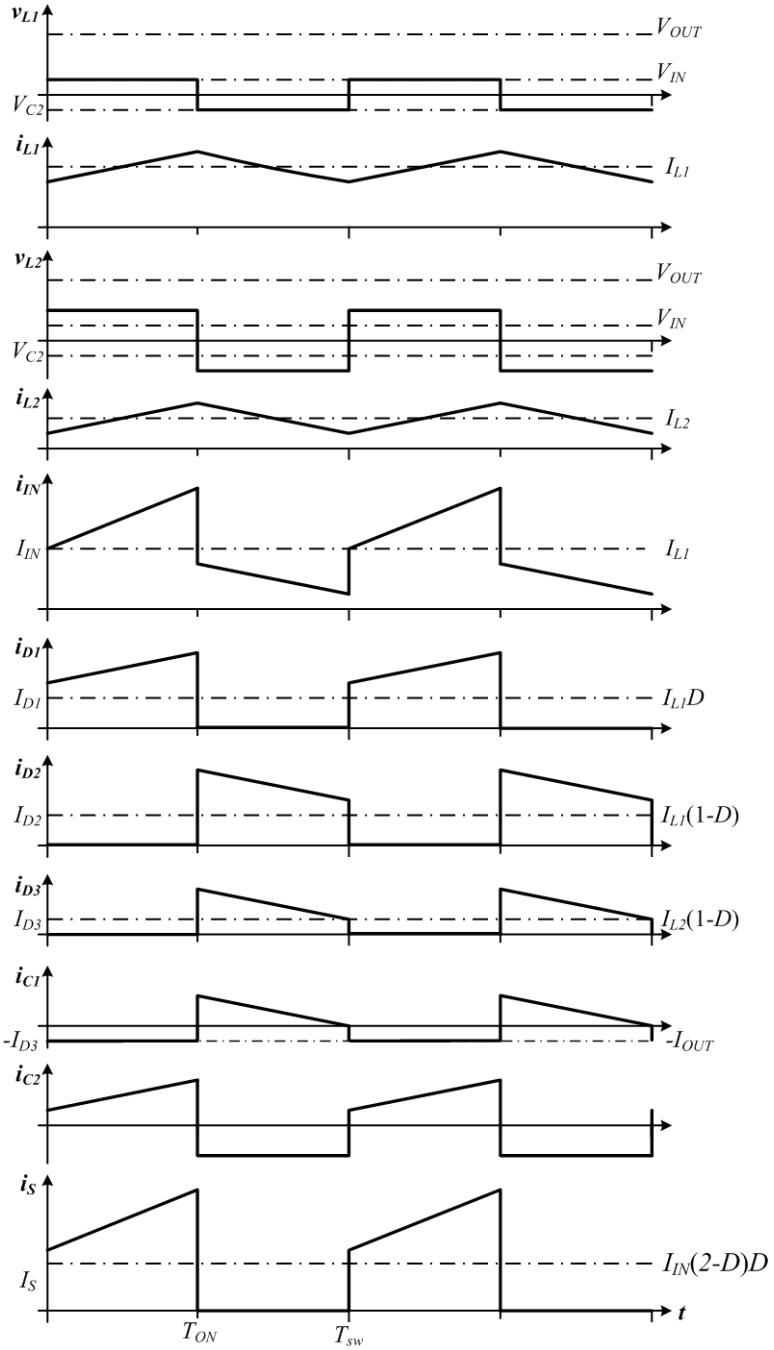

Figure 27 Continuous conduction mode time domain waveforms of the QBC2.

Under the assumption that the converter is ideal, the input power is equal to the output power; the average value of the input current is therefore equal to:

$$I_{L1} = \frac{I_{OUT}}{(1-D)^2} = \frac{V_{IN}}{R(1-D)^4} \tag{58}$$

If eq. (45) of Table 1 is exploited, considering also that the average value of the current of a capacitor is null at steady-state, it is possible obtain that:

$$I_{L1} = I_{IN} \tag{59}$$

Given eq. (59), exploiting also eq. (46) of Table 1, it is possible to obtain the average value of the inductor L_2:

$$I_{L2} = I_{IN} - I_{L1}D = I_{L1}(1\text{-}D) \tag{60}$$

Assuming that the capacitive impedance is much lower than the load one, all the ripple current of the diodes D_3 flows through the capacitor C_1 meanwhile the average value through the load. In conclusion, the output current of the *QBC2* is equal to the average value of the diode current D_3; the capacitor current have the same waveform of the diode current with a null average value. By the knowledge of the capacitor current, integrating, it is possible obtain the trend of the output voltage.

The output voltage ripple can be calculated by the charge variation on the capacitor:

$$\Delta V_{OUT} = \frac{\Delta Q_{C1}}{C_1} = \frac{I_{OUT} T_{ON}}{C_1} = \frac{V_{OUT}}{R} \frac{D}{C_1 f_{sw}} \tag{61}$$

Furthermore, the design condition for the output capacitor is given by:

$$C_1 \geq \frac{V_{OUT}}{R \Delta V^*_{OUT}} \frac{D}{C_1 f_{sw}} \tag{62}$$

where V^*_{OUT} represents the desired value of the output ripple. The output voltage ripple depends on the load value, the capacitor tank, the switching frequency and linearly by the duty-cycle.

The specification of the middle capacitor C_2 is only in terms of efficiency because it plays no role about the input-output voltage ripple requirements. In general, if the capacitor value increases the Equivalent Series Resistance (ESR) increases as well. Therefore it is important to improve the efficiency of the converter to select the minimum tank of energy. Known that, during the *mode on*, the current of the capacitor C_2 is equal to the current of L_2 it is possible write the following energy balance:

$$\frac{1}{2} L_2 (I_{L2} D)^2 \leq \frac{1}{2} C_2 (V_{L2})^2 \tag{63}$$

Using the previous equation, the design relation of the middle capacitor is the following:

$$C_2 \geq L_2 \left(\frac{I_{L2}}{V_{IN}}\right)^2 \geq L_2 \left(\frac{I_{L2}}{V_{IN}}\right)^2 (1 - D)^2 \tag{64}$$

The peak to peak inductor currents can be evaluated by integrating the inductor equation during T_{ON}:

$$\Delta i_{L1} = \frac{V_{IN}}{L_1}\, T_{ON} = \frac{V_{IN}}{L_1}\frac{D}{f_{sw}} \tag{65}$$

$$\Delta i_{L2} = \frac{V_{IN} - V_{C2}}{L_2}\, T_{ON} = \frac{V_{IN}}{(1-D)L_2}\frac{D}{f_{sw}} \tag{66}$$

It should be noted that the current ripples depend by the inductor tank and the switching frequency. Moreover $\Delta i_{L1}$is linear with the duty-cycle, Δi_{L2} is instead non-linear versus the duty-cycle (Buck-Boost gain).

As for all the DC/DC switching converter, the entity of the current ripple defines the operating mode of the converter: CCM, BCM and DCM. The mathematical inequality, that ensures at least a BCM, is given by:

$$I_{Li,min} \geq \frac{\Delta i_{Li}}{2} \qquad \text{with } i\text{=1,2} \tag{67}$$

From which:

$$\mathrm{L}_1 \geq \frac{1}{2}\frac{V_{IN}}{I_{L1,min}}\frac{D}{f_{sw}} \tag{68}$$

$$\mathrm{L}_2 \geq \frac{1}{2}\frac{V_{IN}}{I_{L2,min}}\frac{D}{(1-D)f_{sw}} \tag{69}$$

Where $I_{Li,min}$ represents the minimum average value of the inductor currents of the converter. Its value depends on the load, *R*. Furthermore, the design inductor inequalities are given by:

$$\mathrm{L}_1 \geq \frac{1}{2}\frac{R}{f_{sw}}\mathrm{D}(1-D)^4 \tag{70}$$

$$\mathrm{L}_2 \geq \frac{1}{2}\frac{R}{f_{sw}}\mathrm{D}(1-D)^2 \tag{71}$$

Defining the design constant K_i equal to $\frac{2L_i}{RT_{sw}}$, with *i*=1,2; it is possible rewrite the equations as follow:

$$\mathrm{K}_i \geq k_i(D) = \begin{cases} \mathrm{D}(1-D)^4 & \text{IF} \quad \mathrm{i} = 1 \\ \mathrm{D}(1-D)^2 & \text{IF} \quad \mathrm{i} = 2 \end{cases} \tag{72}$$

The trends of the function $k_i(D)$ are shown in Figure 28 and are the same non-linear design function of the *QBC1*.

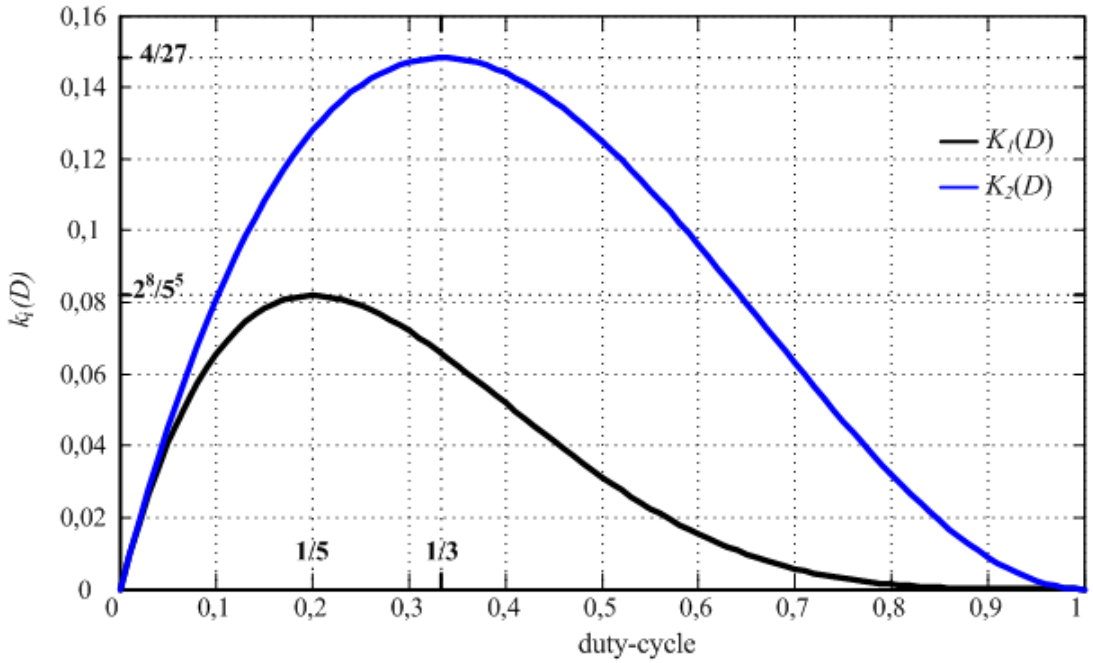

Figure 28 Inductor design function of the QBC1 and *QBC2*.

2.4. Conclusion

In the step-up static conversion, the non-isolated single-switch topologies are very interesting solutions since the transformer increases cost, volume and losses. Moreover, the single-switch makes the driver a simple circuit and reduces the power losses. In this chapter two novel transformer-less and single-switch topologies of Quadratic Boost converters are been treated: *QBC1* and *QBC2*. For these two converters, the operating principle, the ideal time domain waveforms and the design equations of the power stage have been presented.

The *QBC1* presents a lower ripple of the input current than the *QBC2*. This feature is a benefit in the fuel cell generation because improve the reliability. On the other side, the *QBC1* presents one power diode more; therefore, it has less efficiency than the *QBC2*.

Chapter 3

Modeling of a DC/DC Switching Converter

3.1. Introduction

The scope of modeling is seeks to obtain, by a mathematical point of view, the dynamic behavior of a system. Thanks to the dynamical models, it is possible to simulate the system behavior and also to device various control laws. The steady-state model is a subset of the dynamic model because it is obtained by zeroing its time derivatives.

The DC/DC switching converters are non-linear systems. This non-linear behavior is due to the fact that, even if the passive elements are linear and invariant, and the power devices are ideals[3], the latter are non-linears. For this last reason, it is necessary apply non-linear model techniques.

Generally speaking, there are two main modeling approaches: one that uses the known information of the system and the physical laws; the latter uses a black-box model based on the response of the system to some known input signals. A mixing between these two approaches leads to the so called gray-box models. This chapter deals with the main modeling techniques of DC/DC switching converters. An overview of the different modeling approaches is provided and then applied to the two proposed QBCs.

3.1. State Space Averaging

The State Space Averaging (SSA) modeling for the study of switching converters, in CCM, was introduced by (MIDDLEBROOK & ĆUK 1976). Any DC/DC switching converter, operating in continuous conduction mode, can be described by the state space representations for the two linear electric networks: *on mode* and *off mode*:

[3] The power devices are considered ideal if the switching time is infinitely short, the conduction resistance is null (during *on state*) and during the *off state* it has an infinity value. Moreover in the case of the power diodes the voltage forward drop is zero.

$$\begin{cases} \dot{\boldsymbol{x}} = \boldsymbol{A}_{on}\boldsymbol{x} + \boldsymbol{B}_{on}u \\ y = \boldsymbol{C}_{on}\boldsymbol{x} \end{cases} \quad \text{during } T_{ON} \tag{73}$$

$$\begin{cases} \dot{\boldsymbol{x}} = \boldsymbol{A}_{off}\boldsymbol{x} + \boldsymbol{B}_{off}u \\ y = \boldsymbol{C}_{off}x \end{cases} \quad \text{during } T_{OFF} \tag{74}$$

Where the state vector $\boldsymbol{x}$ belonging to $\Re^n$, the scalar input u is equal to the input power supply and finally the scalar y is the output voltage. The dimension of the state space depends on the number of elements able to store energy (inductors and capacitors). It should be noted that the two state space representations have the state vector, the input and the output in common. The matrices $\boldsymbol{A}_{mode(n\times n)}$, $\boldsymbol{B}_{mode(n\times 1)}$ and $\boldsymbol{C}_{mode(1\times n)}$, with *mode=on,off*, are obtained for visual inspection using the electric physical laws.

The SSA model is obtained by averaging, in the switching period, the two linear models:

$$\begin{cases} \dot{\boldsymbol{x}} = \big(\boldsymbol{A}_{on}D + \boldsymbol{A}_{off}(1-D)\big)\boldsymbol{x} + \big(\boldsymbol{B}_{on}D + \boldsymbol{B}_{off}(1-D)\big)u \\ y = \big(\boldsymbol{C}_{on}D + \boldsymbol{C}_{off}(1-D)\big)\boldsymbol{x} \end{cases} \tag{75}$$

The SSA model is non-linear and describes the mean behavior of the converter in a switching period; furthermore it is not able to describe the typical switching behavior.

The SSA model can be linearized around an operating point. More exactly, by introducing a small perturbation as following: $\psi = \Psi + \tilde{\psi}$ where $\Psi \gg \tilde{\psi}$ with $\Psi = Y, D, X, U$ and $\tilde{\psi} = \tilde{y}, \tilde{d}, \tilde{x}, \tilde{u}$. If there are not variations of the input voltage ($\tilde{u} = 0$) and we neglect the 2nd order small signal terms, the SSA model can be rewrite as:

$$\begin{cases} \dot{\tilde{\boldsymbol{x}}} = \boldsymbol{A}\boldsymbol{X} + \boldsymbol{B}U + \boldsymbol{A}\tilde{\boldsymbol{x}} + \boldsymbol{B}_d\tilde{d} \\ Y + \tilde{y} = \boldsymbol{C}\boldsymbol{X} + \boldsymbol{C}\tilde{\boldsymbol{x}} + \boldsymbol{E}_{\boldsymbol{d}}\tilde{d} \end{cases} \tag{76}$$

with:

$$\boldsymbol{B}_d = \big[\big(\boldsymbol{A}_{on} - \boldsymbol{A}_{off}\big) + \big(\boldsymbol{B}_{on} - \boldsymbol{B}_{off}\big)\big]\boldsymbol{X}$$

$$\boldsymbol{E}_d = \big(\boldsymbol{C}_{on} - \boldsymbol{C}_{off}\big)\boldsymbol{X}$$

The linear model in the equation (76) is composed by the steady-state model and the small signal model. The dc component is useful to obtain the steady-state values of the state vector, the output voltage and the input to output conversion ratio:

$$\begin{cases} \boldsymbol{X} = -\boldsymbol{A}^{-1}\boldsymbol{B}U \\ Y = -\boldsymbol{C}\boldsymbol{A}^{-1}\boldsymbol{B}U \end{cases} \tag{77}$$

$$M = \frac{Y}{U} = -\boldsymbol{C}\boldsymbol{A}^{-1}\boldsymbol{B} \tag{78}$$

The ac component of (76) can be transformed into Laplace domain as following:

$$\begin{cases} s\tilde{\boldsymbol{X}}(s) = \boldsymbol{A}\tilde{\boldsymbol{X}}(s) + \boldsymbol{B}_d\tilde{D}(s) \\ \tilde{Y}(s) = \boldsymbol{C}\tilde{\boldsymbol{X}}(s) + \boldsymbol{E}_{\boldsymbol{d}}\tilde{D}(s) \end{cases} \tag{79}$$

where:

$$\tilde{\boldsymbol{X}}(s) = \mathcal{L}[\tilde{\boldsymbol{x}}]$$

$$\tilde{\boldsymbol{Y}}(s) = \mathcal{L}[\tilde{\boldsymbol{y}}]$$

$$\tilde{\boldsymbol{D}}(s) = \mathcal{L}[\tilde{\boldsymbol{d}}]$$

By solving equation (79) it is possible obtain the transfer function of the power stage which is useful for the tuning of a voltage controller:

$$G_{\tilde{y},\tilde{d}} = \boldsymbol{C}(s\boldsymbol{I}_{\boldsymbol{n}} - \boldsymbol{A})^{-1}\boldsymbol{B}_d + \boldsymbol{E}_{\boldsymbol{d}} \tag{80}$$

3.1.1. SSA modeling of the QBC1

The SSA model of the *QBC1* has been derived under the assumption that all the power devices are ideals and obviously the converter working in CCM. Under these hypotheses, the electric scheme of the *QBC1* presents four Equivalent Series Resistances (ESRs): r_{L1}, r_{L2}, r_{C1} and r_{C2} (see Figure 29).

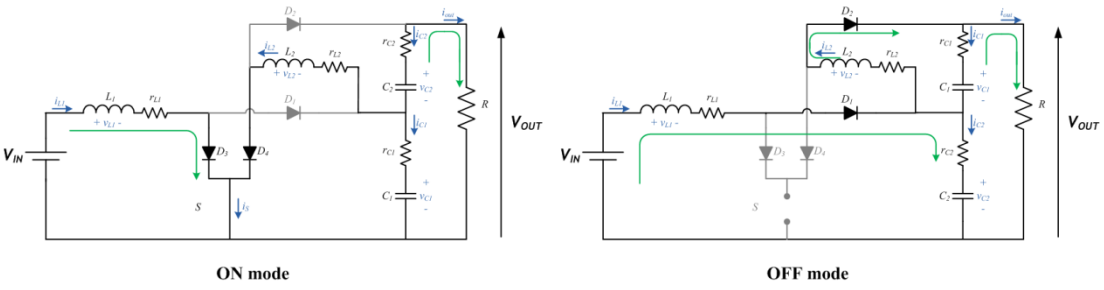

Figure 29 Electric scheme of the *QBC1* with ESRs in the two operating modes.

By writing the Kirchhoff equations for the two circuits sketched in Figure 29, it is possible obtain the state space models of the *QBC1*:

$$\begin{cases} \underbrace{\begin{bmatrix} \dot{i}_{L1} \\ \dot{i}_{L2} \\ \dot{v}_{C1} \\ \dot{v}_{C2} \end{bmatrix}}_{\dot{x}} = \underbrace{\begin{bmatrix} -\frac{r_{L1}}{L_1} & 0 & 0 & 0 \\ 0 & -\frac{r_{L2}\delta + r_{C2}\delta_1}{L_2\delta} & -\frac{r_{C2}}{L_2\delta} & \frac{\delta_1}{L_2\delta} \\ 0 & \frac{r_{C2}}{C_1\delta} & -\frac{1}{C_1\delta} & -\frac{1}{C_1\delta} \\ 0 & -\frac{\delta_1}{C_2\delta} & -\frac{1}{C_2\delta} & -\frac{1}{C_2\delta} \end{bmatrix}}_{\boldsymbol{A_{on}}} \underbrace{\begin{bmatrix} i_{L1} \\ i_{L2} \\ v_{C1} \\ v_{C2} \end{bmatrix}}_{x} + \underbrace{\begin{bmatrix} \frac{1}{L_1} \\ 0 \\ 0 \\ 0 \end{bmatrix}}_{\boldsymbol{B_{on}}} \underbrace{V_{IN}}_{u} \\ \underbrace{V_{OUT}}_{y} = \underbrace{\begin{bmatrix} 0 & \frac{Rr_{C2}}{\delta} & \frac{R}{\delta} & \frac{R}{\delta} \end{bmatrix}}_{\boldsymbol{C_{on}}} \underbrace{\begin{bmatrix} i_{L1} \\ i_{L2} \\ v_{C1} \\ v_{C2} \end{bmatrix}}_{\boldsymbol{x}} \end{cases} \tag{81}$$

$$\begin{cases} \underbrace{\begin{bmatrix} \dot{i}_{L1} \\ \dot{i}_{L2} \\ \dot{v}_{C1} \\ \dot{v}_{C2} \end{bmatrix}}_{\dot{x}} = \underbrace{\begin{bmatrix} -\frac{r_{L1}\delta + r_{C2}\delta_1}{L_1\delta} & \frac{r_{C1}r_{C2}}{L_1\delta} & \frac{r_{C2}}{L_1\delta} & -\frac{\delta_1}{L_1\delta} \\ \frac{r_{C1}r_{C2}}{L_2\delta} & -\frac{r_{L2}\delta + r_{C1}\delta_2}{L_2\delta} & -\frac{\delta_2}{L_2\delta} & \frac{r_{C1}}{L_2\delta} \\ -\frac{r_{C2}}{C_1\delta} & \frac{\delta_2}{C_1\delta} & -\frac{1}{C_1\delta} & -\frac{1}{C_1\delta} \\ \frac{\delta_1}{C_2\delta} & -\frac{r_{C1}}{C_2\delta} & -\frac{1}{C_2\delta} & -\frac{1}{C_2\delta} \end{bmatrix}}_{\boldsymbol{A_{off}}} \underbrace{\begin{bmatrix} i_{L1} \\ i_{L2} \\ v_{C1} \\ v_{C2} \end{bmatrix}}_{x} + \underbrace{\begin{bmatrix} \frac{1}{L_1} \\ 0 \\ 0 \\ 0 \end{bmatrix}}_{\boldsymbol{B_{off}}} \underbrace{V_{IN}}_{u} \\ \underbrace{V_{OUT}}_{y} = \underbrace{\begin{bmatrix} \frac{Rr_{C2}}{\delta} & \frac{Rr_{C1}}{\delta} & \frac{R}{\delta} & \frac{R}{\delta} \end{bmatrix}}_{\boldsymbol{C_{off}}} \underbrace{\begin{bmatrix} i_{L1} \\ i_{L2} \\ v_{C1} \\ v_{C2} \end{bmatrix}}_{\boldsymbol{x}} \end{cases} \tag{82}$$

where $\delta = R + r_{C1} + r_{C2}$, $\delta_1 = R + r_{C1}$, and $\delta_2 = R + r_{C2}$. It should be noted that the two models are the fourth order because there are two inductors and two capacitors. The state vector belonging to the to the 4th dimensional Euclidean space and it is equal to $[x_1, x_2, x_3, x_4]^T = [i_{L1}, i_{L2}, v_{C1}, v_{C2}]^T$.

Using the equations (75),(81) and (82) it is possible to obtain the non-linear SSA model which describes the average behavior of the converter:

$$\begin{cases} \dot{\boldsymbol{x}} = \underbrace{\begin{bmatrix} -\frac{r_{L1}\delta + r_{C2}\delta_1(1-D)}{L_1\delta} & \frac{r_{C1}r_{C2}(1-D)}{L_1\delta} & \frac{r_{C2}(1-D)}{L_1\delta} & -\frac{\delta_1(1-D)}{L_1\delta} \\ \frac{r_{C1}r_{C2}(1-D)}{L_2\delta} & -\frac{\delta_D}{L_2\delta} & -\frac{r_{C2}+R(1-D)}{L_2\delta} & \frac{r_{C1}+RD}{L_2\delta} \\ -\frac{r_{C2}(1-D)}{C_1\delta} & \frac{R(1-D)+r_{C2}}{C_1\delta} & -\frac{1}{C_1\delta} & -\frac{1}{C_1\delta} \\ \frac{\delta_1(1-D)}{C_2\delta} & -\frac{RD+r_{C1}}{C_2\delta} & -\frac{1}{C_2\delta} & -\frac{1}{C_2\delta} \end{bmatrix}}_{\boldsymbol{A}} \boldsymbol{x} + \underbrace{\begin{bmatrix} \frac{1}{L_1} \\ 0 \\ 0 \\ 0 \end{bmatrix}}_{\boldsymbol{B}} u \\ y = \underbrace{\begin{bmatrix} \frac{Rr_{C2}}{\delta} & \frac{Rr_{C1}}{\delta} & \frac{R}{\delta} & \frac{R}{\delta} \end{bmatrix}}_{\boldsymbol{C}} \boldsymbol{x} \end{cases} \tag{83}$$

with $\delta_D = r_{L2}\delta + r_{C1}\delta_2 + R(r_{C2} - r_{C1})D$.

Thanks to knowledge of the matrices of the SSA model of the QBC1 and the steady-state space vector it is possible evaluate the input to output conversion ratio including the parasitic elements:

$$M = \frac{(1+2r_C/R)}{(1-D)^2+\frac{r_{L1}+r_{L2}(1-D)^2+[(2r_C r_{L2}/R)(1-D)^2+2r_C(1-D)^2+2r_C r_{L1}/R+r_C D(1-D)(r_C/R-1)]}{R(1-D)^2}} \quad (84)$$

The last equation has been evaluated in the assumption that the two capacitors are the same ($C_1 = C_2$ and $r_C = r_{C1} = r_{C2}$). It should be noted that if all the parasitic resistances are nulls, the real static gain become the ideal one.

By considering nulls the ESRs of the two capacitors, the small signal transfer function using equation (80) is given by:

$$G_{\widetilde{v_o},\tilde{d}} = RV_{IN}\frac{a_3 s^3+a_2 s^2+a_1 s+a_0}{b_4 s^4+b_3 s^3+b_2 s^2+b_1 s+b_0} \quad (85)$$

with:

$$a_3 = CL_1L_2(2D-3)$$

$$a_2 = C[L_2 r_{L2}(1-D)^2 + L_1 R(5D^2 - 2D^3 - 4D + 1) + L_2 R(1-D)^4 + \\ + L_1 r_{L2}(2D-3) + L_2 r_{L1}(2D-3)$$

$$a_1 = -2L_1(1-D) - L_2(1-D)^3 + Cr_{L2}^2(1-D)^2 + CRr_{L1}(-2D^3 + 5D^2 + \\ -4D + 1) + CRr_{L2}(1-D)^4 + Cr_{L1}r_{L2}(2D-3)$$

$$a_0 = 2R(1-D)^5 + 2r_{L1}(1-D)$$

$$b_4 = C^2 L_1 L_2 R[R(1-D)^4 + r_{L1} + r_{L2}(1-D)^2]$$

$$b_3 = [2CL_1L_2 + C^2 L_1 R r_{L2} + C^2 L_2 R r_{L1}][R(1-D)^4 + r_{L1} + r_{L2}(1-D)^2]$$

$$b_2 = [CL_1R(1+2D^2-2D) + CL_2R(1-D)^2 + 2C(L_1 r_{L2} + L_2 r_{L1}) + C^2 R \cdot \\ \cdot r_{L1}r_{L2}]\,[R(1-D)^4 + r_{L1} + r_{L2}(1-D)^2]$$

$$b_1 = [R(1-D)^4 + r_{L1} + r_{L2}(1-D)^2][L_1 + L_2(1-D)^2 + 2Cr_{L1}r_{L2} + CR \cdot \\ \cdot r_{L1}(1+2D^2-2D) + CRr_{L2}(1-D)^2]$$

$$b_0 = [R(1-D)^4 + r_{L1} + r_{L2}(1-D)^2]^2$$

The transfer function (85) is used to design a linear voltage mode controller (direct output control). In order to improve the closed loop performance, it is possible adopt

linear current mode controllers in which there are two control loops (indirect output control). The design of the inner loop, current loop, needs the knowledge of a current versus duty-cycle variations, i.e. inductor current versus duty-cycle. The small-signal transfer function of the inductor current versus the duty-cycle can be obtained using the models (81), (82) and (83) with the matrix $\boldsymbol{C} = \boldsymbol{C}_{on} = \boldsymbol{C}_{off} = [1 \quad 0 \quad 0 \quad 0]$ and, the equation (80):

$$G_{\widetilde{i_{L1}},\tilde{d}} = V_{IN}(1-D)\frac{a_3 s^3 + a_2 s^2 + a_1 s + a_0}{b_4 s^4 + b_3 s^3 + b_2 s^2 + b_1 s + b_0} \tag{86}$$

with:

$$a_3 = L_2 C^2 R^2 (1-D)^2 + L_2 C^2 R^2 r_{L2}$$

$$a_2 = C^2 R^2 r_{L2}(1-D)^2 + L_2 CR(2D^2 - 5D + 4) + C^2 R r_{L2}^2 + 2L_2 C r_{L2}$$

$$a_1 = CR^2(2D^4 + 5D^3 + 5D^2 - 3D + 1) + CRr_{L2}(4D^2 - 7D + 5) + 2Cr_{L2}^2 + L_2$$

$$a_0 = 4R(1-D)^2 + 2r_{L2}$$

$$b_4 = C^2 L_1 L_2 R[R(1-D)^4 + r_{L1} + r_{L2}(1-D)^2]$$

$$b_3 = [2CL_1 L_2 + C^2 L_1 R r_{L2} + C^2 L_2 R r_{L1}][R(1-D)^4 + r_{L1} + r_{L2}(1-D)^2]$$

$$b_2 = [CL_1 R(1 + 2D^2 - 2D) + CL_2 R(1-D)^2 + 2C(L_1 r_{L2} + L_2 r_{L1}) + C^2 R \cdot$$
$$\cdot r_{L1} r_{L2}]\,[R(1-D)^4 + r_{L1} + r_{L2}(1-D)^2]$$

$$b_1 = [R(1-D)^4 + r_{L1} + r_{L2}(1-D)^2][L_1 + L_2(1-D)^2 + 2Cr_{L1} r_{L2} + CR \cdot$$
$$\cdot r_{L1}(1 + 2D^2 - 2D) + CRr_{L2}(1-D)^2]$$

$$b_0 = [R(1-D)^4 + r_{L1} + r_{L2}(1-D)^2]^2$$

From the analysis of the two small-signal models (85) and (86) it is possible observe that the b_i coeffients are equals, therefore the poles map is identical.

3.1.2. SSA modeling of the QBC2

The SSA model of the *QBC2* has been derived under the assumption that all the power devices are ideals and obviously the converter working in CCM. Similarly to the *QBC1*, even the *QBC2* presents four parasitic parameters.

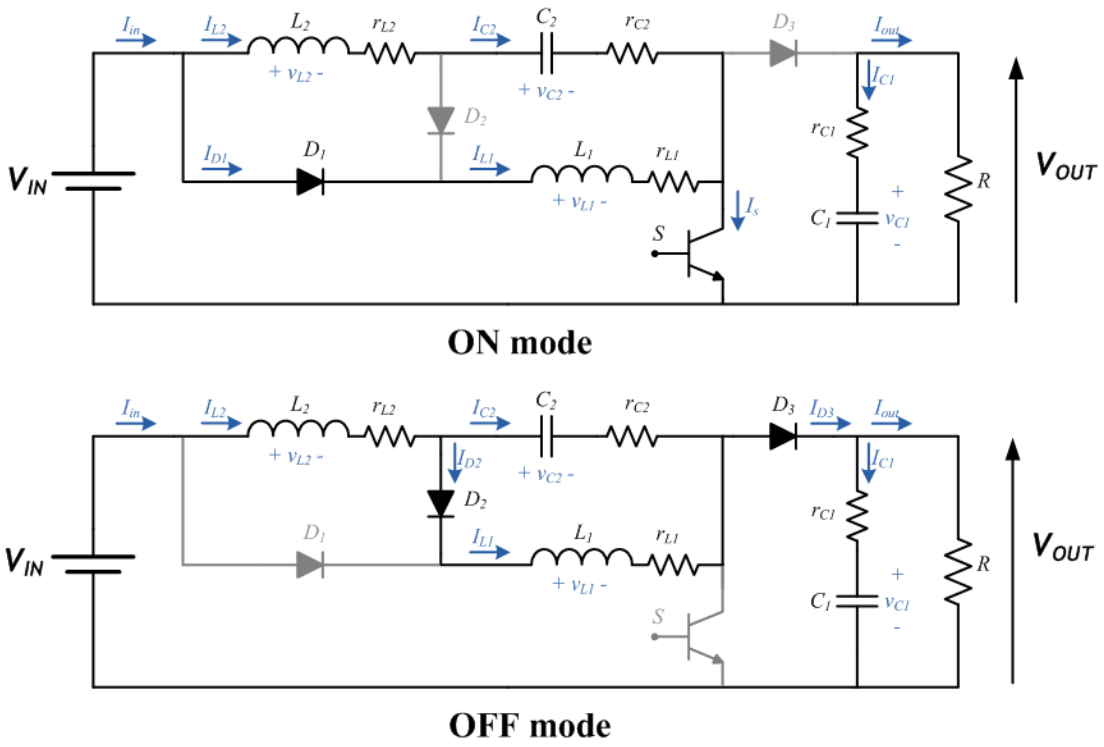

Figure 30 Electric scheme of the QBC2 with ESRs in the two operating modes.

By writing the Kirchhoff equations for the two circuits sketched in Figure 30, it is possible obtain the state space models of the *QBC2*:

$$\begin{cases} \underbrace{\begin{bmatrix} \dot{\imath}_{L1} \\ \dot{\imath}_{L2} \\ \dot{v}_{C1} \\ \dot{v}_{C2} \end{bmatrix}}_{\dot{x}} = \underbrace{\begin{bmatrix} -\frac{r_{L1}}{L_1} & 0 & 0 & 0 \\ 0 & -\frac{r_{L2}+r_{C2}}{L_2} & 0 & \frac{1}{L_2} \\ 0 & 0 & -\frac{1}{C_1\delta_1} & 0 \\ 0 & \frac{1}{C_2} & 0 & 0 \end{bmatrix}}_{\boldsymbol{A_{on}}} \underbrace{\begin{bmatrix} i_{L1} \\ i_{L2} \\ v_{C1} \\ v_{C2} \end{bmatrix}}_{x} + \underbrace{\begin{bmatrix} \frac{1}{L_1} \\ \frac{1}{L_2} \\ 0 \\ 0 \end{bmatrix}}_{\boldsymbol{B_{on}}} \underbrace{V_{IN}}_{u} \\ \underbrace{V_{OUT}}_{y} = \underbrace{\begin{bmatrix} 0 & 0 & \frac{R}{\delta_1} & 0 \end{bmatrix}}_{\boldsymbol{C_{on}}} \underbrace{\begin{bmatrix} i_{L1} \\ i_{L2} \\ v_{C1} \\ v_{C2} \end{bmatrix}}_{x} \end{cases} \tag{87}$$

$$\begin{cases} \underbrace{\begin{bmatrix} \dot{i}_{L1} \\ \dot{i}_{L2} \\ \dot{v}_{C1} \\ \dot{v}_{C2} \end{bmatrix}}_{\dot{\boldsymbol{x}}} = \underbrace{\begin{bmatrix} -\frac{r_{L1}+r_{C2}}{L_1} & \frac{r_{C2}}{L_1} & 0 & \frac{1}{L_1} \\ \frac{r_{C2}}{L_2} & -\frac{(r_{L2}+r_{C2})\delta_1+Rr_{C1}}{L_2\delta_1} & -\frac{R}{L_2\delta_1} & -\frac{1}{L_2} \\ 0 & \frac{R}{C_1\delta_1} & -\frac{1}{C_1\delta_1} & 0 \\ -\frac{1}{C_2} & \frac{1}{C_2} & 0 & 0 \end{bmatrix}}_{\boldsymbol{A_{off}}} \underbrace{\begin{bmatrix} i_{L1} \\ i_{L2} \\ v_{C1} \\ v_{C2} \end{bmatrix}}_{\boldsymbol{x}} + \underbrace{\begin{bmatrix} 0 \\ \frac{1}{L_2} \\ 0 \\ 0 \end{bmatrix}}_{\boldsymbol{B_{off}}} \underbrace{V_{IN}}_{u} \\ \underbrace{V_{OUT}}_{y} = \underbrace{\begin{bmatrix} 0 & \frac{Rr_{C1}}{\delta_1} & \frac{R}{\delta_1} & 0 \end{bmatrix}}_{\boldsymbol{C_{off}}} \underbrace{\begin{bmatrix} i_{L1} \\ i_{L2} \\ v_{C1} \\ v_{C2} \end{bmatrix}}_{\boldsymbol{x}} \end{cases} \tag{88}$$

where $\delta_1 = R + r_{C1}$. It should be noted that the two models are the fourth order because there are two inductors and two capacitors. The state vector belonging to the to the 4th dimensional Euclidean space and it is equal to $[x_1, x_2, x_3, x_4]^T = [i_{L1}, i_{L2}, v_{C1}, v_{C2}]^T$.

Using the equations (75), (87) and (88) it is possible to obtain the non-linear SSA model which describes the average behavior of the converter:

$$\begin{cases} \dot{\boldsymbol{x}} = \underbrace{\begin{bmatrix} -\frac{r_{L1}+r_{C2}(1-D)}{L_1} & \frac{r_{C2}(1-D)}{L_1} & 0 & \frac{(1-D)}{L_1} \\ \frac{r_{C2}(1-D)}{L_2} & -\frac{(r_{L2}+r_{C2})\delta_1+Rr_{C1}(1-D)}{L_2\delta_1} & -\frac{R(1-D)}{L_2\delta_1} & -\frac{1}{L_2} \\ 0 & \frac{R(1-D)}{C_1\delta_1} & -\frac{1}{C_1\delta_1} & 0 \\ -\frac{(1-D)}{C_2} & \frac{1}{C_2} & 0 & 0 \end{bmatrix}}_{\boldsymbol{A}} \boldsymbol{x} + \underbrace{\begin{bmatrix} \frac{D}{L_1} \\ \frac{1}{L_2} \\ 0 \\ 0 \end{bmatrix}}_{\boldsymbol{B}} u \\ y = \underbrace{\begin{bmatrix} 0 & \frac{Rr_{C1}(1-D)}{\delta_1} & \frac{R}{\delta_1} & 0 \end{bmatrix}}_{\boldsymbol{C}} \boldsymbol{x} \end{cases} \tag{89}$$

It should be noted that, different from the *QBC1*, the non-linearity of the model is present in the matrix $\boldsymbol{B}$ because $\boldsymbol{B}_{on} \neq \boldsymbol{B}_{off}$.

Thanks to knowledge of the matrices of the SSA model of the *QBC2* and the steady-state space vector it is possible evaluate the input to output conversion ratio including the parasitic elements:

$$M = \frac{(1+r_{C1}/R)}{(1-D)^2+\frac{r_{C1}}{R}(1-D)+\left(1+\frac{r_{C1}}{R}\right)\left(\frac{r_{L2}}{R}+\frac{r_{L1}}{R(1-D)^2}+\frac{r_{C2}D}{R(1-D)}\right)} \tag{90}$$

If in the last equation all the parasitic components are set equal to zero, it is possible to obtain the equation in the ideal case.

In the assumption that the equivalent series resistance of the capacitors are nulls, the transfer function of the power stage becomes:

$$G_{\widetilde{v_o},\tilde{d}} = V_{IN}\frac{n_4 s^4+n_3 s^3+n_2 s^2+n_1 s+n_0}{d_4 s^4+d_3 s^3+d_2 s^2+d_1 s+d_0} \quad (91)$$

with:

$n_4 = 0$

$n_3 = C_2L_1L_2R(1-D)$

$n_2 = C_2L_1R^2(1-D)^3-C_2R(L_1r_{L2}+ L_2r_{L1})(1-D)$

$n_1 = -R(1-D)(2L_1+C_2r_{L1}r_{L2}) + R[RC_2r_{L1}-L_2](1-D)^3$

$n_0 = -Rr_{L2}(1-D)^4+R^2(1-4D+5D^2-5D^4+4D^5-D^6)-Rr_{L1}(D^2-4D+3)$

$d_4 = C_1C_2L_1L_2R[r_{L1}+R(1-D)^4+ r_{L2}(1-D)^2]$

$d_3=C_2L_1L_2[R(1-D)^4+r_{L2}(1-D)^2+r_{L1}]+C_1C_2L_1Rr_{L2}^2(1-D)^2+C_1C_2L_1R^2r_{L2}(1-D)^4+$
$+C_1C_2L_2R^2r_{L1}(1-D)^4+ C_1C_2L_2Rr_{L1}r_{L2}(1-D)^2+ C_1C_2R[L_2r_{L1}^2+L_1r_{L1}r_{L2}]$

$d_2=[C_1L_1R^2+C_1L_2Rr_{L2}+2C_2L_1Rr_{L2}+C_2L_2Rr_{L1}+C_1C_2R^2r_{L1}r_{L2}](1D)^4+[C_1L_2R^2+C_2L_1\cdot$
$\cdot R^2](1-D)^6+[C_2L_1r_{L2}^2+C_1L_1Rr_{L2}++C_1L_2Rr_{L1}+C_2L_1Rr_{L1}+C_2L_2r_{L1}r_{L2}+C_1C_2Rr_{L1}\cdot$
$\cdot r_{L2}](1-D)^2+ C_2L_2r_{L1}^2+C_1L_1Rr_{L1}+C_2L_1r_{L1}r_{L2}+C_1C_2Rr_{L1}^2r_{L2}$

$d_1 =L_1r_{L1}+C_1Rr_{L1}^2+C_2r_{L1}^2r_{L2}+[L_1r_{L2}+L_2r_{L1}+C_2Rr_{L1}^2+ +C_2r_{L1}r_{L2}^2+2C_1Rr_{L1}r_{L2}](1+$
$-D)^2+[L_1R+L_2r_{L2}+C_1R^2r_{L1}+C_1Rr_{L2}^2+2C_2Rr_{L1}r_{L2}](1D)^4+[L_2R+C_1R^2r_{L2}+C_2 R^2$
$r_{L1}](1-D)^6$

$d_0 = r_{L1}^2+[2r_{L1}r_{L2}](1-D)^2+[r_{L2}+2Rr_{L1}](1-D)^4+2Rr_{L2}(1-D)^6+R^2(1-D)^8$

If the ESRs of the capacitors are not nulls, the transfer function of the converter assumes the same structure of equation (91), but the coefficient n_4 is not null and the other terms are more complex. For this reason only the case with null ESR capacitor have been shown.

3.2. Hammerstein Model

System identification is the branch of the system theory that seeks to obtain an appropriate mathematical model of a dynamic system on the basis of observed time series and a priori knowledge of the system.

Nonlinear systems are often represented as the interconnection of Linear Time Invariant (LTI) systems and static nonlinearities. These model structures, called *block oriented models*, have the ability to represent the dynamics of a large class of non-linear systems. Moreover, they have several advantages: low cost in identification tests; low cost in identification computation; easy use of the a priori knowledge in the model; easy use in control application.

The most simple and common structures are the Hammerstein model (HM), the Wiener model (WM) and their combination (Hammerstein-Wiener model). In the HM structure there is a memory-less nonlinearity followed by a LTI system. On contrary, in the WM the LTI model is followed by the static nonlinear function. Despite their simplicity, these structures accurately describe a wide variety of non-linear systems: electrical drives (Balestrino et al. 2001), solid oxide fuel cells (Jurado 2006), biomedical systems (Dempsey & Westwick 2004), biological systems (Hunter & Korenberg 1986), etc. As result, they have attracted much interest in the control and identification area.

The modeling of the QBCs and all the switching converters with an order higher than the second one exhibits the following challenges:

- The analytical linear transfer function is cumbersome to be obtained by the SSA technique since several reactive components are presents;
- The transfer function is non-linear versus the duty-cycle

Moreover, using the SSA technique all the power devices are assumed ideals and free of auxiliary circuits, i.e. snubber circuits. The Hammerstein approach can easy face up these challenges because it allows to modeling a switching converter without detailed knowledge of the circuit. The Hammerstein model represents the DC/DC switching model with a memory-less nonlinearity followed by a linear discrete-time and time-invariant model as it is shown in Figure 31. In Figure 31, $u(k)$ is the input variable (i.e. the duty-cycle), $f(u)$ is the memory-less nonlinear function, $x(k)$ is a

non-accessible intermediate variable and finally *y*(*k*) is the output of the dynamic LTI system (i.e. the output voltage) and it is measurable.

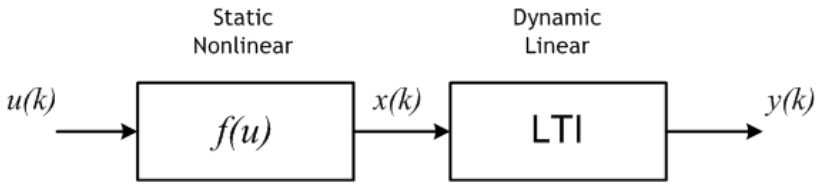

Figure 31 Hammerstein model structure.

H1) The Hammerstein approach can be used if and only if the system is asymptotically stable, which implies that the LTI system is asymptotically stable as well.

By considering an autoregressive model with exogenous input (ARX model), the linear dynamic can be modeled as:

$$\alpha(q)y(k) = \beta(q)x(k) + e(k) \tag{92}$$

where

$x(k) = f(u(k))$;

$\alpha(q) = 1 + a_1 q^{-1} + a_2 q^{-2} + \cdots + a_{n_\alpha} q^{-n_\alpha}$;

$\beta(q) = b_0 + b_1 q^{-1} + b_2 q^{-2} + \cdots + b_{n_\beta} q^{-n_\beta}$;

in which q^{-1} is the unit delay operator, n_α and n_β defines the order of the ARX model, $x(k)$and $y(k)$ are the input and output voltage of the linear part of the HM, and finally $e(k)$ is the system noise that takes into account modeling approximations and measurement noise. The system noise is assumed to be a white stochastic process with zero mean and variance σ^2.

Since the variable *x* is inaccessible, it is convenient to put the gain of the LTI system equal to 1. This implies that the nonlinear characteristic *f*(*u*) represents the static characteristic of the whole system which completely describes the steady-state behavior of the converter. It follows that the Hammerstein model is able to correctly describe the steady-state behavior of the converter. This is an advantage of the Hammerstein modeling over the conventional small-signal modeling.

In the case of the ARX model, the gain is equal to:

$$K_{ARX} = \lim_{z=1} \frac{Y(z)}{X(z)} = \lim_{z=1} \frac{\beta(z)}{\alpha(z)} = \frac{b_0+b_1+\cdots+b_{n_\beta}}{1+a_1+\cdots+a_{n_\alpha}}=1 \quad (93)$$

The gain constraint implies a parameter constraint in one of the coefficient of $\alpha(q)$ and $\beta(q)$, i.e. b_0:

$$b_0 = 1 + a_1 + \cdots + a_{n_\alpha} - (\, b_1 + \cdots + b_{n_\beta}) \quad (94)$$

The procedure of identification of Hammerstein model is essentially made-up of two steps. In the first, the *f*(*u*) is identified; some input–output couples (U_i, Y_i) of the nonlinear static characteristic are obtained by supplying the converter with constant inputs U_i and measuring the corresponding output Y_i at the steady-state. The identification of the non-linear part of the HM is possible thanks to the stability property (*H1*).

In the second step, the LTI model is identified from a set of input–output data acquired during a transient generated by supplying the system with a suitable input, i.e. PRBS (Pseudo Random Binary Sequence). It should be borne in mind that the use of a PRBS to excite the dynamics of the system is widely used for identification purpose (i.e. (Alonge et al. 2008; Haber & Keviczky 1999; Fairweather et al. 2011; Kristinsson & Dumont 1992; Miao et al. 2005)). For the identification of switching converters by mean the HM the frequency of the PRBS have to guarantee the following equation:

$$f_{PRBS} = \frac{1}{\Delta} f_{sw} \qquad , \Delta \epsilon \mathbb{Z}^+ \quad (95)$$

whereas the sampling frequency of the data useful for the identification process have to satisfy the following:

$$f_{sampling} = \Gamma f_{sw} \qquad , \Gamma \epsilon \mathbb{Z}^+ \quad (96)$$

The identification problem consist in the evaluation of the parameter vector $\boldsymbol{p} = \left[a_1\, a_2 \ldots a_{n_\alpha}\, b_1\, b_2 \ldots b_{n_\beta}\right]^T$ so as to minimize the cost function $J = \sum_{k=k_i}^{k_i+N} e^2(k)$ where N is the number of input-output measurements that are executed at the instants $k = k_i + 1, \ldots, k_i + N$ with $N \gg n_\alpha + n_\beta$. Substituting the expression of b_0, eq. (94), in equation (92) we can write that:

$$y(k) - x(k) = a_1[x_k - y_{k-1}] + \cdots + a_{n_\alpha}\left[x_k - y_{k-n_\alpha}\right] + b_1[x_{k-1} - x_k] +$$

$$+\cdots+b_{n_\beta}\left[x_{k-n_\beta}-x_k\right]+e(k)$$

Putting $\tilde{y}(k)=y(k)-x(k)$, the following regression model is obtained:

$$\tilde{y}=\boldsymbol{F}\boldsymbol{p}+e \tag{97}$$

where:

$\tilde{y}=[\,\tilde{y}(k_i+1)\ldots\ \tilde{y}(k_i+N)]^T$

$\boldsymbol{F}=[\boldsymbol{r}(k_i+1)\ldots\boldsymbol{r}(k_i+N)]^T$

$e=[e(k_i+1)\ldots\ e(k_i+N)]^T$

$\boldsymbol{r}=[\boldsymbol{r_a}^T\ldots\boldsymbol{r_b}^T]^T$

$\boldsymbol{r_a}^T=\left[x_k-y_{k-1}\ldots\ x_k-y_{k-n_\alpha}\right]$

$\boldsymbol{r_b}^T=\left[x_{k-1}-x_k\ldots\ x_{k-n_\beta}-x_k\right]$

The solution of the above identification problem is given by an Ordinary Least Squares (OLS) form where is present the left pseudo-inverse of the regressor $\boldsymbol{F}$:

$$\boldsymbol{p}=(\boldsymbol{F}^T\boldsymbol{F})^{-1}\boldsymbol{F}^T\tilde{y} \tag{98}$$

3.3. Conclusion

In this chapter, the main modeling techniques of DC/DC switching converters have been presented. Using the known information of the system and writing the Kirchhoff equations it is possible to obtain the SSA model that describes the average behavior of the system if the converter works in CCM. Usually, using this approach the power devices are assumed ideals especially for more complex converters (order of the system higher than the second degree). The knowledge of the non-linear system can be used to design nonlinear model based controllers. Standard or advanced linear controllers can be used if the SSA model is linearized around an operating point. The analytical SSA model, small-signal model and static gain of the two proposed QBCs have been presented. All these analytical results have been evaluated considering the ESR of the inductors and the capacitors.

In the second part of the chapter, the theoretical framework of the Hammerstein model identification has been discussed. The output of the identification process is a numerical nonlinear model composed by a memoryless nonlinearity and a LTI

system with unitary gain. The identification approach depends on the order of the converter but allows to easy treating the real behavior of the power devices (model and auxiliary circuits).

Chapter 4

Hammerstein Modeling of QBC1

4.1. Introduction

In this section the Hammerstein approach is used to identify the non-linear model of the *QBC1*. Unlike the SSA modeling approach, the HM is carried out by means input-output data sets; therefore the identification process is numerical.

The rated parameters of the *QBC1* are shown in Table 2.

Table 2 Rated circuit parameter of the *QBC1*.

Symbol	Description	Values	
V_{IN}	Input voltage	30	[V]
L_1	Input inductance	1.48	[mH]
r_{L1}	Parasitic resistance of L_1	40	[mΩ]
L_2	Middle inductance	1.7	[mH]
r_{L1}	Parasitic resistance of L_2	0.8	[Ω]
C_1, C_2	Output capacitances	100	[uF]
$r_{C1,}\, r_{C2}$	Parasitic resistance of C_1 and C_2	318	[mΩ]
f_{sw}	Switching frequency	20	[KHz]
R	Load	175	[Ω]
r_{ON}	Forward resistance of IGBT	100	[mΩ]
P_n	Rated Power	300	[W]

4.2. Nonlinear static characteristic identification

For the converter sketched in Figure 22, whose parameters are shown in Table 2, the static characteristics shown in Figure 32 were experimentally obtained, after supplying the converter with a set of pulse signals of different duty cycles, having switching frequency equal to 20 kHz. The solid line represents the static characteristic computed by the model (eq. (84)), including parasitic components. Some experimentally measured points are superimposed to this characteristic, which

confirm the validity of the theoretic analysis. As expected, the ideal characteristic, computed by means of (24), differs from the real one. Therefore, the identified model at the steady-state represents very well the real circuit under test.

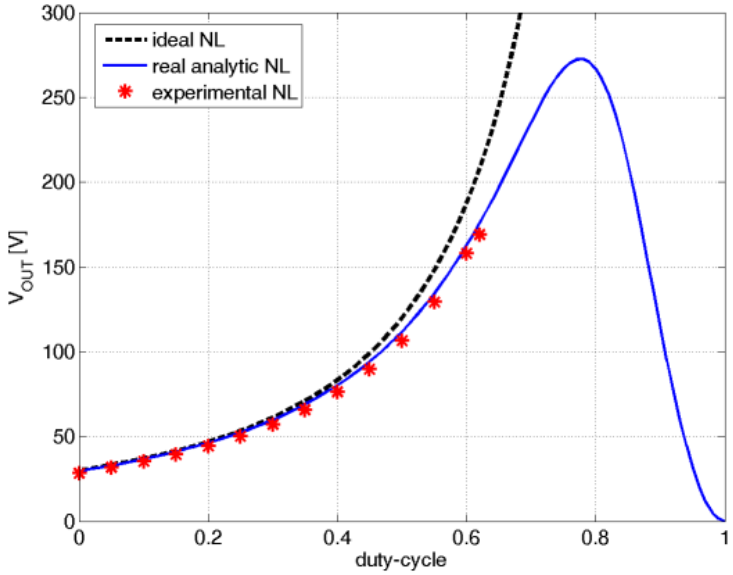

Figure 32 Nonlinear static characteristic of the *QBC1* for R=175Ω.

4.3. LTI model identification

The LTI model considered to describe the dynamic of the *QBC1* is the autoregressive model with exogenous input. The choice of the ARX model, rather than an ARMAX, is based on the consideration that the error dynamics cannot be known with sufficient precision to be included in the modeling process. In this way it is preferable to simplify the approach by using an ARX model. Moreover, not even a NARX model has been considered, since the Hammerstein approach allows the nonlinearity to be treated separately. In this way, the synthesis of the controller is made simpler because it can be referred to a LTI model.

In order to identify $\beta(q)$ and $\alpha(q)$, the range of admissible duty-cycle has been subdivided in 8 intervals. In each interval, a PRBS was generated with the voltage values, $f(D_i)$ and $f(D_{i+1})$, corresponding to the values of the duty-cycles which delimitate the interval itself. Then, a set of couples (t_k, y_k) was experimentally acquired together with the couples $(t_k, f(D))$ with $f(D) \in \{f(D_i), f(D_{i+1})\}$. Finally,

the set of acquired data was processed by means of the ordinary least square method, thus obtaining the coefficients of $\beta(q)$ and $\alpha(q)$.

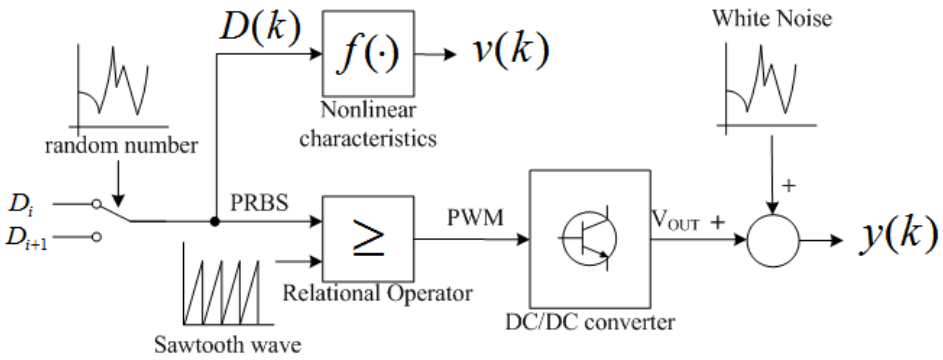

Figure 33 Block scheme for LTI identification purpose.

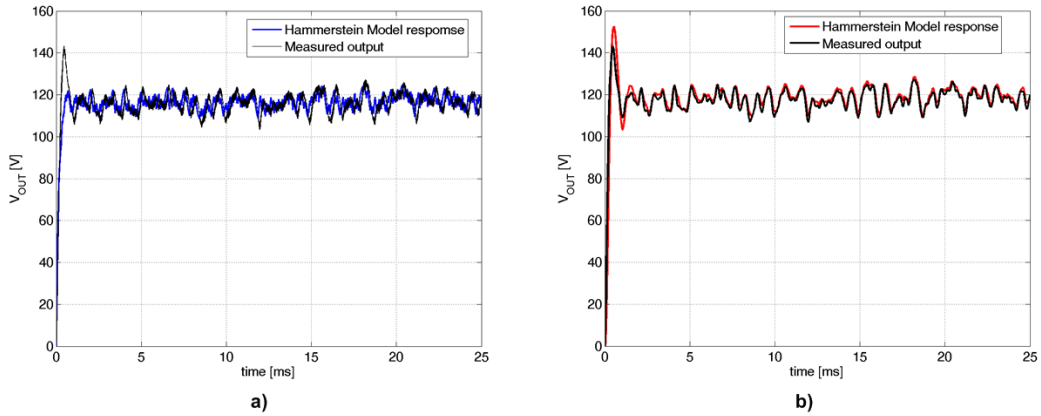

Figure 34 Response of two Hammerstein models: a) data acquired at 200 KHz; b) data acquired at 20 KHz.

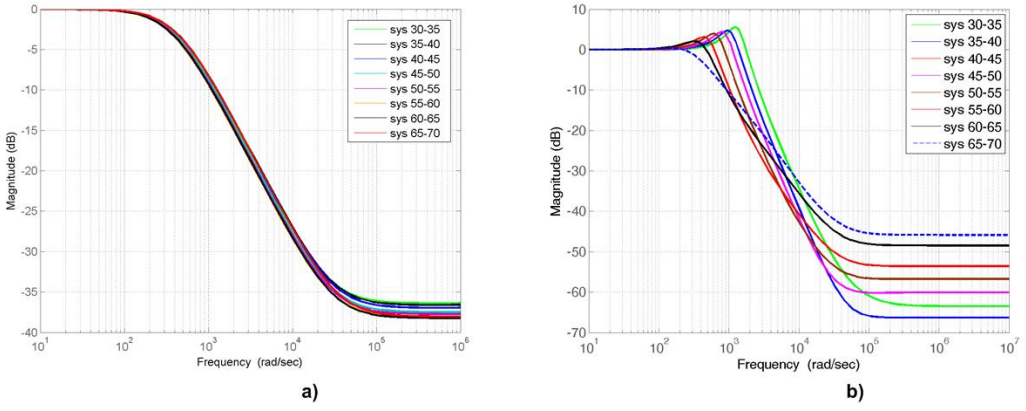

Figure 35 Bode diagrams of the eight identified ARX models: a) $T_s<T_{sw}$; b) $T_s=T_{sw}$.

The block diagram of the identification scheme is provided in Figure 33. The identification has been performed by choosing a fourth-order ARX model ($n_\alpha = 4$ and $n_\beta = 4$). This choice is justified considering that the *QBC1* converter contains

four reactive elements; however, the validation process allows to verify the correctness of the chosen order.

Particular care has to be reserved to the choice of the sampling time T_s of the system. As a matter of fact, T_s strongly influences the identified dynamics of the system and therefore the parameters of the identified transfer function. If T_s is selected equal to T_{sw}, a filtering action on the switching is introduced, which gives filtered data to the regression matrix, and then OLS can be successfully applied to identify the mean behaviour of the converter. On the contrary, if T_s is lower than T_{sw}, the above filtering action disappears and the results obtained using OLS method deteriorate. This is shown in Figure 34 and Figure 35, where the results obtained from the models identified using data in the range $D \in [0.5, 0.55]$, with $T_s = T_{sw}$ and $T_s = T_{sw}/10$, are shown.

In particular, Figure 34 a) and Figure 34 b) show the time domain curves, respectively with $T_s = T_{sw}/10$ (Figure 34 a)) and $T_s = T_{sw}$ (Figure 34 b)). Figure 34 a) clearly shows that the identified system is able to properly tracks the very fast transient caused by the switching while it has lost the information about the main dynamics of the system since it is not able to properly track the first transient of the system. As a matter of fact, the identified system is overdamped while the real system is underdamped. On the contrary, Figure 34 b) shows that, adopting $T_s = T_{sw}$, the system is able to track the main dynamics since the identified system is correctly underdamped. At the same time, the identified system will not be able to track fast variations caused by the switching. This is confirmed by Figure 35 a) and Figure 35 b) showing the Bode diagram of the transfer functions respectively in the case $T_s = T_{sw}/10$ (Figure 35 a)) and $T_s = T_{sw}$ (Figure 35 b)). In the first case the identified main dynamics is governed by the real poles (overdamped system) and it is independent from the duty cycle range. In the second case the identified main dynamics is governed by two complex conjugate poles (underdamped system) with a resonance peak increasing at the decreasing of the values of the duty cycle. There is also a spread of the magnitude curves at high frequency, but this occurs in a region in which the magnitude is under -40 dB.

The discrete-time transfer function obtained as already said, in the case $T_s=T_{sw}$, are sketched in Table 3. It can be observed that all the eight transfer functions are non-minimum phase. Since the non-minimum phase behavior of the boost converter is well known, this result confirms the correctness of the identification process.

Table 3 Discrete transfer functions of the eight ARX models.

Duty-Cycle	Transfer Function $G_p(z)$
[0.30, 0.35]	$\frac{6.416\cdot10^{-5}\,z^4+3.596\cdot10^{-3}\,z^3+5.187\cdot10^{-5}\,z^2-9.324\cdot10^{-4}\,z-1.403\cdot10^{-4}}{z^4-2.172z^3+1.19z^2+0.168z-0.1833}$
[0.35, 0.40]	$\frac{1.645\cdot10^{-4}\,z^4+4.845\cdot10^{-4}\,z^3+1.878\cdot10^{-3}\,z^2-4.208\cdot10^{-4}\,z-4.294\cdot10^{-5}}{z^4-2.107z^3+1.121z^2+0.1083z-0.1208}$
[0.40, 0.45]	$\frac{1.503\cdot10^{-4}\,z^4+4.741\cdot10^{-4}\,z^3+1.83\cdot10^{-3}\,z^2-4.4487\cdot10^{-4}\,z-7.938\cdot10^{-5}}{z^4-2.122\,z^3+1.136z^2+0.124z-0.1361}$
[0.45, 0.50]	$\frac{1.304\cdot10^{-4}\,z^4-9.676\cdot10^{-4}\,z^3+2.682\cdot10^{-3}\,z^2-3.318\cdot10^{-4}\,z-1.593\cdot10^{-4}}{z^4-2.125z^3+1.138z^2+0.1216z-0.1341}$
[0.50, 0.55]	$\frac{1.102\cdot10^{-4}\,z^4-2.303\cdot10^{-3}\,z^3+3.509\cdot10^{-3}\,z^2-2.165\cdot10^{-4}\,z-3.226\cdot10^{-4}}{z^4-2.15z^3+1.156z^2+0.1559z-0.161}$
[0.55, 0.60]	$\frac{9.057\cdot10^{-5}\,z^4-3.875\cdot10^{-3}\,z^3+4.906\cdot10^{-3}\,z^2-1.187\cdot10^{-4}\,z-6.166\cdot10^{-4}}{z^4-2.189z^3+1.194z^2+0.1918z-0.1964}$
[0.60, 0.65]	$\frac{1.286\cdot10^{-4}\,z^4-7.453\cdot10^{-3}\,z^3+8.916\cdot10^{-3}\,z^2+1.864\cdot10^{-5}\,z-1.395\cdot10^{-3}}{z^4-2.23z^3+1.233z^2+0.236z-0.2384}$
[0.65, 0.70]	$\frac{1.216\cdot10^{-4}\,z^4-1.036\cdot10^{-2}\,z^3+1.261\cdot10^{-2}\,z^2+2.589\cdot10^{-4}\,z-2.548\cdot10^{-3}}{z^4-2.292z^3+1.29z^2+0.305z-0.3029}$

4.4. Comparison between SSA and HM modeling

While the SSA is able to reproduce only the mean, in a switching period, of the converter, the Hammerstein model can identify different dynamics according to the switching period and excitation signal. This requires that particular care has to be posed in designing the experiment to be used for identification.

In synthesis the main differences between SSA and Hammerstein approaches are the following:

The SSA approach leads to a linear small-signal model, describing the true nonlinear model in a little neighborhood of a given equilibrium point, which does not appear explicitly in the model but it is implicitly included in its parameters. As a consequence, the small-signal model describes with sufficient care the transients for small signals around the equilibrium point but it does not describe steady-state behavior at all. On the contrary, the Hammerstein model is a nonlinear mapping

followed by a linear model. The static nonlinearity accurately describes the steady-state behavior, whereas the linear model accurately describes the transients in a certain region of the state space. To enlarge the region of the state space of validity of the Hammerstein model, a set of transfer functions can be identified each of them being valid in a certain interval of the space state.

The small-signal model strictly depends on the rated parameters of the converter. In order to obtain an accurate model, it is then necessary to consider the real physical model of each device of the converter. Furthermore, many physical parameters of the converters could be not easily measurable, like the parasitic resistances. In general there is a significant spreading of the parameters that can affect the modeling as well. Often, for avoiding complexity in the analysis, several simplifying hypotheses are made. The Hammerstein model, on the contrary, reproduces the real behavior of the system without any underline approximation. More precisely, this approach allows to include in the model the parasitic components of the system and its auxiliary circuits, i.e. snubber circuit, very easily.

As it is clearly observable from Figure 35, the dc-gain of the LTI model is well defined and equal to 1, independently from the duty-cycle. Consequently, it is easy to define the uncertainty as a function of the frequency: it is null at zero frequency, then increases with frequency and it can be considered constant above a certain frequency. On the contrary, using SSA method, the small-signal models display a gain which strongly depends on the duty-cycle, as shown in Figure 36. This implies that the uncertainty is high also at low frequency, meaning that the low-signal model is not properly suited for applying the frequency-domain robust control techniques, if the whole operating range of the converter has to be taken into account. A direct comparison of Figure 35 b) and Figure 36 shows that the same kind of resonance is present in both the considered models, in the same frequency range (about 1000 rad/s). However, while the HM exhibits the Bode diagram of a second-order underdamped system, the SSA model displays a more irregular frequency response. This is confirmed by the zero-pole maps of SSA and HMs referred, respectively, to small-signal variations around D=0.65 and to the range $D \in [0.6, 0.65]$ (cf. Figure 37). Examination of Figure 37 shows that the complex conjugate low frequency poles and the real positive zero at low frequency are practically (in the given scale) at

the same position in both models. The remaining part of the map shows for the SSA two couples of complex conjugate pole-zero very closer each other (they tend to nullify their effect). Correspondingly, with the Hammerstein approach a couple pole-zero exist at high frequency (they tend to nullify their effect). As for the rest, while the SSA shows a real negative high frequency zero, the Hammerstein model shows a positive zero. This would imply a completely different behavior as the phase rotation is concerned; it is to be observed however that the frequency range in which the zeros act is so high with respect to the band of the control system that their contribution can be considered not relevant.

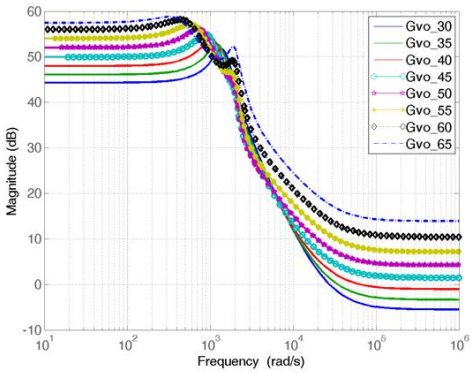

Figure 36 Bode diagrams of the eight small-signal models.

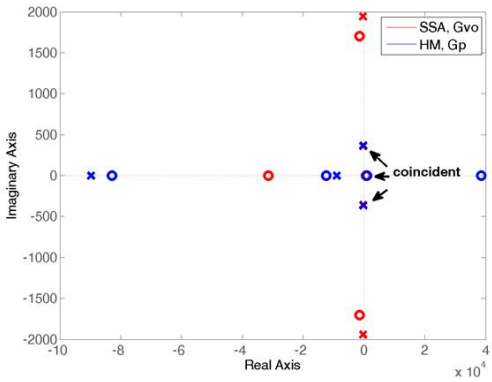

Figure 37 Poles and zeros maps of: G_{vo} in D=0.65; G_p in D∈[0.6, 0.65].

4.5. Conclusion

In this chapter a numerical example of the Hammerstein approach have been presented; more exactly, the HM of the *QBC1*. The HM of the *QBC1* converter has been compared with the relative SSA model. The comparison of the two models confirms the validity of the two different modeling approaches.

Chapter 5

Hybrid Modeling

5.1. Introduction

The SSA approach for the study of switching converter was introduced by (MIDDLEBROOK & ĆUK 1976) , and then it was used in literature to describe the average behavior of these nonlinear systems. However, this approach presents some approximations that can be neglected for elementary schemes of power converters, but cannot be neglected a priori for more complex topology. To this regard, we will describe a general rigorous analysis of the SSA approach in order to show the approximations that this type of modeling produces, and it is demonstrated that often this approach fails giving a wrong behavior of the system especially during transient.

5.2. Limits of the Averaged Model

The goal of this section will be to verify if the equivalent nonlinear model for DC/DC converter (75) well represents the mean behavior of the real system. For mean behavior it is intended that the values of the state at the generic discrete time instants $\boldsymbol{x}(kT_{sw})$ and $\boldsymbol{x}((k+1)T_{sw})$ coincide.

Given the state at the generic discrete time instants $\boldsymbol{x}(kT_{sw})$, for $t \in [kT_{sw},\ kT_{sw} + T_{ON})]$ the system works in *on mode* ant its evolution of the state is the trajectory solution of the set of differential equation given in (73) with initial condition $\boldsymbol{x}(kT_{sw})$. It is well known from the theory of the linear systems that the state evolution for (73) is (in the following $T_{sw} = T$):

$$\boldsymbol{x}(t) = e^{\boldsymbol{A_{on}}(t-kT)}\boldsymbol{x}(kT) + \int_{kT}^{t} e^{\boldsymbol{A_{on}}(t-\tau)}\boldsymbol{B_{on}}u(\tau)d\tau \qquad \forall t \in [kT, kT + T_{ON}] \qquad (99)$$

Defining $\zeta = t - \tau$, and taking into consideration that $\frac{d}{d\zeta} = e^{\boldsymbol{A_{on}}\zeta}\boldsymbol{B_{on}}$, then if $det\boldsymbol{A_{on}} \neq 0 \Rightarrow e^{\boldsymbol{A_{on}}\zeta}\boldsymbol{B_{on}} = \boldsymbol{A_{on}}^{-1}\frac{d}{d\zeta}(e^{\boldsymbol{A_{on}}\zeta}\boldsymbol{B_{on}})$. Moreover, the input $u(\tau)$ is assumed to be constant and equal to U; this assumption is reasonable in a DC/DC converter. Under these considerations (99) can be written as:

$$\boldsymbol{x}(t) = e^{\boldsymbol{A_{on}}(t-kT)}\boldsymbol{x}(kT) + \int_0^{t-kT} e^{\boldsymbol{A_{on}}\zeta}\boldsymbol{B_{on}}U d\zeta =$$

$$= e^{\boldsymbol{A_{on}}(t-kT)}\boldsymbol{x}(kT) + \boldsymbol{A_{on}}^{-1}(e^{\boldsymbol{A_{on}}(t-kT)} - \boldsymbol{I})\boldsymbol{B_{on}}U \tag{100}$$

Using (100), the state at the instant $t = kT + T_{ON}$ is:

$$\boldsymbol{x}(kT + T_{ON}) = e^{\boldsymbol{A_{on}}T_{ON}}\boldsymbol{x}(kT) + \boldsymbol{A_{on}}^{-1}(e^{\boldsymbol{A_{on}}T_{ON}} - \boldsymbol{I})\boldsymbol{B_{on}}U \tag{101}$$

Now, for $t \in [kT + T_{ON},\ (k+1)T)]$, the system works in *off mode* and its evolution of the state is the trajectory of the set of differential equations given in (74) with initial condition $\boldsymbol{x}(kT + T_{ON})$. Using the same procedure, we obtain:

$$\boldsymbol{x}(t) = e^{\boldsymbol{A_{off}}(t-kT-T_{ON})}\boldsymbol{x}(kT + T_{ON}) + \int_{kT+T_{ON}}^{t} e^{\boldsymbol{A_{off}}(t-\tau)}\boldsymbol{B_{off}}u(\tau)d\tau \quad \forall t \in [kT + T_{ON},\ (k+1)T] \tag{102}$$

If exists the inverse of $\boldsymbol{A_{off}}$, $det(\boldsymbol{A_{off}}) \neq 0$, replacing (101) in (102) the following equation is obtained:

$$\boldsymbol{x}\big((k+1)T\big) = e^{\boldsymbol{A_{off}}(t-kT-T_{ON})}\big(e^{\boldsymbol{A_{on}}T_{ON}}\boldsymbol{x}(kT) + \boldsymbol{A_{on}}^{-1}(e^{\boldsymbol{A_{on}}T_{ON}} - \boldsymbol{I})\boldsymbol{B_{on}}U\big) + \\ + \boldsymbol{A_{off}}^{-1}\big(e^{\boldsymbol{A_{off}}(T-T_{ON})} - \boldsymbol{I}\big)\boldsymbol{B_{off}}U \tag{103}$$

Particularizing (103) for $t = (k+1)T$, the value of the state at the end of the switching period is given by:

$$\boldsymbol{x}\big((k+1)T\big) = e^{\boldsymbol{A_{off}}(1-D)T}e^{\boldsymbol{A_{on}}DT}\boldsymbol{x}(kT) + (e^{\boldsymbol{A_{off}}(1-D)T}\boldsymbol{A_{on}}^{-1}(e^{\boldsymbol{A_{on}}DT} - \boldsymbol{I})\boldsymbol{B_{on}} + \\ + \boldsymbol{A_{off}}^{-1}\big(e^{\boldsymbol{A_{off}}(1-D)T} - \boldsymbol{I}\big)\boldsymbol{B_{off}})U \tag{104}$$

Using the properties of the exponential matrix, $\boldsymbol{A_{on}}^{-1}e^{\boldsymbol{A_{on}}DT}$ becomes:

$$\boldsymbol{A_{on}}^{-1}e^{\boldsymbol{A_{on}}DT} = \boldsymbol{A_{on}}^{-1}e^{\boldsymbol{A_{on}}DT}\boldsymbol{A_{on}}\boldsymbol{A_{on}^{-1}} = e^{\boldsymbol{A_{on}^{-1}}\boldsymbol{A_{on}}DT\boldsymbol{A_{on}}}\boldsymbol{A_{on}^{-1}} = e^{\boldsymbol{A_{on}}DT}\boldsymbol{A_{on}^{-1}}$$

and similarly:

$$\boldsymbol{A_{off}}^{-1}e^{\boldsymbol{A_{off}}DT} = e^{\boldsymbol{A_{off}}DT}\boldsymbol{A_{off}^{-1}}$$

Using these two last considerations, (104) can be rewritten as:

$$\boldsymbol{x}\big((k+1)T\big) = e^{\boldsymbol{A_{off}}(1-D)T}e^{\boldsymbol{A_{on}}DT}\boldsymbol{x}(kT) + e^{\boldsymbol{A_{off}}(1-D)T}e^{\boldsymbol{A_{on}}DT}\boldsymbol{A_{on}^{-1}}\boldsymbol{B_{on}}U + \\ + e^{\boldsymbol{A_{off}}(1-D)T}\big(-\boldsymbol{A_{on}^{-1}}\boldsymbol{B_{on}} + \boldsymbol{A_{off}^{-1}}\boldsymbol{B_{off}}\big)U - \boldsymbol{A_{off}^{-1}}\boldsymbol{B_{off}}U \tag{105}$$

The equation (105) is the value of the state $\boldsymbol{x}\big((k+1)T\big)$ given initial condition $\boldsymbol{x}(kT)$, duty-cycle D, and switching period T. This relation is an exact relation and always exists when the dynamic matrices are non-singular ($\boldsymbol{A_{on}}$ and $\boldsymbol{A_{off}}$).

This analysis should lead at the same state, (105), for given initial condition $\boldsymbol{x}(kT)$, if an equivalent analysis for the SSA model (75) is carry out, and if the mean behavior of the system is effectively described. Indeed, for mean behavior is intended that the values of the state can change during a switching period, but their values at the generic instants $\boldsymbol{x}(kT)$ and $\boldsymbol{x}\big((k+1)T\big)$ must coincide.

Applying the same procedure used above to the SSA model, the state at the instant $t = (k+1)T$, starting from $\boldsymbol{x}(k\mathrm{T})$, is:

$$\boldsymbol{x}\big((k+1)T\big) = e^{\boldsymbol{A}T}x(kT) + \boldsymbol{A}^{-1}(e^{\boldsymbol{A}T} - \boldsymbol{I})\boldsymbol{B}U \tag{106}$$

where: $\boldsymbol{A} = \boldsymbol{A_{on}}D + \boldsymbol{A_{off}}(1-D)$ and $\boldsymbol{B} = \boldsymbol{B_{on}}D + \boldsymbol{B_{off}}(1-D)$.

The equivalence between (106) and (105) is not a trivial task, and in general they are not the same. The first term of the (105), that corresponds to the free response of the system, is equal to the first term of (106) if the $\boldsymbol{A_{on}A_{off}} = \boldsymbol{A_{off}A_{on}}$. Therefore, if the product of the two dynamic matrices is commutative, then:

$$e^{\boldsymbol{A_{off}}(1-D)T}e^{\boldsymbol{A_{on}}DT}\boldsymbol{x}(kT) = e^{\boldsymbol{A_{off}}(1-D)T+\boldsymbol{A_{on}}DT}\boldsymbol{x}(kT) = e^{\boldsymbol{A}T}\boldsymbol{x}(kT)$$

So a first condition for the equivalence in free evolution is:

$$\boldsymbol{A_{on}A_{off}} = \boldsymbol{A_{off}A_{on}} \tag{107}$$

It should be noted that usually the equation (107) is not satisfied also for simple converter schemes. For instance, for the ideal Boost converter analyzed in Appendix A of (MIDDLEBROOK & ĆUK 1976) is highlighted that proposed averaged model is an approximated averaged model because $\boldsymbol{A_{on}A_{off}} \approx \boldsymbol{A_{off}A_{on}}$.

A further remark is in the consideration of the non-idealities of the converter. If the dynamic matrices contains terms due to parasitic resistances, then these terms will be neglected when (107) is used; so the modeling effort vanishes when the averaged model is used. For this reason, theoretically, if the SSA model is used, the non-ideal model can only be used to compute the converter gain with more accuracy, but it cannot be used in order to increase the model accuracy during transient.

The terms that contain the input U in (105) and (106) are considered. If the condition (107) is used, then the terms in (105) become:

$$(e^{\boldsymbol{A}T}\boldsymbol{A_{on}^{-1}B_{on}} + e^{\boldsymbol{A_{off}}(1-D)T}\big(\boldsymbol{A_{off}^{-1}B_{off}} - \boldsymbol{A_{on}^{-1}B_{on}}\big) - \boldsymbol{A_{off}^{-1}B_{off}})U \tag{108}$$

From a direct comparison it is evident that the forcing terms cannot be compared even if the condition (107) is satisfied. Anyway, a comparison can be done between the first order terms of the Taylor series of these terms. More exactly, considering that for T sufficiently small $e^{\boldsymbol{AT}} \approx \mathbf{I} + \boldsymbol{AT}$, then the term $\boldsymbol{A}^{-1}(e^{\boldsymbol{AT}} - \mathbf{I})\boldsymbol{B}U$ can be linearized as:

$$\boldsymbol{A}^{-1}(e^{\boldsymbol{AT}} - \boldsymbol{I})\boldsymbol{B}U \approx \boldsymbol{B}TU \tag{109}$$

while (108) can be linearized as:

$$\begin{aligned}
&\left(e^{\boldsymbol{AT}}\boldsymbol{A}_{\boldsymbol{on}}^{-1}\boldsymbol{B}_{\boldsymbol{on}} + e^{\boldsymbol{A}_{\boldsymbol{off}}(1-D)T}\left(\boldsymbol{A}_{\boldsymbol{off}}^{-1}\boldsymbol{B}_{\boldsymbol{off}} - \boldsymbol{A}_{\boldsymbol{on}}^{-1}\boldsymbol{B}_{\boldsymbol{on}}\right) - \boldsymbol{A}_{\boldsymbol{off}}^{-1}\boldsymbol{B}_{\boldsymbol{off}}\right)U \approx \\
&\approx [\left(\boldsymbol{I} + \boldsymbol{A}_{\boldsymbol{on}}DT + \boldsymbol{A}_{\boldsymbol{off}}(1-D)T\right)\boldsymbol{A}_{\boldsymbol{on}}^{-1}\boldsymbol{B}_{\boldsymbol{on}} + \left(\boldsymbol{I} + \boldsymbol{A}_{\boldsymbol{off}}(1-D)T\right)\left(\boldsymbol{A}_{\boldsymbol{off}}^{-1}\boldsymbol{B}_{\boldsymbol{off}} - \boldsymbol{A}_{\boldsymbol{on}}^{-1}\boldsymbol{B}_{\boldsymbol{on}}\right) + \\
&\quad \boldsymbol{A}_{\boldsymbol{off}}^{-1}\boldsymbol{B}_{\boldsymbol{off}}]U = \\
&\quad = [\boldsymbol{A}_{\boldsymbol{on}}^{-1}\boldsymbol{B}_{\boldsymbol{on}} + \boldsymbol{B}_{\boldsymbol{on}}DT + \boldsymbol{A}_{\boldsymbol{off}}\boldsymbol{A}_{\boldsymbol{on}}^{-1}\boldsymbol{B}_{\boldsymbol{on}}(1-D)T + \boldsymbol{A}_{\boldsymbol{off}}^{-1}\boldsymbol{B}_{\boldsymbol{off}} - \boldsymbol{A}_{\boldsymbol{on}}^{-1}\boldsymbol{B}_{\boldsymbol{on}} + \boldsymbol{B}_{\boldsymbol{off}}(1-D)T + \\
&\quad -\boldsymbol{A}_{\boldsymbol{off}}\boldsymbol{A}_{\boldsymbol{on}}^{-1}\boldsymbol{B}_{\boldsymbol{on}}(1-D)T - \boldsymbol{A}_{\boldsymbol{off}}^{-1}\boldsymbol{B}_{\boldsymbol{off}}]U = \boldsymbol{B}TU
\end{aligned} \tag{110}$$

From (109) and (110) it is evident that, under the condition $\boldsymbol{A}_{\boldsymbol{on}}\boldsymbol{A}_{\boldsymbol{off}} = \boldsymbol{A}_{\boldsymbol{off}}\boldsymbol{A}_{\boldsymbol{on}}$, the first order approximation is the same. Obviously, smaller is the switching period better is the approximation.

To sum up, in a switching period, for given initial condition $\boldsymbol{x}(kT)$, the free response of the averaged model is equal to the free response of the real system if (107) is satisfied. Moreover, under the same condition the first order approximation of the forcing term of the averaged model coincides with that one of the real system. For this consideration it can be concluded that the SSA model represents a good approximated averaged model of the real system if $\boldsymbol{A}_{\boldsymbol{on}}\boldsymbol{A}_{\boldsymbol{off}} = \boldsymbol{A}_{\boldsymbol{off}}\boldsymbol{A}_{\boldsymbol{on}}$ and T is as smaller as possible. The SSA is an exactly averaged model when $\boldsymbol{A}_{\boldsymbol{on}}\boldsymbol{A}_{\boldsymbol{off}} = \boldsymbol{A}_{\boldsymbol{off}}\boldsymbol{A}_{\boldsymbol{on}}$ and $T \to 0$. These means that, if the approximation (107) cannot be done, i.e. when complex topologies of converters are used, or when the converter works with asynchronous switching (the condition of small T cannot be guaranteed), then the average model fails in its mean description.

A final further consideration is that the proposed average model works only in continuous conduction mode, so it cannot be used when the converter works in discontinuous conduction mode.

In order to highlight the approximation of the SSA model, the traditional Boost converter and the quadratic boost converter *QBC1* have been analyzed in the ideal and real case.

5.2.1. Example 1: Boost Converter

In CCM, the Boost converter of Figure 4 is modeling by mean of (73) and (74) where the state vector $\boldsymbol{x} \in \Re^2$ and it is equal to $[i_L\ v_C]^T$. The scalar input $u \in \Re$ and it is equal to the voltage input supply.

In ideal case, the dynamic matrices of the Boost converter are equal to:

$$\boldsymbol{A_{on}} = \begin{bmatrix} 0 & 0 \\ 0 & -\frac{1}{CR} \end{bmatrix}, \boldsymbol{A_{off}} = \begin{bmatrix} 0 & -\frac{1}{L} \\ \frac{1}{C} & -\frac{1}{CR} \end{bmatrix},$$

and the product between A_{on} and A_{off} is not commutative because:

$$\boldsymbol{A_{on}A_{off}} = \begin{bmatrix} 0 & 0 \\ -\dfrac{1}{C^2R} & \dfrac{1}{(CR)^2} \end{bmatrix}$$

$$\boldsymbol{A_{off}A_{on}} = \begin{bmatrix} 0 & \dfrac{1}{LCR} \\ 0 & -\dfrac{1}{(CR)^2} \end{bmatrix}$$

In the real case, the dynamic matrices are equal to:

$$\boldsymbol{A_{on}} = \begin{bmatrix} -\frac{r_L}{L} & 0 \\ 0 & -\frac{1}{C\sigma_1} \end{bmatrix}, \boldsymbol{A_{off}} = \begin{bmatrix} -\frac{r_C r_L + R(r_C + r_L)}{L\sigma_1} & -\frac{R}{L\sigma_1} \\ \frac{R}{C\sigma_1} & -\frac{1}{C\sigma_1} \end{bmatrix},$$

with $\sigma_1 = R + r_C$. In the real case, the result is the same of the ideal one because:

$$\boldsymbol{A_{on}A_{off}} = \begin{bmatrix} \dfrac{r_L(r_C r_L + R(r_C + r_L))}{L^2\sigma_1} & \dfrac{Rr_L}{L^2\sigma_1} \\ -\dfrac{R}{(C\sigma_1)^2} & \dfrac{1}{(C\sigma_1)^2} \end{bmatrix}$$

$$\boldsymbol{A_{off}A_{on}} = \begin{bmatrix} \dfrac{r_L(r_C r_L + R(r_C + r_L))}{L^2\sigma_1} & \dfrac{R}{LC{\sigma_1}^2} \\ -\dfrac{Rr_L}{LC\sigma_1} & -\dfrac{1}{(C\sigma_1)^2} \end{bmatrix}$$

and only the diagonal terms are equals.

5.2.2. Example 2: QBC1

In continuous conduction mode, the *QBC1* is a 4th order system because the state vector $\boldsymbol{x} = [i_{L1}\ i_{L2}\ v_{C1}\ v_{C2}]^T \in \Re^4$. In ideal case, where all the parasitic components are nulls, if the capacitors C_1 and C_2 are equals to C, the dynamic matrices of (81) and (82) becomes:

$$\boldsymbol{A_{on}} = \begin{bmatrix} 0 & 0 & 0 & 0 \\ 0 & 0 & 0 & \frac{1}{L_2} \\ 0 & 0 & -\frac{1}{CR} & -\frac{1}{CR} \\ 0 & -\frac{1}{C} & -\frac{1}{CR} & -\frac{1}{CR} \end{bmatrix}$$

$$\boldsymbol{A_{off}} = \begin{bmatrix} 0 & 0 & 0 & -\frac{1}{L_1} \\ 0 & 0 & -\frac{1}{L_2} & 0 \\ 0 & \frac{1}{C} & -\frac{1}{CR} & -\frac{1}{CR} \\ \frac{1}{C} & 0 & -\frac{1}{CR} & -\frac{1}{CR} \end{bmatrix}$$

The dynamic matrices are not commutative:

$$\boldsymbol{A_{on}A_{off}} = \begin{bmatrix} 0 & 0 & 0 & 0 \\ \frac{1}{CL_2} & 0 & -\frac{1}{CL_2R} & -\frac{1}{CL_2R} \\ \delta_2 & \delta_2 & \delta_1 & \delta_1 \\ \delta_2 & \delta_2 & \delta_1 + \frac{1}{CL_2} & \delta_1 \end{bmatrix}$$

$$\boldsymbol{A_{off}A_{on}} = \begin{bmatrix} 0 & \frac{1}{CL_1} & \frac{1}{CL_1R} & \frac{1}{CL_1R} \\ 0 & 0 & \frac{1}{CL_2R} & \frac{1}{CL_2R} \\ 0 & -\delta_2 & \delta_1 & \delta_1 + \frac{1}{CL_2} \\ 0 & -\delta_2 & \delta_1 & \delta_1 \end{bmatrix}$$

where $\delta_1 = \frac{2}{(CR)^2}$ and $\delta_2 = -\frac{1}{C^2R}$.

In the real case similarly:

$$\boldsymbol{A_{on}} = \begin{bmatrix} -\frac{r_{L1}}{L_1} & 0 & 0 & 0 \\ 0 & -\frac{r_{L2}\delta_1 + r_C\delta_2}{L_2\delta_1} & -\frac{r_C}{L_2\delta_1} & \frac{\delta_2}{L_2\delta_1} \\ 0 & \frac{r_C}{C\delta_1} & -\frac{1}{C\delta_1} & -\frac{1}{C\delta_1} \\ 0 & -\frac{\delta_2}{C\delta_1} & -\frac{1}{C\delta_1} & -\frac{1}{C\delta_1} \end{bmatrix}$$

$$\boldsymbol{A_{off}} = \begin{bmatrix} -\frac{r_{L1}\delta_1 + r_C\delta_2}{L_1\delta_1} & \frac{{r_C}^2}{L_1\delta_1} & \frac{r_C}{L_1\delta_1} & -\frac{\delta_2}{L_1\delta_1} \\ \frac{{r_C}^2}{L_2\delta_1} & -\frac{r_{L2}\delta_1 + r_C\delta_2}{L_2\delta_1} & -\frac{\delta_2}{L_2\delta_1} & \frac{r_C}{L_2\delta_1} \\ -\frac{r_C}{C\delta_1} & \frac{\delta_2}{C\delta_1} & -\frac{1}{C\delta_1} & -\frac{1}{C\delta_1} \\ \frac{\delta_2}{C\delta_1} & -\frac{r_C}{C\delta_1} & -\frac{1}{C\delta_1} & -\frac{1}{C\delta_1} \end{bmatrix}$$

where $\delta_1 = R + 2r_C$ and $\delta_2 = R + r_C$. In real case the two products of the dynamic matrices are instead equals to:

$$\boldsymbol{A_{on}A_{off}} =$$

$$\begin{bmatrix} \frac{r_{L1}(r_{L1}\delta_1 + r_C\delta_2)}{{L_1}^2\delta_1} & -\frac{r_{L1}{r_C}^2}{{L_1}^2\delta_1} & \frac{r_{L1}r_C}{{L_1}^2\delta_1} & \frac{r_{L1}\delta_2}{{L_1}^2\delta_1} \\ -\frac{{r_C}^2C(r_{L2}\delta_1 + r_C\delta_2) + L_2({r_C}^2 + {\delta_2}^2)}{{L_2}^2{\delta_1}^2C} & \frac{C(r_{L2}\delta_1 + r_C\delta_2)^2 - 2L_2r_C\delta_2}{{L_2}^2{\delta_1}^2C} & \frac{\delta_2C(r_{L2}\delta_1 + r_C\delta_2) + L_2(r_C - \delta_2)}{{L_2}^2{\delta_1}^2C} & \frac{-Cr_C(r_{L2}\delta_1 + r_C\delta_2) + L_2(r_C - \delta_2)}{{L_2}^2{\delta_1}^2C} \\ \frac{Cr_C{}^3 + L_2(r_C - \delta_2)}{C^2{\delta_1}^2L_2} & \frac{-Cr_C(r_{L2}\delta_1 + r_C\delta_2) + L_2(r_C - \delta_2)}{C^2{\delta_1}^2L_2} & \frac{-Cr_C\delta_2 + 2L_2}{C^2{\delta_1}^2L_2} & \frac{Cr_C{}^2 + 2L_2}{C^2{\delta_1}^2L_2} \\ \frac{-\delta_2Cr_C{}^2 + L_2(r_C - \delta_2)}{C^2{\delta_1}^2L_2} & \frac{C\delta_2(r_{L2}\delta_1 + r_C\delta_2) + L_2(r_C - \delta_2)}{C^2{\delta_1}^2L_2} & \frac{C{\delta_2}^2 + 2L_2}{C^2{\delta_1}^2L_2} & \frac{-\delta_2Cr_C + 2L_2}{C^2{\delta_1}^2L_2} \end{bmatrix}$$

$$\boldsymbol{A_{off}A_{on}} =$$

$$\begin{bmatrix} \frac{r_{L1}(r_{L1}\delta_1 + r_C\delta_2)}{{L_1}^2\delta_1} & -\frac{{r_C}^2C(r_{L2}\delta_1 + r_C\delta_2) + L_2({r_C}^2 + {\delta_2}^2)}{L_1L_2{\delta_1}^2C} & \frac{-Cr_C{}^3 + L_2(\delta_2 - r_C)}{L_1L_2{\delta_1}^2C} & \frac{\delta_2Cr_C{}^2 + L_2(\delta_2 - r_C)}{L_1L_2{\delta_1}^2C} \\ -\frac{r_{L1}{r_C}^2}{L_1L_2\delta_1} & \frac{C(r_{L2}\delta_1 + r_C\delta_2)^2 - 2L_2r_C\delta_2}{{L_2}^2{\delta_1}^2C} & \frac{r_CC(r_{L2}\delta_1 + r_C\delta_2) + L_2(\delta_2 - r_C)}{{L_2}^2{\delta_1}^2C} & \frac{-C\delta_2(r_{L2}\delta_1 + r_C\delta_2) + L_2(\delta_2 - r_C)}{{L_2}^2{\delta_1}^2C} \\ \frac{r_{L1}r_C}{L_1C\delta_1} & \frac{-\delta_2C(r_{L2}\delta_1 + r_C\delta_2) + L_2(\delta_2 - r_C)}{{L_2}^2{\delta_1}^2C} & \frac{-Cr_C\delta_2 + 2L_2}{C^2{\delta_1}^2L_2} & \frac{C{\delta_2}^2 + 2L_2}{C^2{\delta_1}^2L_2} \\ -\frac{r_{L1}\delta_2}{L_1C\delta_1} & \frac{Cr_C(r_{L2}\delta_1 + r_C\delta_2) + L_2(\delta_2 - r_C)}{C^2{\delta_1}^2L_2} & \frac{Cr_C{}^2 + 2L_2}{C^2{\delta_1}^2L_2} & \frac{-\delta_2Cr_C + 2L_2}{C^2{\delta_1}^2L_2} \end{bmatrix}$$

On the bases of this example it can be conclude that, in the ideal or real case, the condition (107) is not satisfied.

5.3. Hybrid Modeling

Many dynamical systems combine typical behaviors of continuous time dynamical systems and discrete time dynamical systems. For instance, in a switching converter, currents and voltages change continuously, in according to the Kirchhoff laws, and discontinuously due to the opening and closing of the switching device. This last behavior leads to a rich dynamical system called hybrid model.

In a hybrid model the continuous time dynamics is taken into account by mean the widely used model with state constraints:

$$\dot{\boldsymbol{x}} = f(\boldsymbol{x}) \tag{111}$$

where $\dot{\boldsymbol{x}}$ belonging to a set-valued mapping $F(\boldsymbol{x})$ and $\boldsymbol{x}$ belonging to $\mathcal{C}$, a subset of the n-dimensional Euclidean space $\Re^n$. The dimension of set $\mathcal{C}$ depends on the constraints of the systems and the physical initial conditions.

In a hybrid system, the discrete time dynamics instead, is taken into account by means the typical first order equation:

$$\boldsymbol{x}^+ = g(x) \tag{112}$$

The notation $\boldsymbol{x}^+$ indicates that the next value of the state is given as function of the current state $\boldsymbol{x}$ through the value of $g(\boldsymbol{x})$. As for differential equations, in this case we can write instead that $\boldsymbol{x}^+ \in \mathcal{G}(\boldsymbol{x})$, a set-valued mapping, and $\boldsymbol{x} \in \mathcal{D}$ a subset of $\Re^n$. In compact form the general hybrid model with constraints is given by (Goebel et al. 2009):

$$\dot{\boldsymbol{x}} \in F(\boldsymbol{x}), \qquad \boldsymbol{x} \in \mathcal{C} \tag{113}$$

$$\boldsymbol{x}^+ \in \mathcal{G}(\boldsymbol{x}), \qquad \boldsymbol{x} \in \mathcal{D} \tag{114}$$

where (113) represents the constrained differential inclusion (continuous time model part) and (114) represents the constrained difference inclusion (discrete time model part). The model (113),(114) captures a wide variety of dynamic phenomena including systems with logic-based state components.

We refer to a hybrid system in the form (113),(114) as $\mathcal{H}$ and, also we call F the flow map, $\mathcal{C}$ the flow set; $\mathcal{G}$ the jump map and finally $\mathcal{D}$ the jump set.

5.4. Hybrid Model of a switching converter

In order to modeling a switching converter as a hybrid system $\mathcal{H}$ the procedure step by step is proposed.

As it is well known in literature, a switching converter can works in CCM or in DCM if the current of the inductor drop to zero almost in a time instant during the *off time*. In CCM, any switching DC-DC converters can be described by the state space equations (73) and (74) while, if it works in DCM, another state space model is required. Therefore, in general, it is possible to describe the systems in every conduction mode by means a set of linear network as following:

$$\begin{cases} \begin{cases} \dot{\boldsymbol{x}} = f_{ON}(\boldsymbol{x}, u) \\ y = h_{ON}(\boldsymbol{x}) \end{cases} \\ \begin{cases} \dot{\boldsymbol{x}} = f_{OFF}(\boldsymbol{x}, u) \\ y = h_{OFF}(\boldsymbol{x}) \end{cases} \\ \begin{cases} \dot{\boldsymbol{x}} = f_{DCM}(\boldsymbol{x}, u) \\ y = h_{DCM}(\boldsymbol{x}) \end{cases} \end{cases} \tag{115}$$

where $\boldsymbol{x}$ is the state vector belonging to $\Re^n$ where n is the order of the system, and finally u is the input source. In (115) the couple of functions f_{ON} and h_{ON}, f_{OFF} and h_{OFF}, f_{DCM} and h_{DCM} described the converter respectively in the *on mode*, *off mode* and *discontinuous mode*.

Defining a variable $\sigma = [1,2,3]$ where $\sigma = 1$ means *on mode*, $\sigma = 2$ means *off mode* and finally $\sigma = 3$ means *discontinuous mode* and moreover a time variable τ such that: $\dot{\sigma} = 0$ and $\dot{\tau} = 1$, it is possible extend the state vector $\boldsymbol{x}$ as following:

$$\tilde{\boldsymbol{x}} = \begin{bmatrix} \boldsymbol{x} \\ \tau \\ \sigma \end{bmatrix} \tag{116}$$

Using the extended state $\tilde{\boldsymbol{x}}$ is possible to specify the set of equations (113),(114):

$$\dot{\tilde{\boldsymbol{x}}} = \tilde{f}_{\sigma}(\tilde{\boldsymbol{x}}, \boldsymbol{u}) \tag{117}$$

$$y = \tilde{h}_{\sigma}(\tilde{\boldsymbol{x}}) \tag{118}$$

$$\tilde{\boldsymbol{x}}^{+} = \begin{bmatrix} \boldsymbol{x}^{-} \\ \tau = \tau^{-} \\ \sigma = 2 \end{bmatrix} \qquad \text{IF } \tilde{\boldsymbol{x}} \in [\Re^n] \times [T_{ON}, +\infty] \times [1] \tag{119}$$

$$\tilde{\boldsymbol{x}}^{+} = \begin{bmatrix} \boldsymbol{x}^{-} \\ \tau = 0 \\ \sigma = 1 \end{bmatrix} \qquad \text{IF } \tilde{\boldsymbol{x}} \in [\Re^{n}] \times [T_{sw}, +\infty] \times [\{1, 2\}] \tag{120}$$

$$\tilde{\boldsymbol{x}}^{+} = \begin{bmatrix} \boldsymbol{x}^{-} \\ \tau = \tau^{-} \\ \sigma = 3 \end{bmatrix} \qquad \text{IF } \tilde{\boldsymbol{x}} \in [0 \times \Re^{n-1}] \times [T_{ON}, T_{sw}] \times [2] \tag{121}$$

5.5. Hybrid Model of the Boost converter

In order to understand the potentiality of the Hybrid modeling, in this section there is a numerical example of the Boost converter.

The Hybrid model of the Boost converter is defined by the equations (117)-(121) in which $\tilde{\boldsymbol{x}} = [\boldsymbol{x}\ \tau\ \sigma\ ]^{T} = [x_1\ x_2\ \tau\ \sigma\ ]^{T} = [i_L\ v_C\ \tau\ \sigma\ ]^{T}$, $u = V_{IN}$ and:

$$\tilde{f}_1(\tilde{\boldsymbol{x}}, u) = \begin{bmatrix} -\frac{r_L}{L} x_1 + \frac{u}{L} \\ -\frac{1}{C(R + r_C)} x_2 \\ 1 \\ 0 \end{bmatrix} \tag{122}$$

$$\tilde{h}_1(\tilde{\boldsymbol{x}}) = \frac{R}{R + r_C} x_2 \tag{123}$$

$$\tilde{f}_2(\tilde{\boldsymbol{x}}, u) = \begin{bmatrix} -\frac{r_C r_L + R(r_L + r_C)}{L(R + r_C)} x_1 - \frac{R}{L(R + r_C)} x_2 + \frac{u}{L} \\ \frac{R}{C(R + r_C)} x_1 - \frac{1}{C(R + r_C)} x_2 \\ 1 \\ 0 \end{bmatrix} \tag{124}$$

$$\tilde{h}_2(\tilde{\boldsymbol{x}}) = \frac{R r_C}{R + r_C} x_1 + \frac{R}{R + r_C} x_2 \tag{125}$$

$$\tilde{f}_2(\tilde{\boldsymbol{x}}, u) = \begin{bmatrix} 0 \\ 1 \\ -\frac{1}{C(R + r_C)} x_2 \\ 1 \\ 0 \end{bmatrix} \tag{126}$$

$$\tilde{h}_3(\tilde{\boldsymbol{x}}) = \frac{R}{R + r_C} x_2 \tag{127}$$

The validation of the Hybrid model of the Boost converter has been performed in the Matlab-Simulink® environment.

In the validation processing, the reference model has been implemented using the PLECS® block-sets and, the parameters of the Boost converter sketched in Table 4. Moreover a comparison between the Hybrid model and the SSA model has been performed.

Table 4 Rated circuit parameter of a Boost converter for PFC application.

Symbol	Values	
V_{IN}	311	[V]
L	4	[mH]
r_L	0.5	[Ω]
C	3.3	[mF]
r_C	10	[mΩ]
f_{sw}	20	[KHz]
R	160	[Ω]
P_n	1	[KW]
D	22%	

In Figure 38 are sketched the time domain waveforms of the Boost models during a start-up transient. This kind of test is representative because it involves the two conduction modes: CCM and DCM. The response of the Boost described by means of Hybrid modeling approach is practically the same of the Plecs® reference model. Unlike the SSA model, the Hybrid model is able to describe the start-up transient very well both in terms of current and voltage. The management of the DCM case guarantees an inductor current always greater or equal to zero and a correct voltage response. The SSA model it is able to describe the average behavior of the system when the DCM is elapsed. Indeed, at steady-state (time > 0.25 s) the average voltage and current are the real ones. In the zoomed area of Figure 38, it is possible observe that the Hybrid model contains the typical switching trend of the inductor current whereas the SSA model its average value in a switching period.

For the same start-up transient of Figure 38, in Figure 39 is shown the vector state $\tilde{\boldsymbol{x}}$ of the Boost Hybrid-model. More exactly, it is possible observe the time domain trends of the input current, the capacitor voltage, the time-state τ and, finally, the mode-state σ. In the middle picture, the mode-state σ describes the evolution of the converter operating modes: CCM, DCM, and CCM. The first transition from CCM to DCM is better showed in the bottom picture of Figure 39. In this last zoomed transition (time window of 1ms), it is possible to observe the effects of the jump-map (equations from (119) to (121)) in the states x_1, x_3 and x_4. The time-state is a

sawtooth with amplitude T_{sw}. The mode-state changes its value in accordance to the inductor current value and the time-state value. Indeed its values is one for time $t \in [0, DT_{sw}]$, two for time $t \in [DT_{sw}, T_{sw}\,] \wedge x_1 \in (0, +\infty)$, three for time $t \in [DT_{sw}, T_{sw}\,] \wedge (x_1 = 0)$.

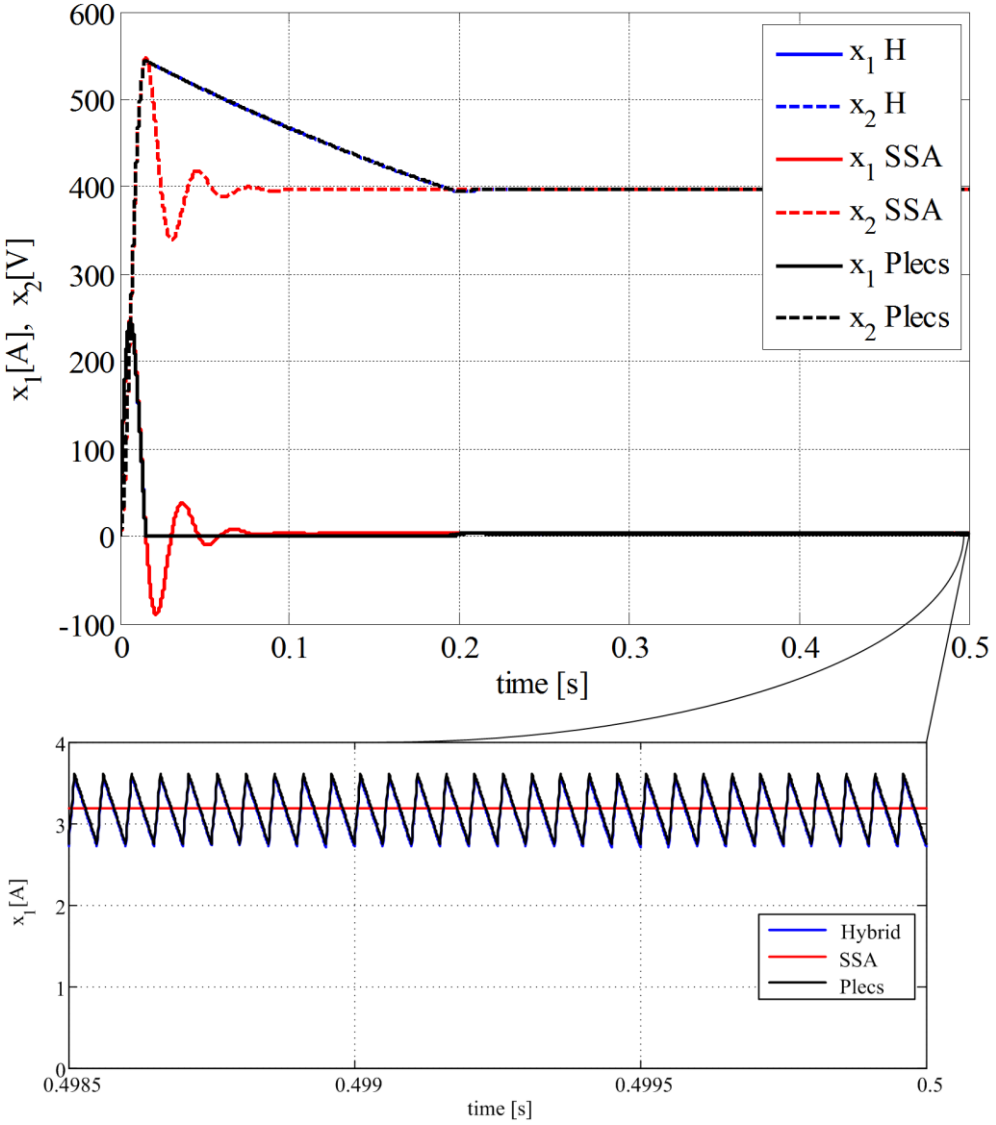

Figure 38 Comparison between the Hybrid model and the SSA model during a start-up transient: inductor currents, capacitor voltages.

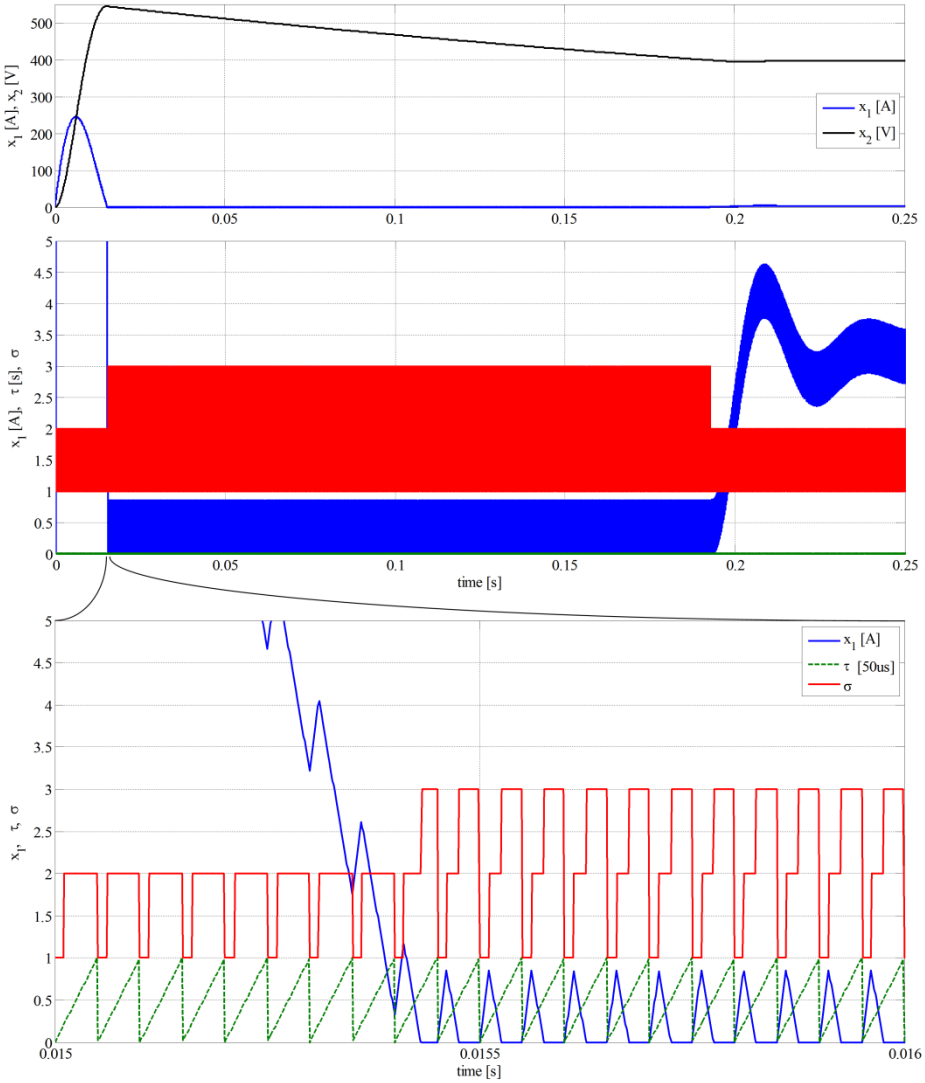

Figure 39 State vector of the Hybrid model during a start-up transient: inductor current, capacitor voltage, time-state variable, mode-state variable.

5.6. Conclusion

In the first part of the chapter, the limits of the SSA modeling have been highlighted. The conclusion of the state evolution analysis is that the free evolution of the averaged model effectively represents the free evolution of the converter if and only if the product of the two dynamic matrices is commutative. Indeed, in the ideal or real case, the commutative property of the two dynamic matrices is not satisfied in the *QBC1* converter but also in the easiest step-up converter, the traditional Boost converter. The first order approximation of the forced state evolution for the averaged model coincides with that one of the real system if the commutative

property of the matrices is satisfied and the switching frequency is as smaller as possible. All in all, the SSA model represents a good approximated averaged model of the converter if it works only in CCM.

The limits of the SSA modeling have been exceeded using the Hybrid modeling theory. With this formalism it is possible to obtain a general mathematical description of a switching converter. The Hybrid system theory has been applied to a traditional Boost converter successfully. The Hybrid model of the Boost converter is able to describe the continuous and discrete dynamics of the system in CCM or DCM without any constraint.

Chapter 6

Sensitivity analysis versus parameters variation

6.1. Introduction

In this section a sensitivity analysis versus parameters variation of the Boost converter, the *QBC1* and the *QBC2* has been treated. In general, for a DC/DC converter, a negligible variation of the static gain with the duty cycle and with the parasitic input inductor resistance is desirable. This condition makes the control task easier to maintain the output voltage regulated during the operation.

Defining N_L and N_C respectively the number of the inductors and the capacitors of the power stage, and also r_{L_i} and r_{C_j} the parasitic elements of the generic DC/DC converter with i=1, … , N_L and j=1, … , N_C. The static gain sensitivity versus the variations of the parasitic elements r_{L_i} and r_{C_j} is given by:

$$\Delta M = \left|\frac{\partial M}{\partial D}\right| \Delta D + \sum_{i=1}^{N_L} \left|\frac{\partial M}{\partial r_{L_i}}\right| \Delta r_{L_i} + \sum_{j=1}^{N_C} \left|\frac{\partial M}{\partial r_{C_j}}\right| \Delta r_{C_j} \tag{128}$$

6.2. Sensitivity analysis of the Boost Converter

Using the expression of the static gain of the Boost converter, (16), and the equation (128) the sensitivity terms are equal to:

$$\frac{\partial M}{\partial D} = \frac{1 - \frac{r_L}{R(1-D)^2}}{\psi(D)} \tag{129}$$

$$\frac{\partial M}{\partial r_L} = \frac{-1}{\psi(D) R(1-D)} \tag{130}$$

with $\psi(D) = (1-D)^2 \left[1 + \frac{r_L}{R(1-D)^2}\right]^2$.

It should be noted that the higher r_L, the lower is the sensitivity. This result is in the opposite direction compared to the static gain curve. In other words an inductor with small parasitic resistance will require a more accurate control algorithm especially for high values of the duty cycle.

The sensitivity term respect the parasitic resistance of the capacitor is negligible because $r_C \ll R$ and its effect in the static gain is meaningless.

Table 5 Rated circuit parameter of the Boost converter.

Symbol	Description	Values	
V_{IN}	Input voltage	30	[V]
L	Input inductance	1.48	[mH]
r_L	Parasitic resistance of L	40	[mΩ]
C	Output capacitances	100	[uF]
r_C	Parasitic resistance of C	318	[mΩ]
f_{sw}	Switching frequency	20	[KHz]
R	Load	175	[Ω]
r_{ON}	Forward resistance of IGBT	100	[mΩ]
P_n	Rated Power	300	[W]

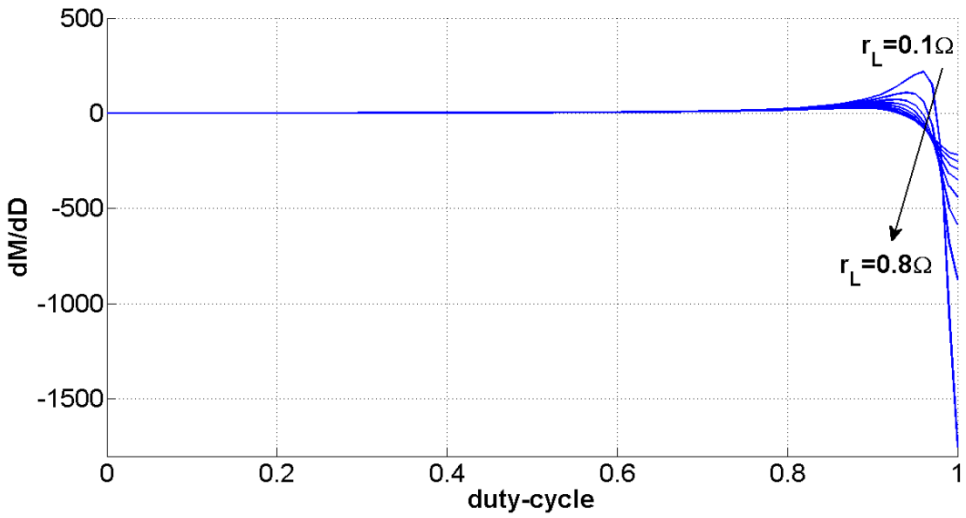

Figure 40 Gain derivative respect to the duty-cycle for different values of the parasitic input inductor resistance.

Using the rated parameter of Table 5 it is possible to plot the numerical trend of equations (129) and (130). The sensitivity curves are given in Figure 40 and Figure 41. All figures exhibit a very small value up to a duty cycle equal to 0.8. It implies a relatively easy control of the converter. It should be borne in mind however that a very low value of the parasitic resistance would permit to work with high boost ratio but in this case the derivatives present higher variations.

These informations are summarized in the 3-dimensional plot of Figure 41 where it is more evident that when the load is far from the rated value for high boosting, the sensitivity is raised.

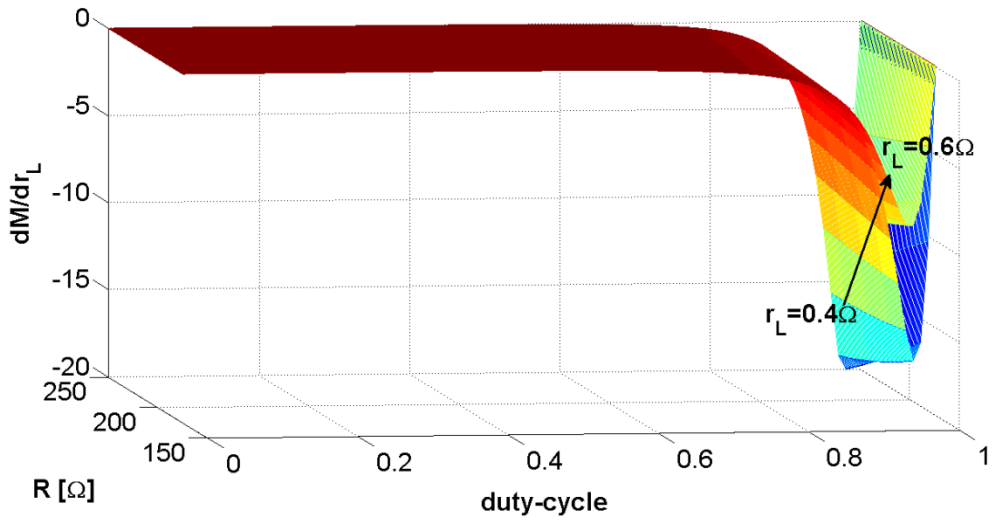

Figure 41 3D-plot of the gain derivative respect to the parasitic input inductor resistance versus duty-cycle and load values.

6.3. Sensitivity analysis of the QBC1 Converter

In the *QBC1* converter, the sensitivity terms are given by:

$$\frac{\partial M}{\partial D} = \frac{2\left(1 - \frac{r_{L1}}{R(1-D)^4} - \frac{2}{(1-D)^4}\right)}{\psi'(D)(1-D)^3} \tag{131}$$

$$\frac{\partial M}{\partial r_{L1}} = \frac{-1}{\psi'(D)R(1-D)^6} \tag{132}$$

$$\frac{\partial M}{\partial r_{L2}} = \frac{-1}{\psi'(D)} \tag{133}$$

with $\psi'(D) = \left(1 + \frac{r_{L1}}{R(1-D)^4} + \frac{r_{L2}}{R(1-D)^2}\right)^2$.

Using the parameter table of the *QBC1*, Table 2, the curve of the static gain is obtained, it is shown in Figure 42. In the plot area the parasitic input resistance is used as variable parameter. The shape of the curves is similar to the ones obtained for the Boost converter. Anyway, the drop of the gain occurs for lower values of the duty-cycle. This would suggest a possible control of the converter up to a value of the duty-cycle near to about *0.7* (corresponding to a gain equal to about 8).

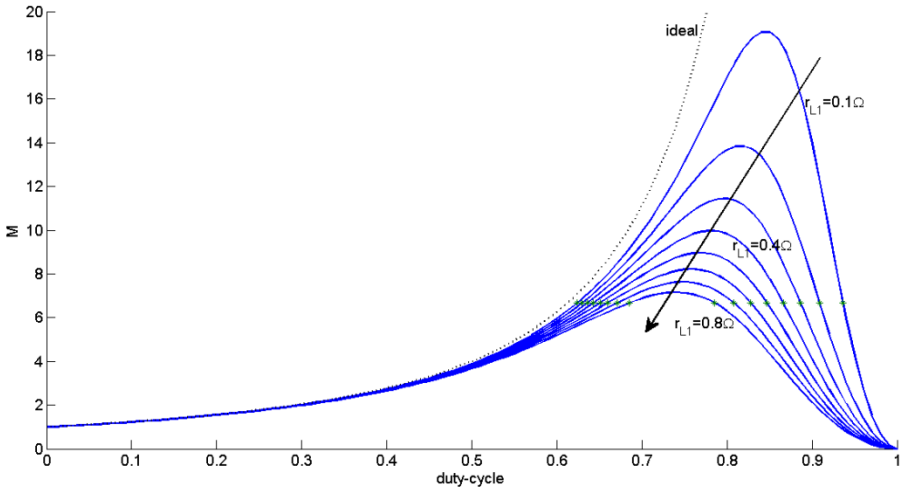

Figure 42 Static gain of the QBC1 versus duty-cycle.

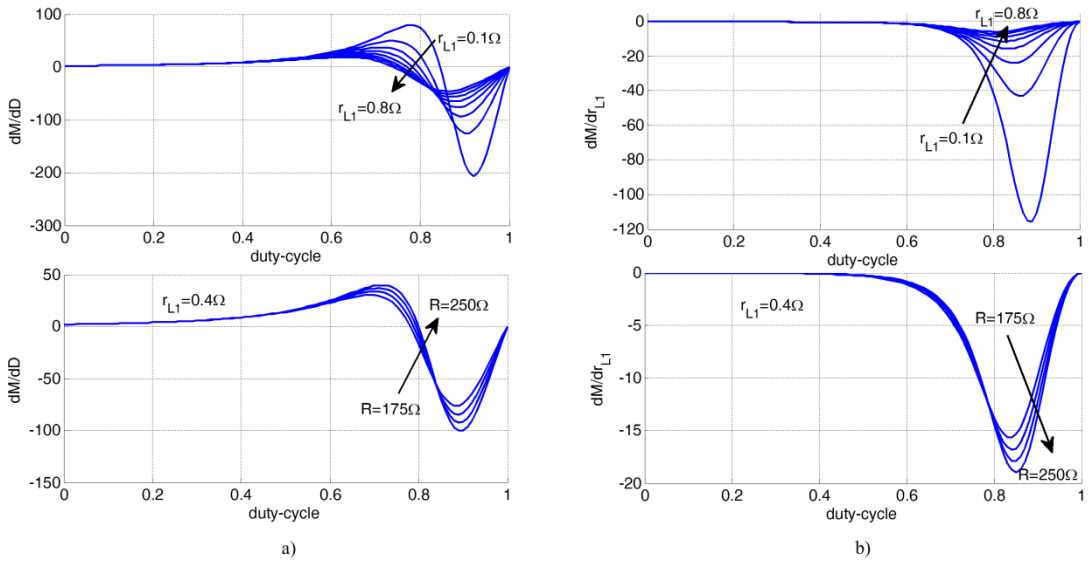

Figure 43 Sensitivity gain terms of the QBC1 versus duty-cycle: a) Gain derivative respect to the duty-cycle; b) Gain derivative respect to the parasitic input inductor resistance.

Figure 43 a) shows the derivative of the gain function versus the duty cycle adopting as parameter the parasitic resistance and the load resistance respectively.

The same considerations about the Boost remain valid, however, it is more evident that a low value of the parasitic resistance of the input inductor induces high variation starting from D=0.6. As the influence of the load value the operation in the neighborhood of the rated load is subjected to lower value of the sensitivity.

Finally, the derivative of the gain respect to the parasitic resistance confirms the consideration that a low parasitic resistance makes more difficult the control task, see Figure 43 b). In addition, since the parasitic resistance varies with the temperature during the operation, the control algorithm must be robust to face up with these variations.

6.4. Sensitivity analysis of the QBC2 Converter

In the *QBC2* converter, the sensitivity terms are given by:

$$\frac{\partial M}{\partial D} = \frac{2\left(1 - \frac{r_{L1}}{R(1-D)^4} - \frac{2}{(1-D)^4}\right)}{\psi''(D)(1-D)^3} \tag{134}$$

$$\frac{\partial M}{\partial r_{L1}} = \frac{\left(1 + \frac{r_{C1}}{R}\right)^2}{\psi''(D)R(1-D)^4} \tag{135}$$

$$\frac{\partial M}{\partial r_{L2}} = \frac{\left(1 + \frac{r_{C1}}{R}\right)^2}{\psi''(D)R} \tag{136}$$

$$\frac{\partial M}{\partial r_{C1}} = \frac{1 + \frac{r_{C1}}{R(1-D)} - \frac{1}{(1-D)}\left(1 + \frac{r_{C1}}{R}\right)}{\psi''(D)R(1-D)^2} \tag{137}$$

$$\frac{\partial M}{\partial r_{C2}} = \frac{D\left(1 + \frac{r_{C1}}{R}\right)^2}{\psi''(D)R(1-D)^5} \tag{138}$$

with $\psi''(D) = \left[1 + \frac{r_{C1}}{R(1-D)} + \left(1 + \frac{r_{C1}}{R}\right)\left(\frac{r_{L1}}{R(1-D)^4} + \frac{r_{L2}}{R(1-D)^2} + \frac{r_{C2}D}{R(1-D)^3}\right)\right]^2$.

Using the rated parameter of Table 6 it is possible to evaluate numerically the sensitivity terms of the *QBC2*.

In Figure 44, the static gain of the *QBC2* versus the duty-cycle and the parasitic parameters is plotted. Unlike the Boost and *QBC1*, the static gain of the *QBC2* essentially depends on the parasitic resistance of the first inductor and of the middle capacitor. For this reason $N_C = 2$ has been adopted in the sensitivity analysis. Finally, Figure 45 shows the input to output conversion ratio of the *QBC2* versus duty-cycle and load variations. In rated condition it is possible to obtain a conversion ratio equal to about 10 for *D=0.7*.

Table 6 Rated circuit parameter of the *QBC2*.

Symbol	Description	Values	
V_{IN}	Input voltage	30	[V]
L_1	First inductor	0.5	[mH]
r_{L1}	Parasitic resistance of L_1	20	[mΩ]
L_2	Second inductor	0.5	[mH]
r_{L1}	Parasitic resistance of L_2	20	[mΩ]
C_1	Output capacitance	99	[uF]
r_{C1}	Parasitic resistance of C_1	25	[mΩ]
C_2	Middle capacitance	16.5	[uF]
r_{C2}	Parasitic resistance of C_2	150	[mΩ]
f_{sw}	Switching frequency	20	[KHz]
R	Load	[48, 480]	[Ω]
r_{ON}	Forward resistance of SiC MOSFET	80	[mΩ]
P_n	Rated Power	300	[W]

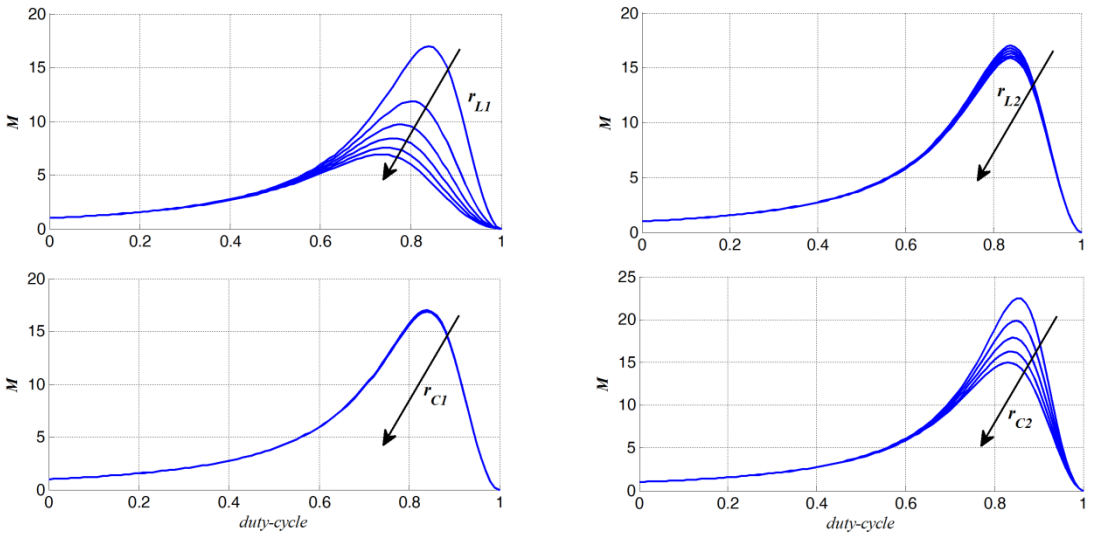

Figure 44 Static gain of the QBC2 versus duty-cycle.

Figure 46, Figure 47, and Figure 48 show the derivative of the gain function respect respectively to: the duty cycle, the parasitic resistance of the first inductor, the ESR of the middle capacitor. The same considerations about the Boost and the *QBC1* remain valid. Low value of the parasitic resistance of the first inductor induces high variation starting from D=0.6. Lower values of the sensitivity terms are obtained in rated load condition.

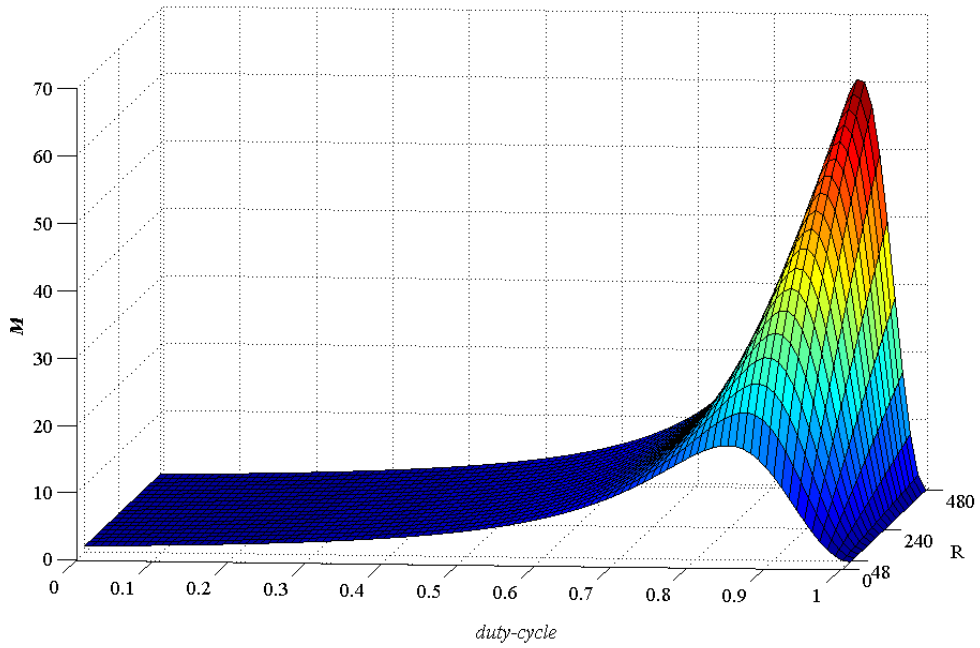

Figure 45 Static gain of the QBC2 versus duty-cycle and load variation.

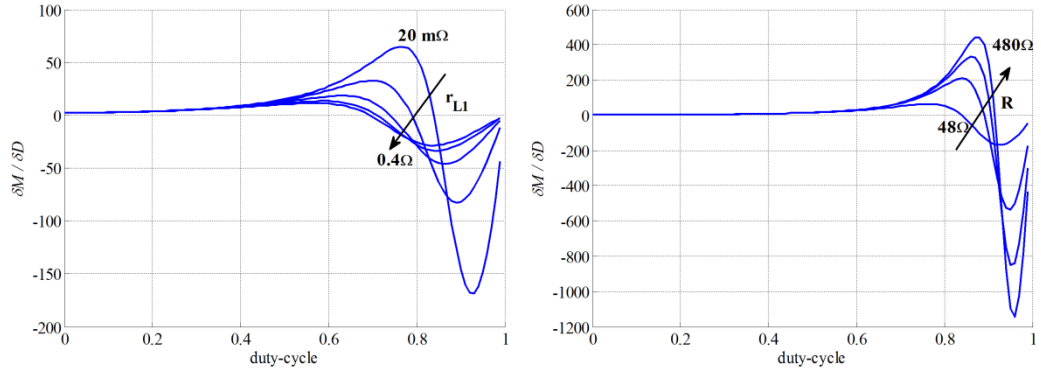

Figure 46 Gain derivative respect to the duty-cycle, *QBC2*.

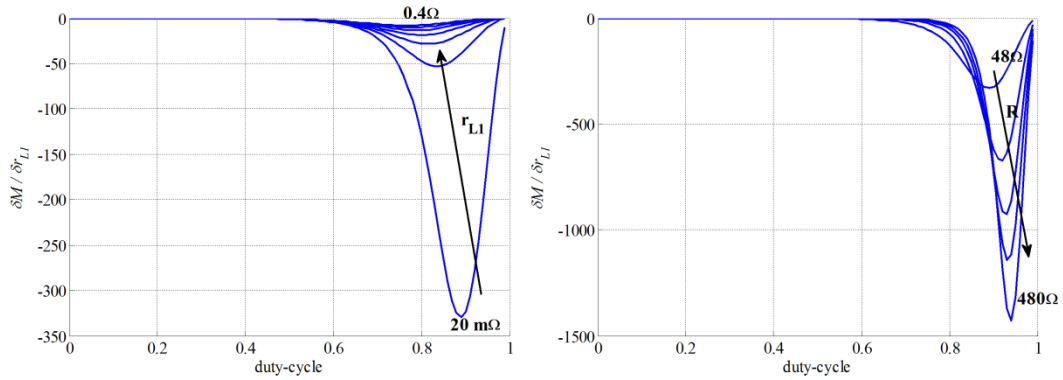

Figure 47 Gain derivative respect to the parasitic resistance of the first inductor, *QBC2*.

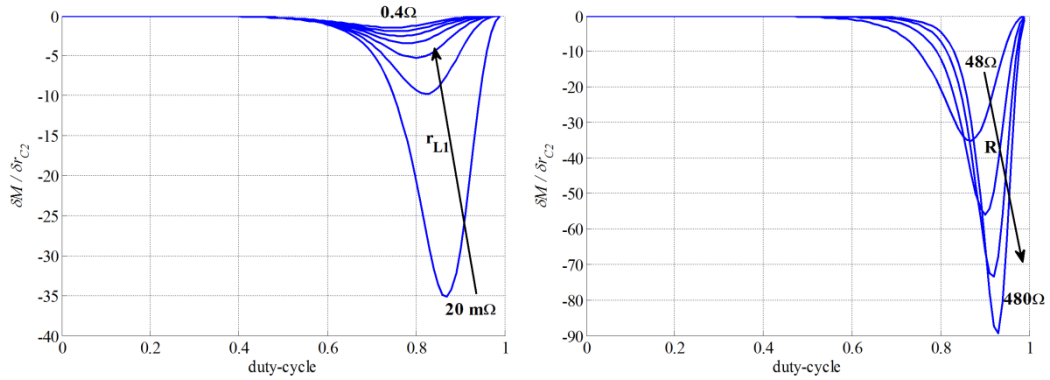

Figure 48 Gain derivative respect to the parasitic resistance of the middle capacitor, *QBC2*.

6.5. Conclusion

DC/DC Quadratic Boost Converters give advantages in terms of voltage boosting. The presence of an input inductance assures a low ripple of the input current. In order to increase the efficiency of these converters a low value of the parasitic resistance of the input inductance is desired. On the other hand, this dramatically increases the sensitivity of the static gain especially in the region of higher duty cycle, where the converter is required to be operated.

Chapter 7

Control of DC/DC Switching Converter

7.1. Introduction

The DC/DC converters are variable-structure systems with fast nonlinear dynamics that are potentially subject to switching noise. Such systems are challenging from the control perspective, therefore a large palette of control methods exists.

Typically, power electronic converters require a suitable controller for operating and safety goals. For instance, a DC/DC converter needs duty-cycle adjustments in order to ensure a constant output voltage for the entire operating range. Figure 49 shows a generic control structure for power electronic systems. The output of the controller is the control average value, the duty-cycle. The duty-cycle needs modulation to be applied to the driver of the power switch. To this purpose, various kinds of modulators can be used; the Pulse Width Modulation (PWM) is the most common used modulator. Anyway, the controller must guarantee the desired output even if there are system perturbations such as load and supply variations. Moreover, the controller includes variable limitations such as the maximum admissible current or the saturation of the duty-cycle in a subset of the interval $[0, 1]$ in order to avoid the operating after the knee point. All these limitations introduce nonlinearities that the controller has to handle for example using anti-windup schemes.

In the converter control design, the frequency domain of interest is placed well below the carrier frequency but, a high closed-loop bandwidth is desirable. In this context, the knowledge of the passive elements is useful for control purposes because parameter/model variations may reduce the stability margins to low levels. For this reason, sometimes the controller performance is sacrificed for the sake of robustness.

In order to improve the response performances, adaptive algorithms can be used to ensure optimal closed-loop behavior for different operating point, i.e. gain scheduling. The parameter/model uncertainty can be also treated using robust control techniques.

The converters with a boost skill display a non-minimum phase behavior and make more difficult the control task.

In the case of converters that have more than two states, not all the states are sensed for economic issues. In this case, in order to reduce the number of transducers, a partial state feedback with observers (state reconstruction) can be used.

In literature, there are several control structures employed for DC/DC switching converter control. The model-based control technique depends on the nature of the adopted model. Figure 50 shows the relation between model and kind of control law.

From the knowledge of the converter it is possible use a physical or identification approach. In the first case, the Hybrid model describes the switching behavior in CCM or DCM and a variable structure control is required. In the assumption that the converter works in CCM, the SSA model describe the average behavior in a switching period. Using the SSA model, advanced nonlinear controllers can be designed: stabilizing control and passivity-based control that use the Lyapunov stability theory, feedback-linearization control that cancel the original plant nonlinearity with a nonlinear feedback. Linearizing the SSA model around a well-defined operating point, linear controls based on the small-signal model can be designed. In the latter case, the linear part of the identified Hammerstein model can be used to tuning a linear control law.

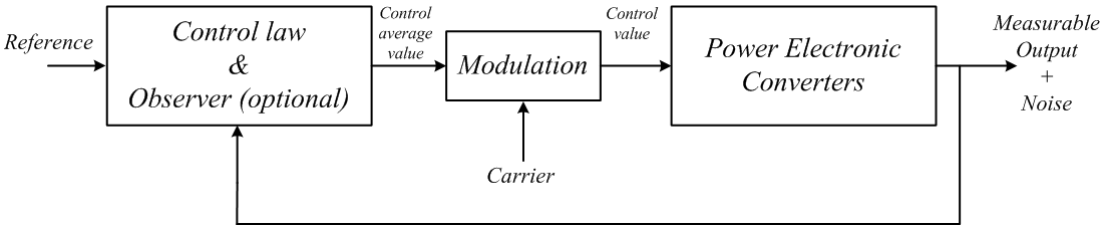

Figure 49 Generic control structure for power electronic converters.

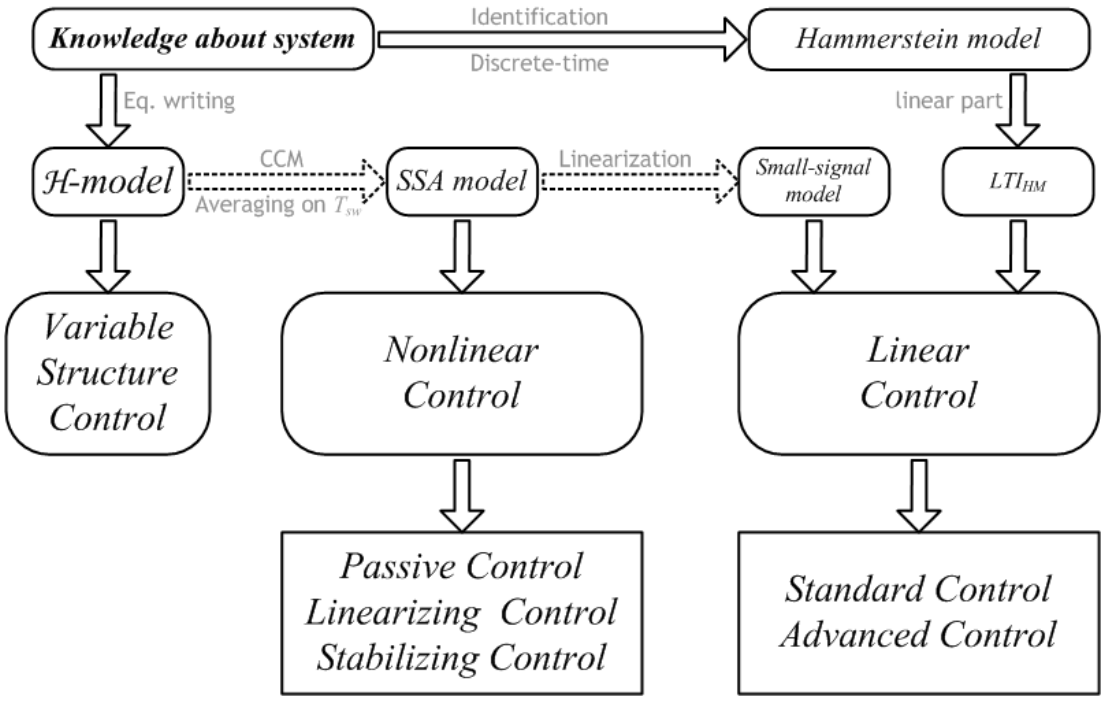

Figure 50 Relation between models and control laws.

7.2. Robust Control of the QBC1

The control of the *QBC1* converter can be carried out using robust control techniques in order to cope with model/parameter uncertainty. In particular, the control method in the frequency domain described in (Morari & Zafiriou 1990) is employed. This method has been applied to the small-signal and Hammerstein descriptions of the *QBC1*.

The voltage mode control of the *QBC1* can be carried out according to the scheme of Figure 51. More exactly, Figure 51 a) represents the control scheme based on the small-signal model, where $G_c(s)$ represents the controller transfer function, ${V_{pk}}^{-1}$ is the transfer function of the PWM modulator where V_{pk} is the peak value of the carrier waveform, and $G_{vo}(s)$ is the nominal transfer function of the converter. In this control scheme the voltage of the dc line and the load current variations are considered as system disturbances. In particular, $G_{v_o,v_{in}}(s)$ and Z_o are respectively the small-signal transfer function of v_o over v_{in} and v_o over i_{out}.

The VM control of *QBC1* converter by the Hammerstein model can be carried out according to the simple scheme of Figure 51 b), where $G_c(Z)$ is the discrete time

transfer function of the controller and $f^{-1}(\cdot)$ is the inverse of the function $f(\cdot)$. It can be observed that $f^{-1}(\cdot)$ is well defined in the duty-cycle range in which the function $f(\cdot)$ is strictly monotone, i.e. the usual range of operations. In Figure 51 b), the block *QBC* represents the model of the converter. To this regard, it is convenient to point out that in practical applications it could be necessary to change the load of the converter, whereas the line voltage V_{IN} could vary during the work. These events cannot be treated as parameter variations because the models are identified; instead, it is convenient to treat them as equivalent disturbance acting on the output of the model.

As already said, using the Hammerstein approach, few LTI models are needed to describe the converter in a large range of operation, together with the static nonlinear characteristics. All of these models have the same gain equal to 1, which means that the low frequency behavior is well defined. Instead, with reference to the description by means of small-signal model this is true only in a small range of duty-cycle.

This observation suggests to describe the linear part of the Hammerstein model and the small-signal model as an uncertain process consisting of a well-defined nominal model, and a set of transfer functions describing the uncertainty, $F_p(s)$. To this regard, it can be noted that the models describing the above uncertain system are discrete-time in the Hammerstein case. In order to use the same methodology for designing the controller starting from the Hammerstein and small-signal descriptions of the *QBC1*, these discrete-time models are transformed in continuous-time models using the bilinear transform. Then, robust control theory in the frequency domain for LTI models can be used for designing both the controllers.

Assuming $V_{pk} = 1$, and limiting the duty-cycle range to that in which $f(\cdot)$ is monotone, both controllers can be designed according to the equivalent scheme of Figure 52 a), putting $v_{ref} = 0$ when designing the controller for the SSA model. More precisely, both controllers are designed using the Internal Model Control (IMC) structure of Figure 52 b) where $\tilde{G}_p(s)$ is the nominal transfer function of the model, and $G_q(s)$ the transfer function of the IMC controller, whose link with $G_c(s)$ is given by:

$$G_c(s) = \frac{G_q(s)}{1 - G_q(s)\tilde{G}_p(s)} \tag{139}$$

The design of the controller $G_q(s)$ can be carried out using a multiplicative uncertainty description:

$$F_p = \left\{ G_p(s): \left| \frac{G_p(j\omega) - \tilde{G}_p(j\omega)}{\tilde{G}_p(j\omega)} \right| \leq \Delta_m(\omega) \right\} \tag{140}$$

where $\Delta_m(\omega)$ is the upper bound of the uncertainty due to parameters variations and unmodeled dynamics.

Let us define $\tilde{G}_p(s) = \tilde{G}_{pm}(s)\tilde{G}_{pa}(s)$ and $V(s) = V_m(s)V_a(s)$ where: $\tilde{G}_{pa}(s)$ is an all-pass transfer function containing the RHP (Right Half Plane) zeros of $\tilde{G}_p(s)$; $\tilde{G}_{pm}$ contains zeros and poles in the LHP (Left Half Plane); $V_m(s)$ is the part of the Laplace transform of the input (v_{ref} or ζ) containing zeros and poles in the LHP; $V_a(s)$ containing zeros and poles in the RHP of the input. The H_2 optimal controller, $\tilde{G}_q(j\omega)$, which minimizes a cost function J equal to $\|e(t)\|_2^2$ is given by:

$$\tilde{G}_q(s) = \left(\tilde{G}_{pm}(s)V_m(s)\right)^{-1} \left\{ \tilde{G}_{pa}{}^{-1}(s)V_m(s) \right\}_* \tag{141}$$

where: $e(t) = v_{ref}(t) - v_o(t)$ is the tracking error; the quantity $\{\cdot\}_*$ contains the terms of the partial fraction expansion of $\tilde{G}_{pa}{}^{-1}(s)V_m(s)$ relative to the LHP poles.

With reference to the input, it is usually assumed as the output of a LTI system having transfer function $W_{in}(s)$ supplied by either an ideal Dirac impulse, or a square integrable real signal, i.e. a signal with finite 2-norm. For example, a step input, $V(s) = \frac{1}{s}$, can be generated choosing $W_{in}(s) = \frac{1}{s}$ and an ideal Dirac impulse at its input. In this case, the type 1 H_2-optimal controller is given by:

$$\tilde{G}_q(s) = \tilde{G}_{pm}{}^{-1}(s) \tag{142}$$

It should be noted that $\tilde{G}_q(s)$ could not be physically realizable because the transfer function $\tilde{G}_{pm}^{-1}(s)$ could be an improper function. This problem is easily solved adding to the above optimal controller a cascade IMC filter. The IMC controller of the scheme of Figure 52 b) is given by:

$$G_q(s) = \tilde{G}_q(s)G_f(s) \tag{143}$$

where $G_f(s)$ is the transfer function of the IMC filter. In particular, $G_f(s)$ is a low pass filter that is inserted to meet the following conditions: make (143) physically realizable, preserving the conditions on the type of system, while ensuring the conditions for robust stability and/or robust behavior.

The simpler structure of the IMC filter, used in the following, is given by:

$$G_f(s) = \frac{\beta_{m-1}s^{m-1} + \cdots + \beta_1 s + \beta_0}{(1+s\lambda)^n} \tag{144}$$

where the coefficients β_i are chosen so as to satisfy the condition on the type, n to make the transfer function of the IMC controller physically realizable, whereas λ is chosen in order to satisfy the condition of robustness of stability or behavior, given by:

$$\sup_{\omega} \left|\tilde{C}(j\omega)\Delta_m(\omega)\right| < 1 \qquad \text{for robust stability} \tag{145}$$

$$\sup_{\omega} \left(\left|\tilde{C}(j\omega)\Delta_m(\omega)\right| + \left|\tilde{S}(j\omega)\mathrm{W}_{in}(\omega)\right|\right) < 1 \qquad \text{for behavior stability} \tag{146}$$

where $\tilde{S}(j\omega) = \left(1 - G_q(j\omega)\tilde{G}_p(j\omega)\right)$ and $\tilde{C}(j\omega) = G_q(j\omega)G_p(j\omega)$ are respectively the nominal sensitivity and the complementary sensitivity functions.

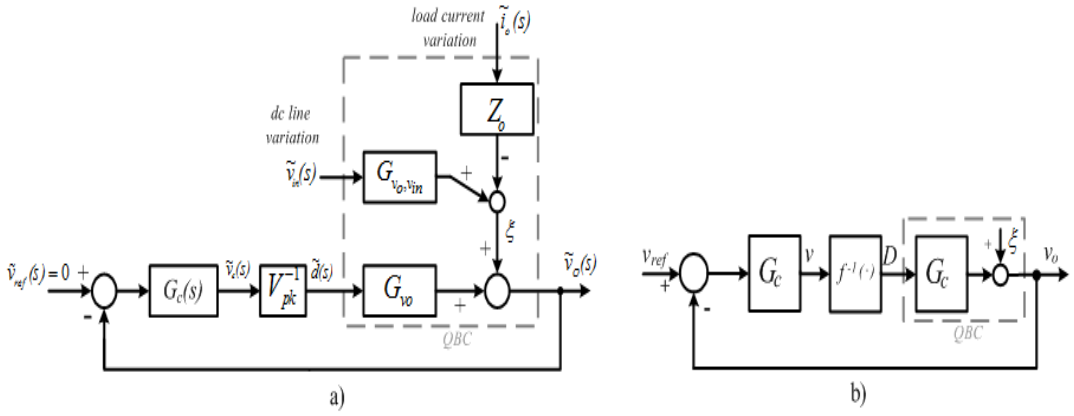

Figure 51 Voltage mode control scheme: a) small-signal model; b) Hammerstein model.

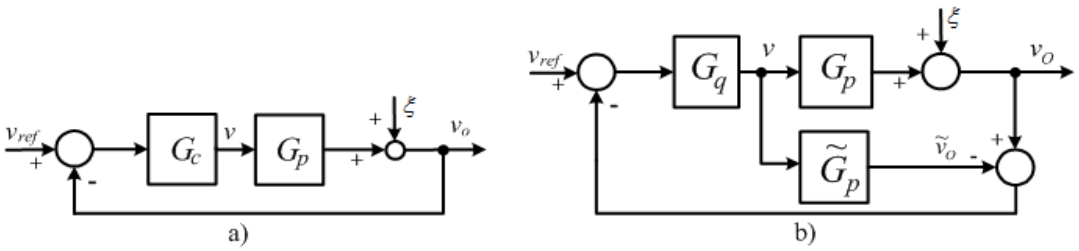

Figure 52 Voltage mode control scheme: a) equivalent control scheme; b) IMC control scheme.

7.2.1. Robust QBC1 Control based on the small-signal model

The control scheme of the *QBC1* based on the small-signal model is depicted in Figure 52 b) with $v_{ref} = 0$, and the input is the disturbance ζ. The chosen nominal model is that corresponding to D=0.65 between the set of transfer functions showed in Table 7. The uncertainty bound $\Delta_m(\omega)$, obtained considering the transfer functions $G_p(s)$ relative to D={0.6, 0.61, 0.62, 0.63, 0.64, 0.65}, is sketched in Figure 53.

The H_2-optimal, type 1 controller, obtained minimizing the cost function J, assumes the following form:

$$G_c(s) = \frac{K(s-z_1)(s-z_2)(s-z_3)(s-z_4)}{s(s-p_1)(s-p_2)(s-p_3)(s-p_4)} \tag{147}$$

where $p_1 = -1392$, $p_2 = -3.14 \cdot 10^4$, $p_3 = -3.79 \cdot 10^4$, $p_4 = -8.282 \cdot 10^4$, $K = 67.3386$, $z_{1,2} = (-2.5 \pm j3.58) \cdot 10^2$ and, $z_{3,4} = (-3.17 \pm j19.43) \cdot 10^2$.

Table 7 Continuous transfer functions of the *QBC1* small-signal model around several operating point.

Duty-Cycle	Transfer Function $G_{vo}(s)$
0.30	$\frac{-0.53\,s^4 - 6438\,s^3 + 3.25\cdot10^8 s^2 + 1.632\cdot10^{11}\,s + 1.598\cdot10^8}{s^4 + 1192\,s^3 + 7.1\cdot10^6\,s^2 + 4.155\cdot10^9\,s + 9.74\cdot10^{12}}$
0.35	$\frac{-0.6789\,s^4 - 1.189\cdot10^4\,s^3 + 3\cdot10^8 s^2 + 1.334\cdot10^{11}\,s + 1.469\cdot10^{15}}{s^4 + 1181\,s^3 + 6.439\cdot10^6\,s^2 + 3.71\cdot10^9\,s + 7.287\cdot10^{12}}$
0.40	$\frac{-0.8865\,s^4 - 1.952\cdot10^4\,s^3 + 2.643\cdot10^8 s^2 + 9.5\cdot10^{10}\,s + 1.336\cdot10^{15}}{s^4 + 1170\,s^3 + 5.864\cdot10^6\,s^2 + 3.316\cdot10^9\,s + 5.338\cdot10^{12}}$
0.45	$\frac{-1.183\,s^4 - 3.043\cdot10^4\,s^3 + 2.135\cdot10^8 s^2 + 4.5\cdot10^{10}\,s + 1.198\cdot10^{15}}{s^4 + 1159\,s^3 + 5.381\cdot10^6\,s^2 + 2.972\cdot10^9\,s + 3.817\cdot10^{12}}$
0.50	$\frac{-1.62\,s^4 - 4.641\cdot10^4\,s^3 + 1.406\cdot10^8 s^2 - 2.215\cdot10^{10}\,s + 1.055\cdot10^{15}}{s^4 + 1149\,s^3 + 4.99\cdot10^6\,s^2 + 2.675\cdot10^9\,s + 2.656\cdot10^{12}}$
0.55	$\frac{-2.281\,s^4 - 7.045\cdot10^4\,s^3 + 3.537\cdot10^7 s^2 - 1.143\cdot10^{11}\,s + 9.018\cdot10^{14}}{s^4 + 1138\,s^3 + 4.691\cdot10^6\,s^2 + 2.425\cdot10^9\,s + 1.792\cdot10^{12}}$
0.60	$\frac{-3.31\,s^4 - 1.075\cdot10^5\,s^3 - 1.174\cdot10^8 s^2 - 2.431\cdot10^{11}\,s + 7.355\cdot10^{14}}{s^4 + 1127\,s^3 + 4.485\cdot10^6\,s^2 + 2.22\cdot10^9\,s + 1.17\cdot10^{12}}$
0.65	$\frac{-4.95\,s^4 - 1.66\cdot10^5\,s^3 - 3.38\cdot10^8 s^2 - 4.241\cdot10^{11}\,s + 5.505\cdot10^{14}}{s^4 + 1117\,s^3 + 4.37\cdot10^6\,s^2 + 2.056\cdot10^9\,s + 7.387\cdot10^{11}}$

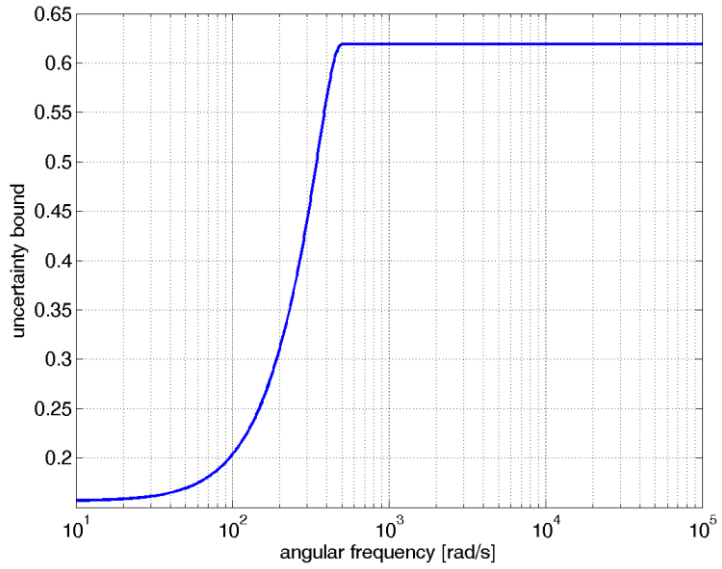

Figure 53 Multiplicative uncertainty bound of the *QBC1* using small-signal modeling.

7.2.2. Robust QBC1 Control based on the Hammerstein model

Using the Hammerstein approach, the chosen nominal model is that corresponding to the duty cycle range [0.60, 0.65]. The F_p family is composed by means of the transfer functions of Table 3 translated in the *s*-plane using the bilinear transformation. The nominal transfer function is sketched in Figure 54 together with the small-signal models in the same range. The numerical uncertainty bound is show in Figure 55. In this case, the uncertainty is greater than *1* for angular frequency greater than about *200 rad/s*.

The H_2-optimal, type 1 controller, assumes the form (147) where: $p_1 = -1.628 \cdot 10^3$, $p_2 = -1.25 \cdot 10^4$, $p_3 = -3.79 \cdot 10^4$, $p_4 = -8.282 \cdot 10^4$, $K = 88.153 \cdot 10^3$, $z_1 = -8.964 \cdot 10^{-3}$, $z_2 = -8.978 \cdot 10^4$ and, $z_{3,4} = (-1.95 \pm j3.65) \cdot 10^2$.

Comparing Figure 53 and Figure 55 a different profile of the uncertainty curve can be noted. In particular, the uncertainty curve in the SSA case exhibits lower values than the corresponding curve of the Hammerstein case. This can be explained taking into account that for the SSA approach the F_p family is defined in a neighbourhood of the operating point whereas in the Hammerstein case the uncertainty can be defined in a wider interval since the gain is unitary. For this reason, the set of F_p

family defined for the SSA is a subset of the F_p family defined in the Hammerstein approach.

In Figure 56 the Bode diagrams of the nominal open loop transfer functions are shown, corresponding to SSA and Hammerstein cases. It can be seen that the shape of the magnitude in both cases is almost coincident. In both cases, the stability margins, are positive, but robustness is here treated in the contest of the robust control theory.

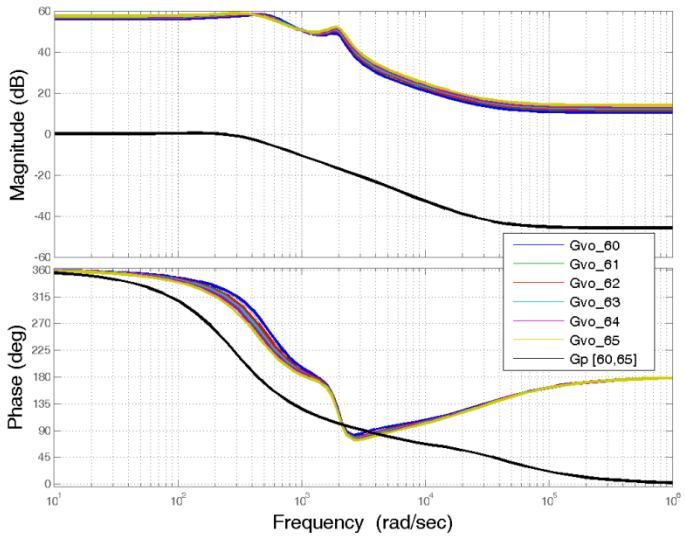

Figure 54 Bode diagrams of F_p family in the SSA case and nominal transfer function in the Hammerstein case.

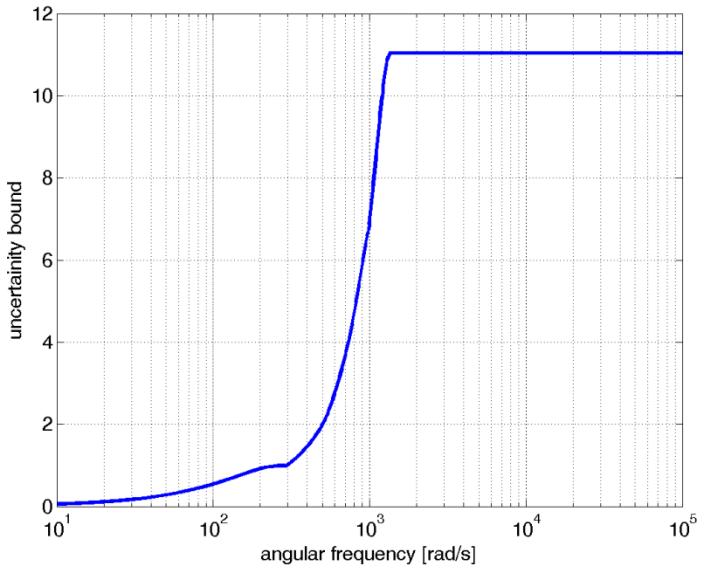

Figure 55 Multiplicative uncertainty bound of the *QBC1* in Hammerstein case.

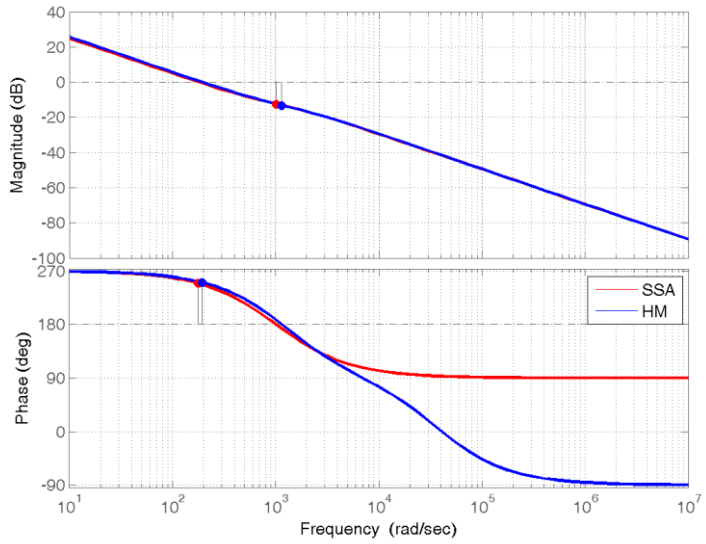

Figure 56 Bode diagrams of the open loop transfer function in SSA and Hammerstein cases (G_cG_{vo} and G_cG_p respectively).

7.2.3. Experimental Results: Robust Controller Comparison

Both the proposed robust controllers have been tested, by means of simulation and experimentally, on a suitable developed converter prototype, based on a 30A-600V fast IGBT STGW20NC60VD power device. The control algorithm, as well as the PWM algorithm, have been implemented on the DSPACE DS1103 board, adopting a sampling frequency of 20 kHz equal to the switching frequency of the converter. The converter is loaded by an electronic load Sorensen SLHACDC-500V, 6A. A picture of the test benchmark is shown in Figure 57.

In order to compare the robust control based on the small-signal model and on the Hammerstein model, two set of tests have been performed.

The first set of tests aims to show the behavior of the converter when a step variation of the reference voltage is imposed. In particular, Figure 58 shows the duty-cycle vs. time for a step variation of the reference voltage with the following values 30 V, 50 V, 70 V, 90 V, 110 V, 130 V and 150 V; the load is equal to 175 Ω and the input inductance is equal to 1.48 mH. The input current and the output voltage, under the same test conditions, are shown in Figure 59 and Figure 60 respectively. It can be noted that in all cases the behavior is the same when the reference voltage approaches the rated value. On the contrary, for test conditions far from this value, the behavior belonging to the SSA approach shows a higher tracking error compared

to behavior obtained with the control designed on the basis of the Hammerstein model. From another point of view, this better behavior of the robust controller obtained in the Hammerstein model case can be explained considering that the robust controller designed on the Hammerstein model contains a variable nonlinear gain (cf. Figure 32) which increase the dynamics of the system for low values of the duty cycle with respect to the SSA case.

The results of the second set of test are presented in Figure 61 and Figure 62, which show the duty-cycle and the output voltage vs. time for a ramp variations of the reference voltage from 30 V to 150 V using different slope of the ramp: 130, 260, 520 and 1040 [V/s]; the load is equal to 175 Ω and the input inductance is equal to 1.48 mH. The obtained curves confirm the result obtained with the former test where the tracking error between the reference voltage and the obtained one is as much lower as the reference voltage is close to the rated value.

This result is coherent with the previous test and can be explained considering that, the robust control designed on the basis of the Hammerstein model takes into account the static gain and presents a varying gain of the controller in the different working regions. This clearly accounts for a better tracking behavior in the ramp test, whereas the control system has been designed as a type 1 system. This result is also confirmed by the trend of the tracking error shown in Figure 63.

Finally Figure 64 and Figure 65 aim to verify the influence of the designed control on the output impedance; a variation of the output current from 0.8 A to 0.4 A and from 0.4 A to 0.8 A has been imposed maintaining the resistor load constant and equal to 1 kΩ. In both cases a slight improvement is noted in the case of robust control designed on the basis of the Hammerstein model. It should be however noticed that this improvement is not particularly significant.

The tests discussed were repeated by changing the input inductance, L_1=2 mH and r_{L1}=125 mΩ. The results are not shown here because the signal trends are the same.

Results show a very similar behavior of the two controllers as far as the working point is close to the nominal one (on which the controller is designed), whereas when the working point becomes far from the nominal one, the HM based robust controller exhibits better dynamic performance than the SSA one, due to its variable gain intrinsic characteristic.

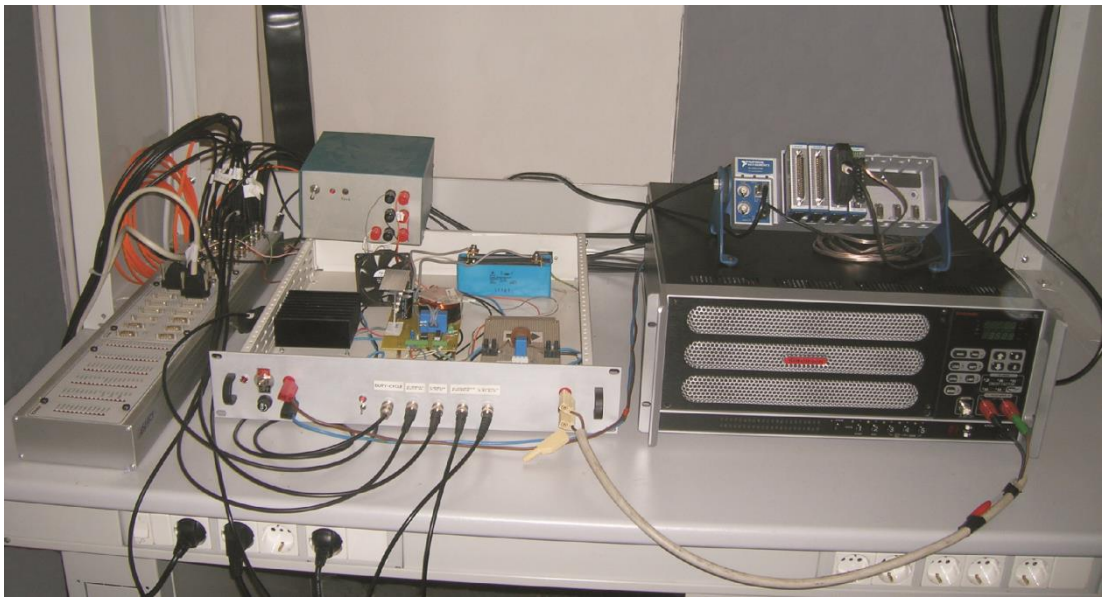

Figure 57 Test benchmark of the *QBC1*.

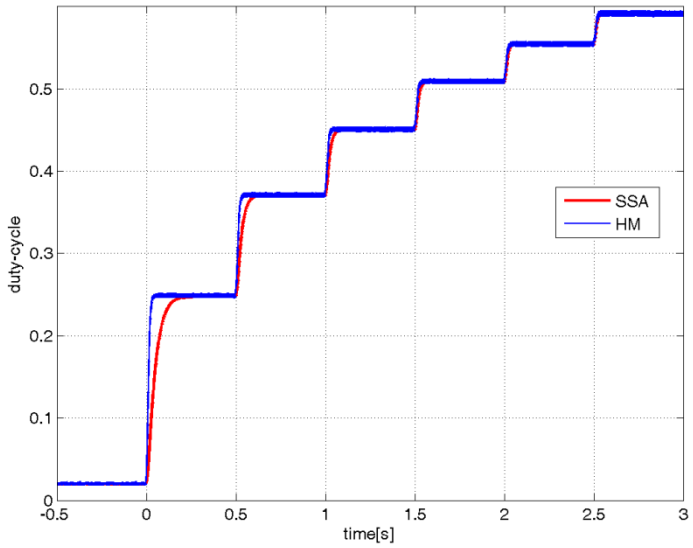

Figure 58 Duty-cycle vs. time for step variations of the reference voltage: 30 V, 50 V, 70 V, 90 V, 110 V, 130 V and 150 V; the load is equal to 175Ω; the input inductance is equal to 1.48 mH.

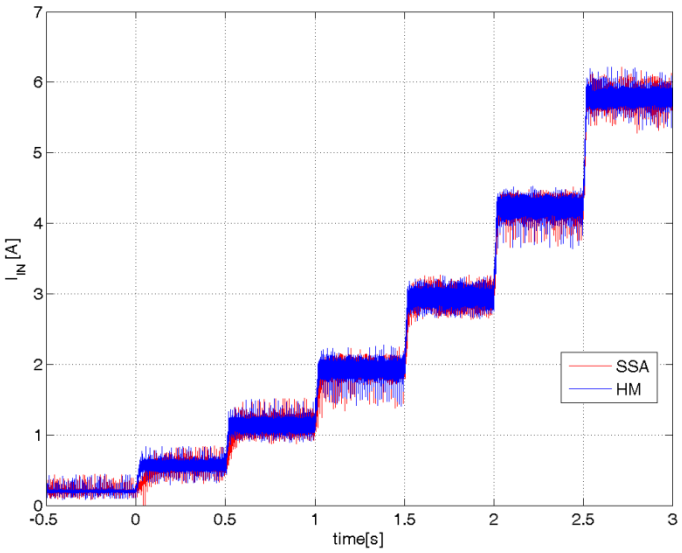

Figure 59 Input current vs. time for step variations of the reference voltage: 30 V, 50 V, 70 V, 90 V, 110 V, 130 V and 150 V; the load is equal to 175Ω; the input inductance is equal to 1.48 mH.

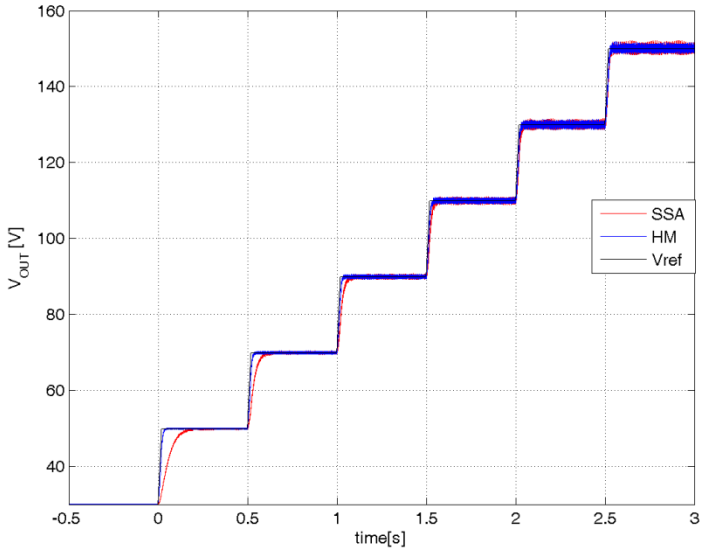

Figure 60 Output voltage vs. time for step variations of the reference voltage: 30 V, 50V, 70 V, 90 V, 110 V, 130 V and 150 V; the load is equal to 175Ω; the input inductance is equal to 1.48 mH.

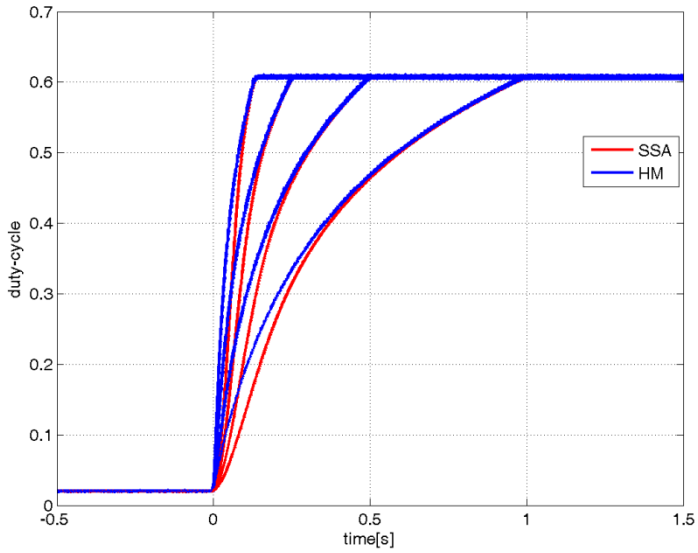

Figure 61 Duty-cycle vs. time for ramp variations of the reference voltage from 30 V to 150 V using different slope of the ramp: 130, 260, 520 and 1040 V/s; the load is equal to 175Ω; the input inductance is equal to 1.48 mH.

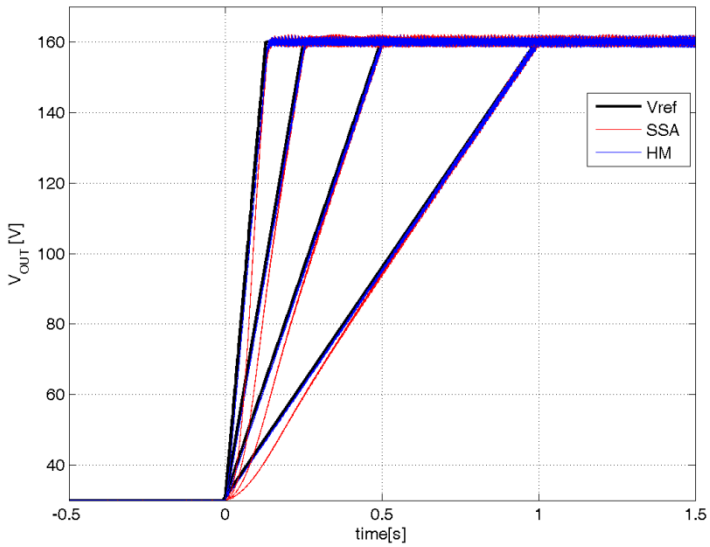

Figure 62 Output voltage vs. time for ramp variations of the reference voltage from 30 V to 150 V using different slope of the ramp: 130, 260, 520 and 1040 V/s; the load is equal to 175Ω; the input inductance is equal to 1.48 mH.

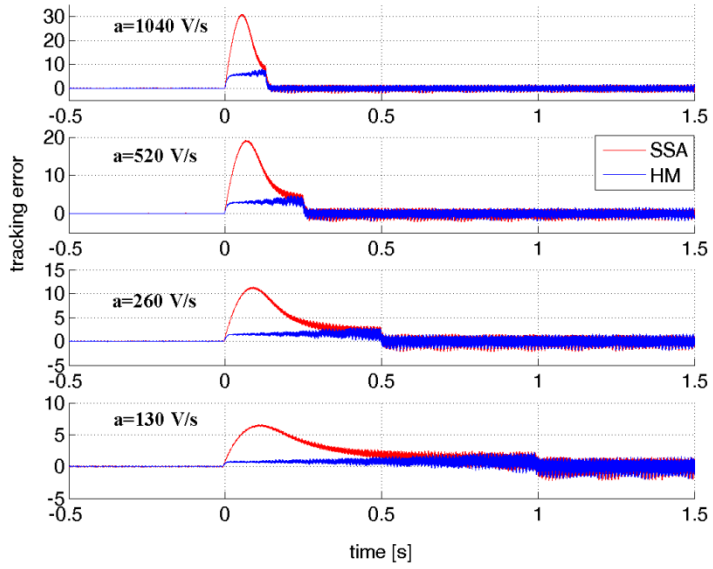

Figure 63 Tracking error vs. time for ramp variations of the reference voltage from 30 V to 150 V using different slope of the ramp: 130, 260, 520 and 1040 V/s; the load is equal to 175Ω; the input inductance is equal to 1.48 mH.

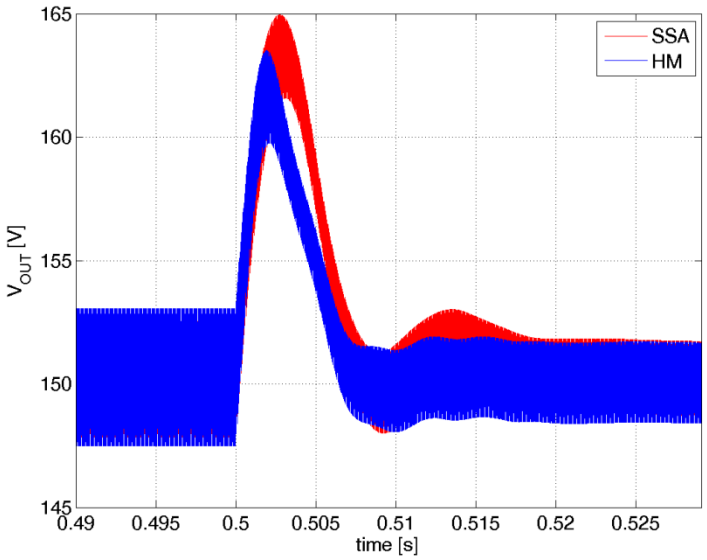

Figure 64 Output voltage for a step output current variation from 800 to 400 mA and a load resistance of 1kΩ.

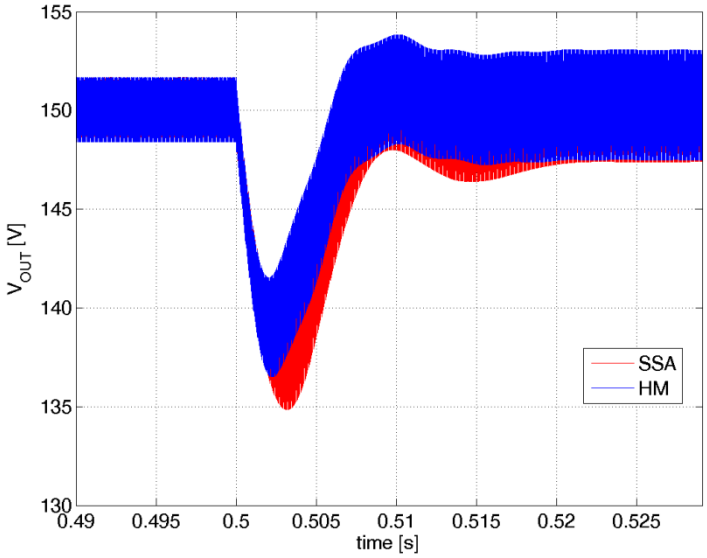

Figure 65 Output voltage for a step output current variation from 400 to 800 mA and a load resistance of 1kΩ.

7.2.4. Experimental Results: Comparison between a Robust and Classic Controller

The performances of the robust controller based on the Hammerstein model have been compared with a classic PI controller. The tuning of the PI controller has been made in the frequency domain using the classical method. More exactly the proportional and integral gain have been obtained by setting the phase margin equal to 45° with a crossover frequency equal to 150 rad/s. In order to improve the performance of the controller an additional tuning has been made online on the experimental setup. The proportional and integral gain adopted are respectively $1.68 \cdot 10^{-4}$ and 0.6.

The digital implementation of the PI requires at every sample time three sums and three multiplication while the digital robust controller needs nine sums and products so three times the operations of the PI. In general the nonlinear functions are onerous for a digital system, but in this case the digital implementation of the nonlinear gain necessity a lookup table which requires an amount of memory that depends on the desired resolution. All in all, the digital robust controller requires only basic operation and a slight increase of the computational demand to the programmable hardware (DSP or FPGA). For these reasons an upgrade of the microprocessor is not required.

In order to compare the robust control performance with those achievable with the classical PI, two set of tests have been performed. In the former the adopted input inductance corresponds to the design value and it is equal to 1.48 mH with a parasitic resistance of r_{L1}=40 mΩ. In the latter, the input inductance it is equal to 2 mH with a parasitic resistance of r_{L1} =125 mΩ; it simulates a big variation of these parameters. This test is motivated by the fact that the most typical variation which can occur is the variation of the parasitic resistances of both the input inductance and the output capacitance. Such a variation, due to the heating for joule losses mixed to environmental temperature variations, can be even bigger than 35%. It should be added to such a variation the speeding of the values of such resistances in the different exemplars of the same inductance, due to the manufacturing process. Even such an effect can be conspicuous. As far as the inductance term variation is concerned, the only reason why it can vary so strongly is the magnetic properties of nucleus of the inductance vary because of either the circulating current (high frequency harmonics) or any damage. In this last case, the scope is to show that the system is able to continue working without any loss in the control performance even in presence of a damage of the inductance. Nevertheless, the reason why such a variation has been applied is that it is not practically easy to impose experimentally a variation. The simpler thing to do has been to directly substitute the inductance with another different (modifying at the same time both the inductance and its parasitic resistance). Figure 66 shows the duty-cycle vs. time for a step variation of the reference voltage from 30 V to 150 V and subsequent load variation from 175 Ω to 350 Ω. It can be noted that an increase of the duty cycle corresponds to an increase of the voltage reference with a comparable rise time. When the load reduction occurs, a corresponding duty cycle reduction is expected. A slight reduction of the duty cycle ripple is noticeable in the robust control case with a smoother transient subsequent the load variation. Correspondingly, Figure 67 shows the input current in the same conditions. The same considerations made on the duty cycle hold for the current waveform. The rise time in the two cases is almost comparable while the steady state ripple of the input current is considerably lessened in the robust control case. Moreover, the load transient is much smoother in the robust control case. Figure 68 shows the output voltage in the same previously set test conditions. Also in

this case the robust control permits a lower ripple in steady state and a faster rejection capability of the load variation. The different timing between the two controllers during the step load is due to the fact that, after the step reference voltage, which is synchronized in the two cases, the step variation of the resistance is made by hand by the user and thus there is no synchronization.

As for the second test, performed with a L_1=2 mH and r_{L1}=125 mΩ, different from the values adopted for the control system design (the input inductance is almost 1.35 times bigger while its parasitic resistance is 3.12 time bigger), figures from Figure 69 to Figure 71 show the duty cycle, input current and output voltage during a voltage step from 30 V to 150 V and subsequent load variation from 175 Ω to 350 Ω. These figures show clearly the robustness vs. parameters' variations of the robust control respect to the PI control. The three variables obtained with the PI, i.e. the duty cycle, the input current and the output voltage show an increasing oscillating behavior after the first transient clearly leading to an unstable behavior. On the contrary, robust control exhibits a stable behavior as expected. After the load reduction, the waveforms obtained with the PI maintain a significant oscillating behavior (close to the stability limit) whereas the robust control guarantees a stable behavior with constant values of the variables.

The performance of the two controllers are summarized in Table 8 and Table 9 by the evaluation of the Integral Absolute Error (IAE), Integral Time Absolute Error (ITAE), rise time, settling time (5%) and finally overshoot or maximum error of tracking. This kind of analysis has been performed using $2 \cdot 10^5$ samples. These index of performance are also evaluated in the case L_1=2mH even if the system in rated condition is unstable. In conclusion, the PI and the robust controller are very similar in the rated condition, but this is to be expected, since the improvements brought by the robust controller are not in terms of dynamic performance, which maintain almost the same, but in terms of robustness versus parameters' variations and unmodeled dynamics.

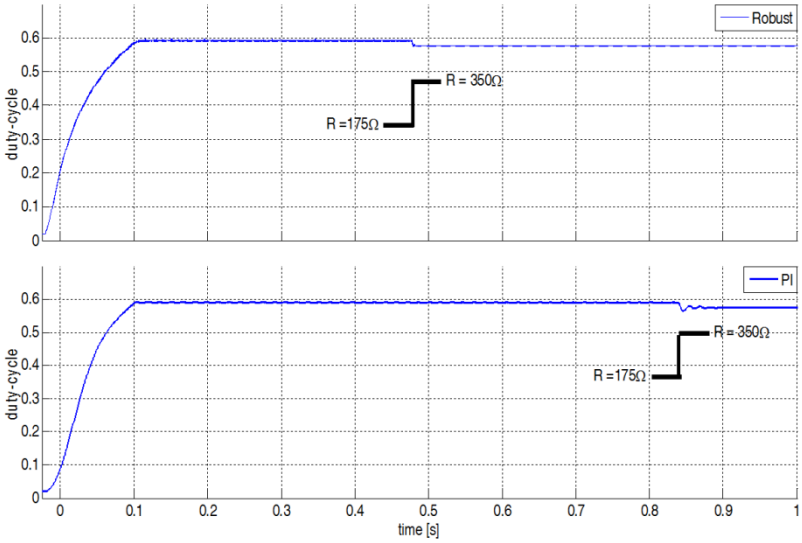

Figure 66 Duty-cycle vs. time for a step variation of the reference from 30 V to 150 V and a subsequent load variation from 175 Ω to 350 Ω; the input inductance is equal to 1.48 mH.

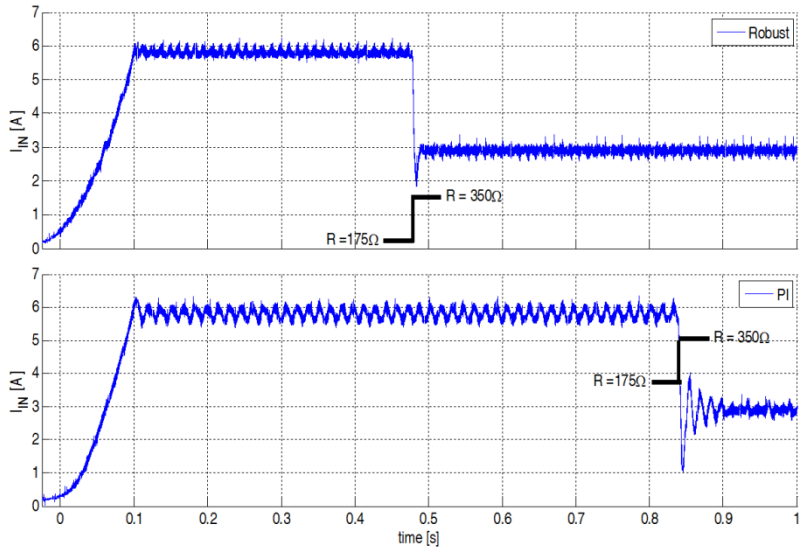

Figure 67 Input current vs. time for a step variation of the reference voltage from 30 V to 150 V and subsequent load variation from 175 Ω to 350 Ω; the input inductance is equal to 1.48 mH.

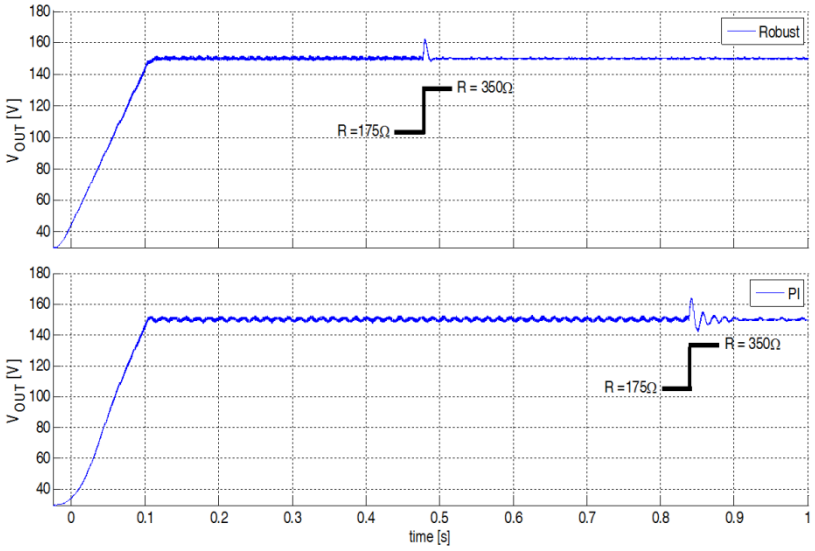

Figure 68 Output voltage vs. time for a step variation of the reference voltage from 30 V to 150 V and subsequent load variation from 175 Ω to 350 Ω; the input inductance is equal to 1.48 mH.

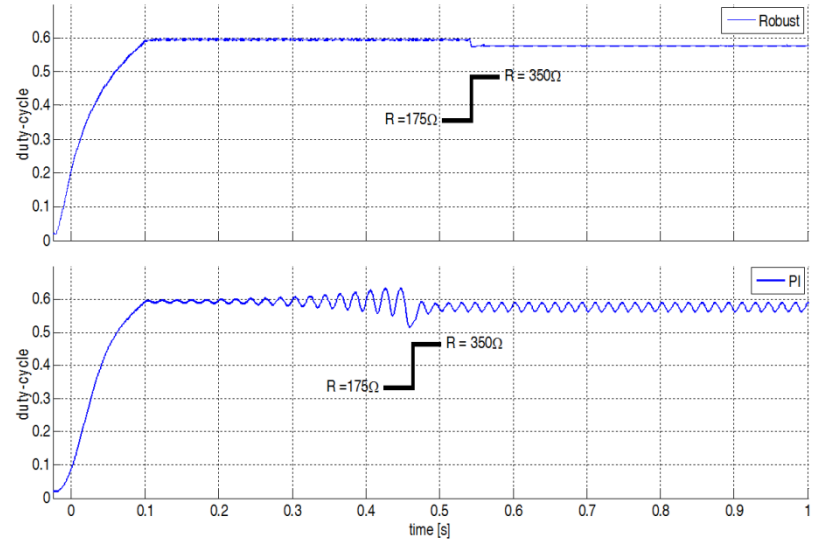

Figure 69 Duty-cycle vs. time for a step variation of the reference voltage from 30 V to 150 V and subsequent load variation from 175 Ω to 350 Ω; the input inductance is equal to 2 mH.

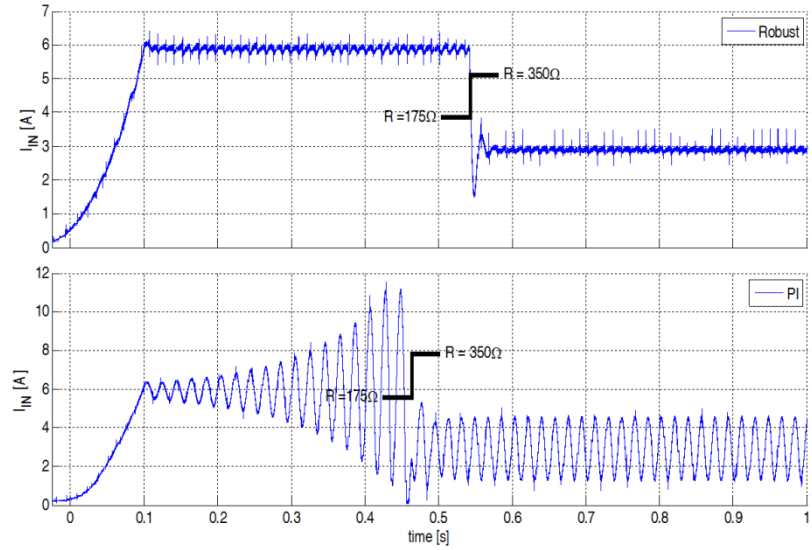

Figure 70 Input current vs. time for a step variation of the reference voltage from 30 V to 150 V and subsequent load variation from 175 Ω to 350 Ω; the input inductance is equal to 2 mH.

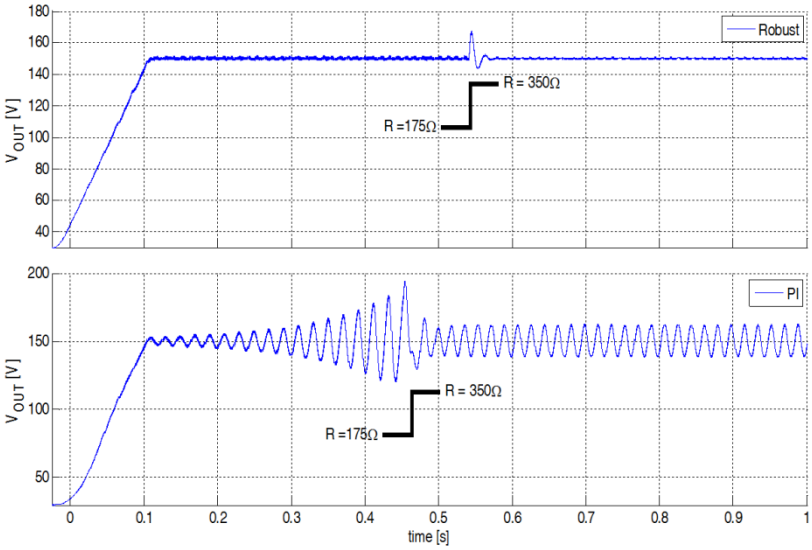

Figure 71 Output voltage vs. time for a step variation of the reference voltage from 30 V to 150 V and subsequent load variation from 175 Ω to 350 Ω; the input inductance is equal to 2 mH.

Table 8 Comparison of the controllers during a step reference from 30 V to 150 V.

	PI Controller		Robust controller	
	L_1=1.48mH	L_1=2mH	L_1=1.48mH	L_1=2mH
IAE	2,60309	23,86568	1,59561	1,75521
ITAE	0,96820	20,62960	0,74260	0,85901
Rise time [s]	0,08016	0,08002	0,09688	0,09712
Settling time [s]	0,09832	Infinite	0,10688	0,10658
Overshoot	/	2%	/	/

Table 9 Comparison of the controllers during a step load from 175 to 350 Ω.

	PI Controller		Robust controller	
	L_1=1.48mH	L_1=2mH	L_1=1.48mH	L_1=2mH
IAE	0.2157	1.25	0.1118	0.1762
ITAE	0.1887	0.6748	0.0581	0.1005
Max error [V]	14.12	16.88	12.29	17.39
Settling time [s]	5.78m	Infinite	4.77m	6.17m

7.3. Control of the QBC2 with a Feedforward Action Model-Based

In this section, a linear controller plus a feed-forward action model-based is designed for the *QBC2*. The rated parameters of the *QBC2* are shown in Table 6, whereas the laboratory prototype is shown in Figure 72. The feed-forward action is based on the SSA model of the *QBC2*; therefore a validation of the model is required.

The SSA model (89) has been suitably modeled in Matlab®-Simulink® environment for validation purpose. The validation process has been carried out in two phases: validation of the nonlinear SSA model; validation of the static gain and the small-signal transfer function.

7.3.1. Validation of the nonlinear SSA model

The SSA model has been implemented in two versions: the conventional and the so-called modified SSA. The modified SSA model is an extension of the SSA model (89). It takes into consideration the presence of the diodes and of the mono-directional switch in the system. As a matter of fact, if the SSA model is straightforward adopted, the currents flowing through the inductances L_1 and L_2 can

even become negative, during transients involving a temporary discontinuous behavior. This is not allowed in the real system, because of the presence of diodes D_1, D_2 and D_3 as well as the mono-directional switch S. Solving the state equation (89) requires the presence of 4 integrators, anyway the traditional integrator lead to an incorrect modeling since the diode currents cannot reverse. This has been simply overcome by adopting, as integrators of the first 2 state equations (89), two saturated integrators with outputs bounded between 0 and $+\infty$. Figure 74 from *a* to *e* shows the same kind of figures sketched in Figure 73, as obtained with the modified SSA model. It can be easily observed that, not only the mono-directional nature of the currents in the inductances is properly represented, but also the response of the model very well matches that of the real system all the components of the state vector, as well as in the output voltage waveform, with waveforms that are almost superimposed.

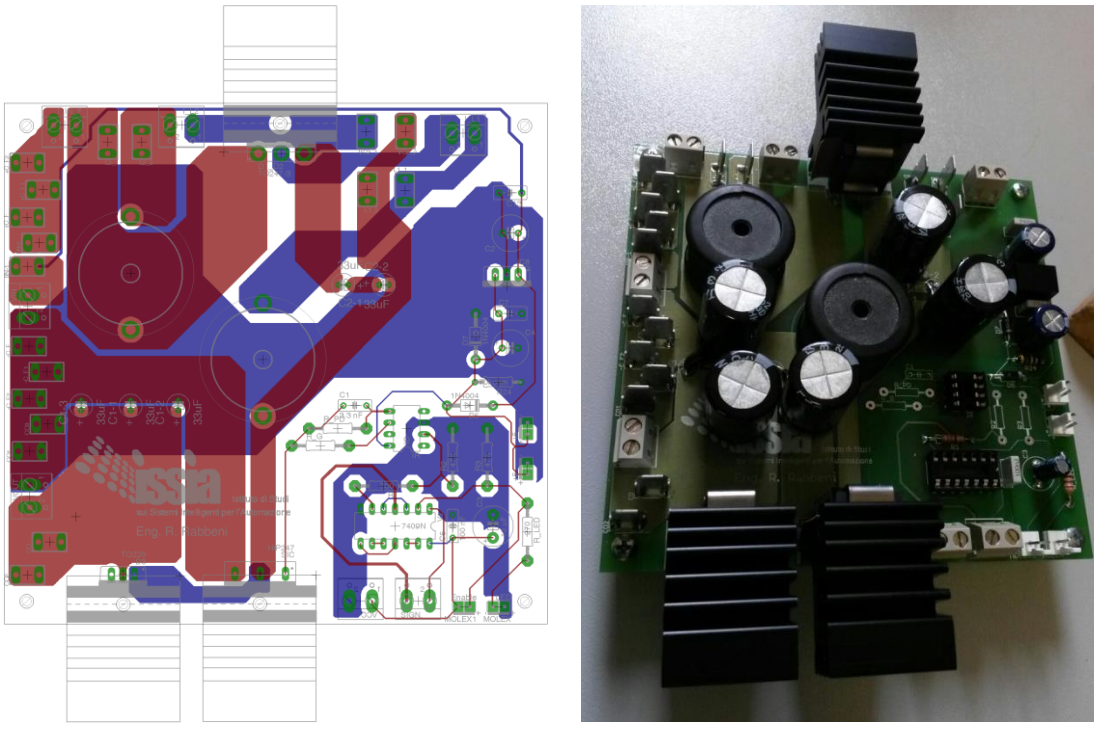

a) b)

Figure 72 *QBC2* prototype: a) PCB layout; b) PCB board.

7.3.2. Validation of the static gain and the small-signal model

The contemporary validation of the static gain expression, equation (90), and the small-signal transfer function has been performed. The block diagram representing the logic of such a validation is shown in Figure 75. The real power converter has been given a duty-cycle, obtained as the sum of a constant value *D* and value $\tilde{d}$ variable with sinusoidal law. The output voltage of the real system has been therefore compared, under such an input, with the corresponding obtained as the sum of V_{OUT} and $\tilde{v}_{OUT}$, where V_{OUT} is the output of the static gain expression having *D* and V_{IN} as inputs, and $\tilde{v}_{OUT}$ is the output of the small-signal transfer function having $\tilde{d}$ as input. Figure 76 shows the waveform of $\tilde{d}$ as well as the out voltages of the system, as above recalled under a constant output reference voltage equal to 120 V with *D*=0.5 and load resistance equal to R = 48 Ω. The waveform of $\tilde{d}$ presents initially a null value, so to verify the correctness of the static gain expression, and then subsequently increasing amplitudes so to verify the progressive un-match of the small-signal transfer function output versus the real converter output for operating points progressively far from the equilibrium one. Figure 76 clearly shows a very good matching of the static gain expression with the static output of the converter. At the same time, for small variations $\tilde{d}$ around the equilibrium point, the small signal transfer function properly describes the real system behavior. Above a certain threshold value of the amplitude of $\tilde{d}$, the output of the small signal transfer function becomes unreliable, as expected.

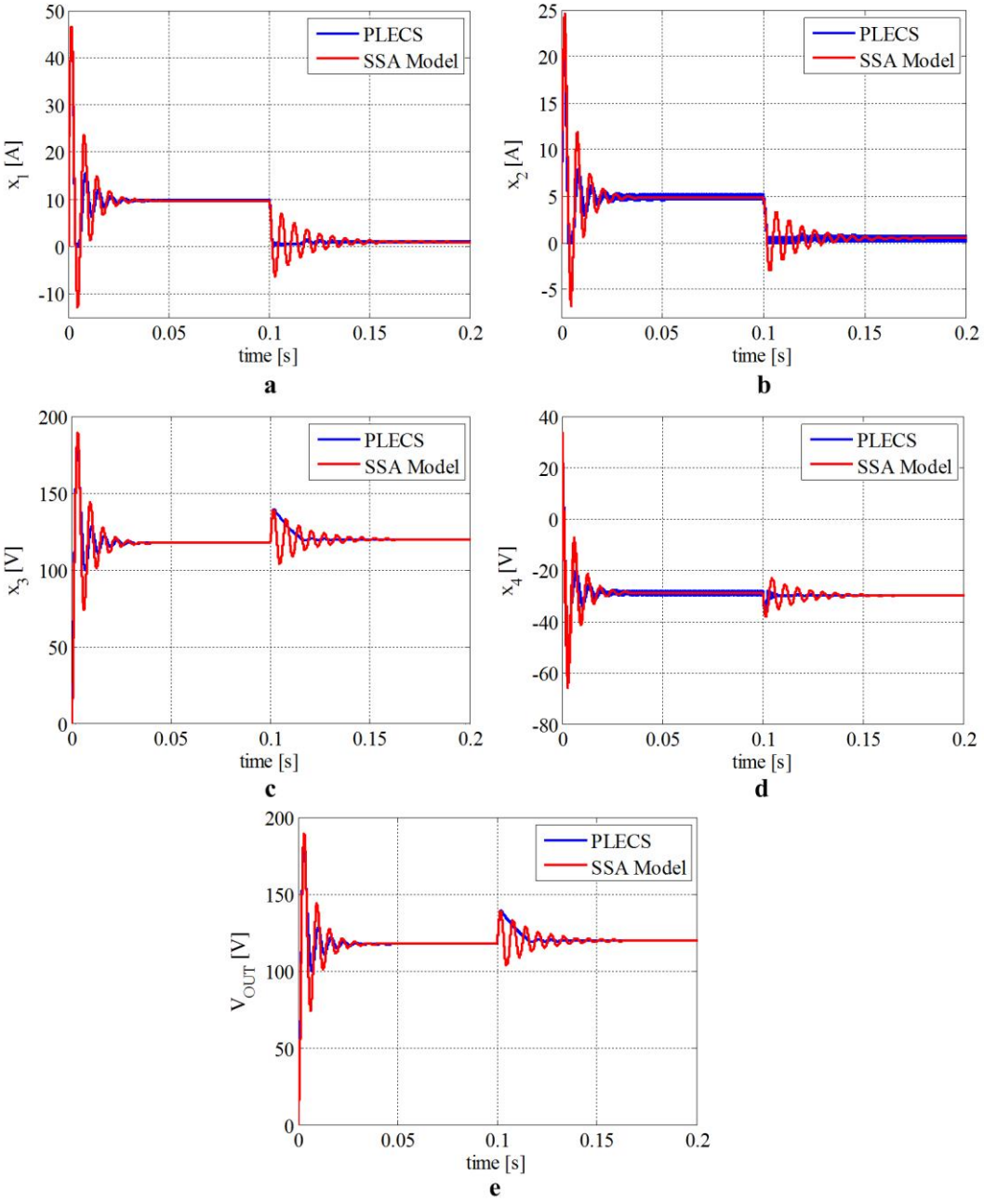

Figure 73 Comparison between PLECS and the SSA model of the *QBC2*: a) Current of L_1; b) Current of L_2; c) Voltage of C_1; d) Voltage of C_2; e) output voltage.

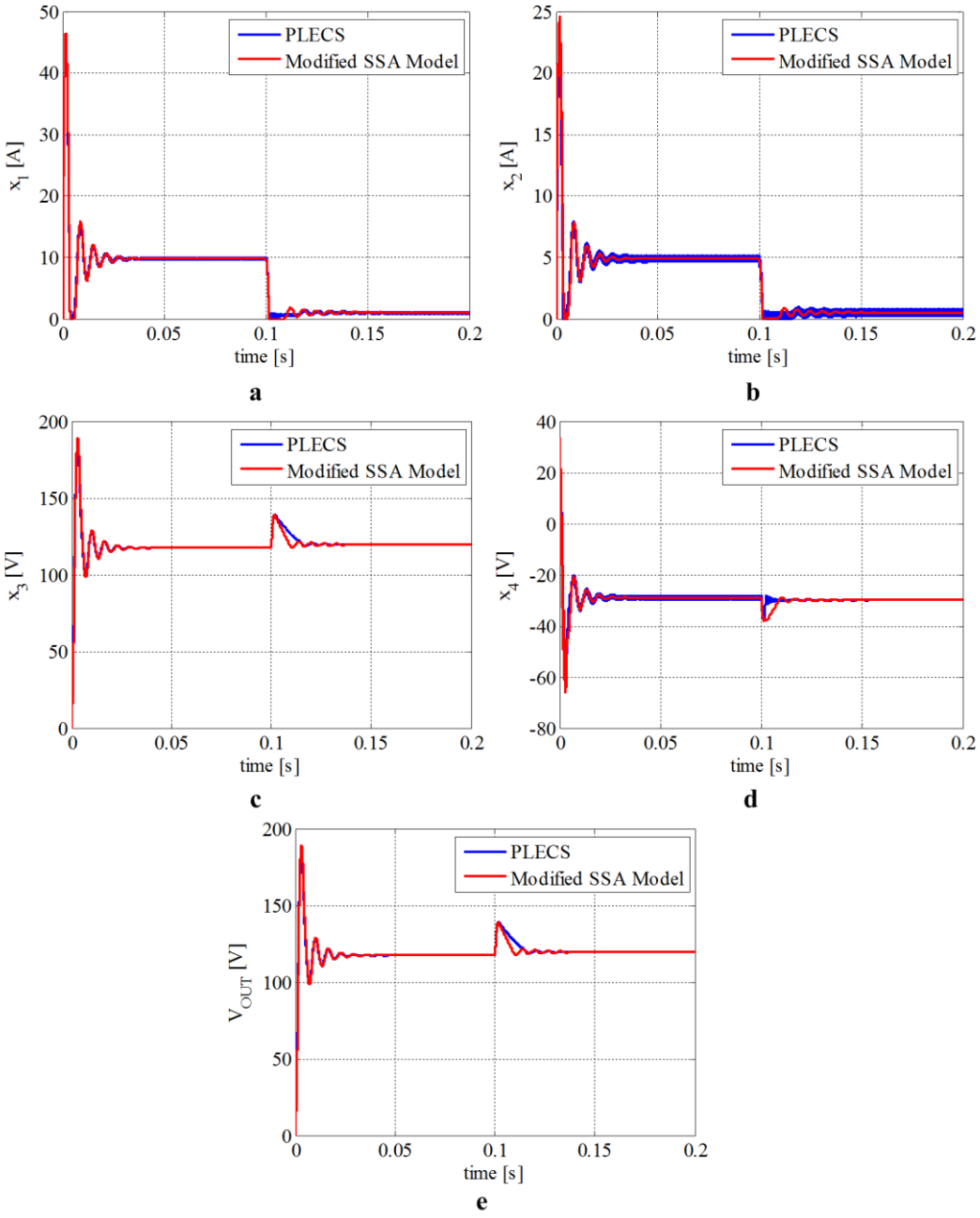

Figure 74 Comparison between PLECS and the Modified SSA model of the *QBC2*: a) Current of L_1; b) Current of L_2; c) Voltage of C_1; d) Voltage of C_2; e) output voltage.

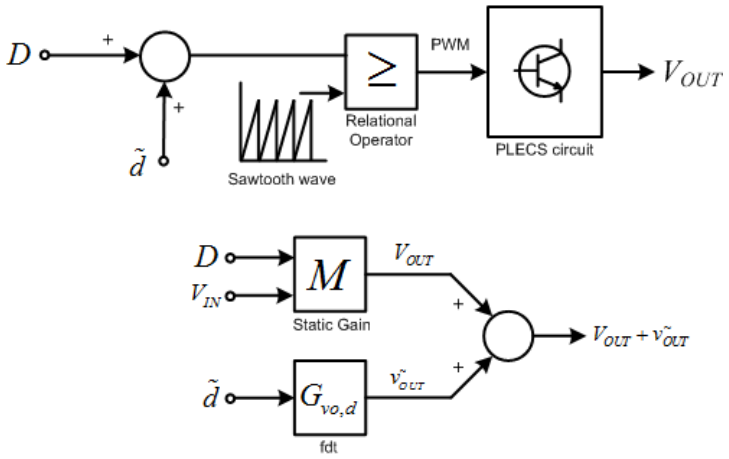

Figure 75 Block scheme for the validation of the small-signal model and the static gain of the *QBC2*.

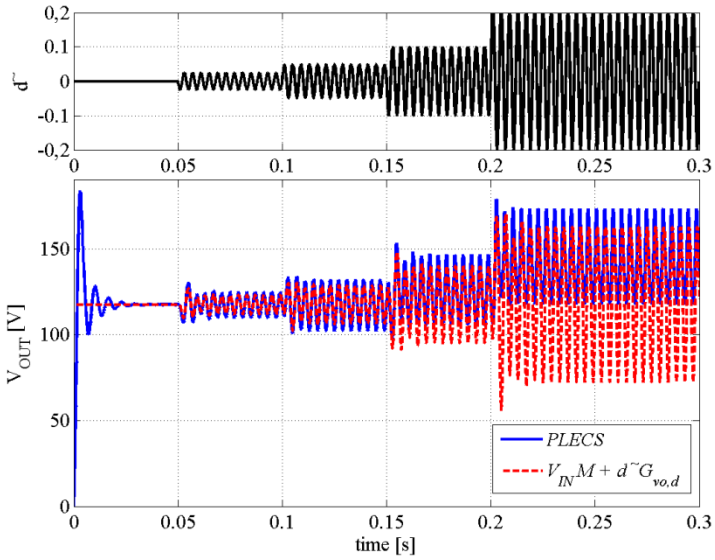

Figure 76 Validation of the small-signal model and the static gain of the *QBC2* using the block scheme of Figure 75 where D=0.65 and $G_{vo,\,d}$ is the transfer function around the equilibrium point D=0.65 with R=48 Ω.

7.3.3. Feedforward controller model-based

Using the validated SSA model of the *QBC2* a feed-forward controller model-based has been implemented. The implemented control scheme has been shown in Figure 77 where there is a feed-forward action plus a simple integrator regulator having a transfer function equal to $\frac{K_I}{s}$. The feed-forward action has been obtained using the inverse of the equation (90) that surely exists because the function (90), *f*(*D*), is strictly monotone in a subset belonging to [0, 1]. In Figure 78, in dashed line, has

been shown the closed loop response of the QBC assuming K_I and V_{ref} respectively equal to 0.14 and 120 V. The output voltage of the converter presents a very fast response against reference step transient and so a high overshoot. Anyway, this is only a numerical problem because it is practically impossible to provide a step variation of the reference in a real system. In order to take into account this phenomenon a pre-filtering, PF, of the reference has been added to the control scheme of Figure 77. Using a low pass filter having a cut off frequency equal to 1 KHz, the response of the controlled system has been shown in Figure 78 in continuous line. It is also possible to observe that the presence of the integrator is able to nullify the steady-state error even if there is a load variation from 48Ω to 480Ω.

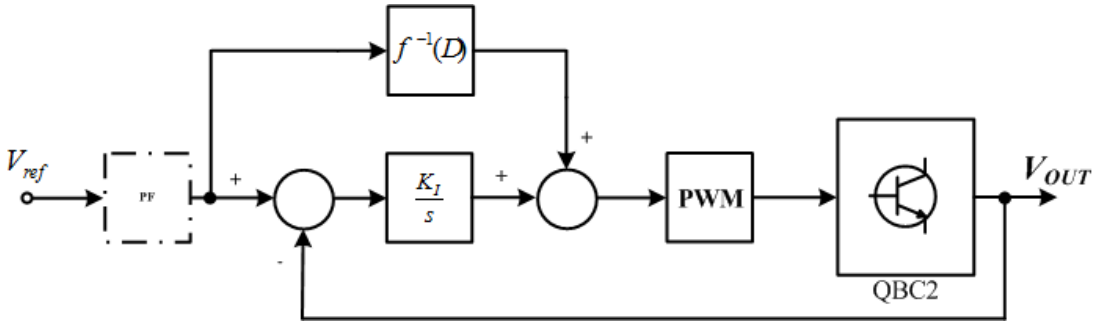

Figure 77 Feed-forward control scheme.

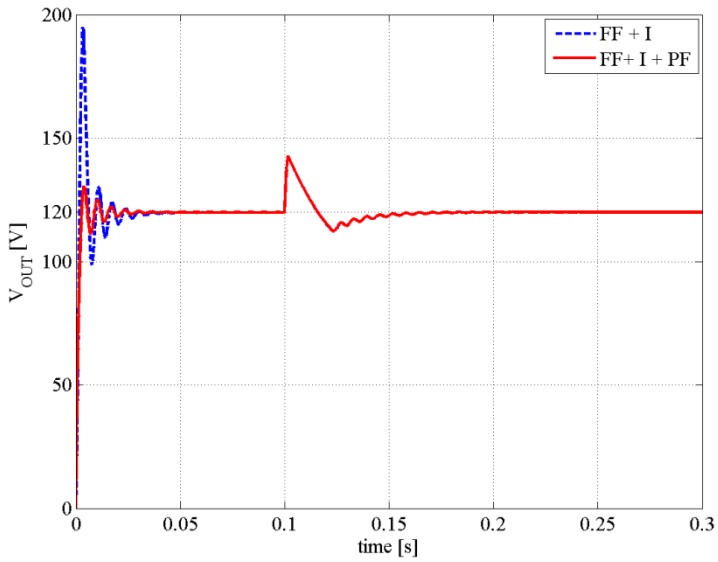

Figure 78 Regulated output voltage of the *QBC2* by means an integral regulator plus a feed-forward action.

7.4. Conclusion

The quadratic Boost converters *QBC1* and *QBC2* have a high static gain sensitivity in the ordinary duty-cycle operating range. In the standard Boost converter, this kind of gain sensitivity is instead present for higher and actually not usable values of the duty-cycle. For this last reason, the control of the QBCs is not a trivial task. The design of a robust control law, allows to contrast the gain sensitivity and the model/parameter uncertainty. The experimental results confirm the performances of the designed H_2 optimal robust controller. Even if there are parameter variations the controller is able to guarantee the voltage reference. The design procedure of the robust controller has been developed using both the two modeling approaches, SSA and HM model of the *QBC1*.

The SSA model of a *QBC2* prototype has been validated. Imposing the current constraint introduced by means of the power diodes the SSA model is able to average describes the transition between the CCM and DCM with a better approximation. All in all, the knowledge of the *QBC2* model has been used to design a simple integrator regulator plus a feedforward action based on the analytical knowledge of the static gain.

Chapter 8

FS-MPC and M^{2}PC for Active Power Filtering Systems

8.1. Introduction

Maintaining a good Power Quality (PQ) level in modern electrical smart grids (Salmeron & Litran 2010) is a vital issue to ensure reliability, security and efficiency and it is currently becoming hugely important due to the proliferation of non-linear loads, power conversion systems, renewable energy sources, distributed generation sources, Plug-in Electric Vehicles (PEVs) (Moses et al. 2010). A variety of Flexible AC Transmission System (FACTS) related equipment (Dionise & Lorch 2010; Todeschini & Emanuel 2010; Singh et al. 1999) have been developed in the past years to improve power quality, such as: Active and Hybrid power filter, Static compensator (STATCOM/DSTATCOM), Static Var Compensator (SVC), Unified Power Flow/Quality Controller (UPFC/UPQC), Dynamic Voltage Restorer (DVR). Active powers filters allow "controlled" harmonic reduction and are not affected by the limits of their passive counterparts, such as the introduction of resonances onto the power system, impossibility of current limiting (other than fuses), possible overloaded operation if the supply voltage quality deteriorates (Beaty 2004). However, the accurate management of active filters (Akagi 2005) is a demanding control challenge, as high bandwidth regulation is required possibly using a reasonable switching frequency, and in the presence of supply disturbances (Buso et al. 1998; Jintakosonwit et al. 2002).

The most common active filter configuration is the Shunt Active Filter (SAF) which can be controlled in several ways (Cirrincione et al. 2009; Cirrincione et al. 2008; Zahira & Peer Fathima 2012). The control strategy for SAF consists on the generation of the reference currents that must be provided to the power filter to compensate reactive power and harmonic currents demanded by the nonlinear load. This involves a set of currents in the phase domain which will be tracked generating the switching signals applied to the power electronic converter by means of an

appropriate closed-loop controller. Usually, it is useful to calculate the compensating current in terms of the reference source current. In the fixed frequency controller, the error between the reference and actual current is fed through a PI controller which integrates the error and generates a variable voltage value for the modulator. PI controllers in a stationary frame are unable to completely eliminate the steady state error and to achieve satisfactory reference tracking performance since the reference signals are periodical quantities containing several harmonics. The tracking accuracy for specified harmonics may be improved by using multiple related synchronous reference frames (Zmood et al. 2001; Espí Huerta et al. 2010), but the need for multiple band-pass filters and interactions among them make the design and the tuning of the control difficult. Alternatively, to avoid multiple reference frame transformations, a resonant controller may be used (Mattavelli 2001), but its tuning is difficult and can lead to instability. Reducing the number of sensors has also been investigated, using a state feedback control and a suitable observer (Kwan et al. 2007). Finally, dead beat control strategies have been considered in several papers (Malesani et al. 1999) coupled with a PI -based DC-Link voltage control.

In recent years, Model Predictive Control (MPC) has been applied for the control of power converters due to its several advantages, like fast dynamic response, no need of modulation, easy inclusion of system nonlinearities, constraints and requirements in the controller (Rodriguez et al. 2007; Cortés et al. 2007; P. Cortés et al. 2008). MPC considers the system model for predicting its future behavior and determining the best control action according to a cost function representing the desired behavior. Considering that power converters are systems with a finite number of states, the Finite Control Set MPC (FCS-MPC) optimization problem consists in the prediction of the system behavior for each possible state. Then, each prediction is evaluated using the cost function and the state that minimizes it, is selected (Kouro et al. 2009). This approach has been successfully applied for the current control in three-phase inverters (Rodriguez et al. 2007), matrix converters, power control in an active front end rectifiers (Patricio Cortés et al. 2008), and torque and flux control of an induction machine (Geyer et al. 2009; Papafotiou et al. 2009).

The lack of a modulator, although being an advantage for the performance of the system in case of large transient, it is also a drawback under steady-state and small

transient conditions when the high bandwidth of the control is not necessary and the higher current ripple, due to the limited set of available control actions, is more evident. This chapter investigates the development and implementation of a novel Modulated MPC (M^2PC) algorithm suitable for SAF control which retains most of the advantages of the MPC such as the presence of a cost function and the use of a single loop for improved responsivity and larger bandwidth, but exploits a modulator for reducing the current ripple. The modulator uses the cost function for selecting the vectors and their application times for the next sampling period. Experimental results show the excellent steady state and transient performance of the proposed filtering system.

8.2. System Description and Modeling

In its classical configuration, a SAF consists of a VSI inverter whose DC side is connected to a capacitors bank whereas its AC side is connected to the main by a set of series inductors as shown in Figure 79.In such configuration, the SAF can produce any set of currents which have a null sum and, therefore, compensate the reactive power and the current harmonics drawn by a non-linear load. On the other hand, the grid provides only the active power required to supply the load and maintains the SAF DC-Link at the desired voltage.

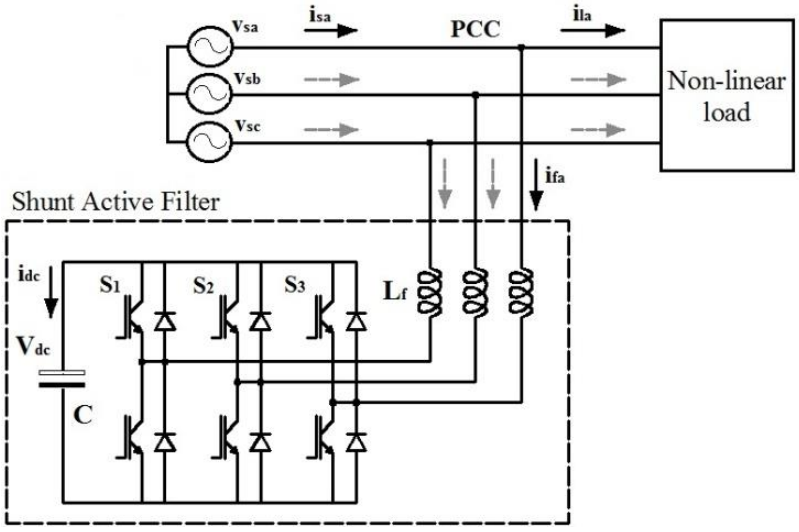

Figure 79 Typical structure of 3-wires Shunt Active Filter.

With reference to the scheme of Figure 79 and considering a sinusoidal symmetrical three-phase voltage source with a balanced load, in the *abc* frame it is possible to reduce the system order to the third order, represented by the state variables i_{fa}(t), $i_{fb}(t)$ and $V_{dc}(t)$. Neglecting the equivalent impedance of the grid and the conduction voltage drop in the switching devices, with the input filter modeled as a set of identical linear series inductances, the dynamics of the SAF currents can be modeled as follows.

$$\begin{cases} \frac{di_{fa}(t)}{dt} = \frac{1}{L_f} v_{sa}(t) - \frac{R_f}{L_f} i_{fa}(t) - \frac{1}{3L_f}[2S_a(t) - S_b(t) - S_c(t)]V_{dc} \\ \frac{di_{fb}(t)}{dt} = \frac{1}{L_f} v_{sb}(t) - \frac{R_f}{L_f} i_{fb}(t) - \frac{1}{3L_f}[2S_b(t) - S_a(t) - S_c(t)]V_{dc} \end{cases} \quad (148)$$

where R_f and L_f are the equivalent resistance and inductance of the input filter whereas the switching functions $S_a(t)$, $S_b(t)$ and $S_c(t)$ are equal to 1 if the corresponding device is ON, 0 if the device is OFF. The dynamic of the converter dc side is expressed by the following equation, where the DC current through the converter is defined from the switching functions and AC currents.

$$\frac{dV_{dc}(t)}{dt} = \frac{1}{C}\{[S_a(t) - S_c(t)]i_{fa}(t) + [S_b(t) - S_c(t)]i_{fb}(t)\} \quad (149)$$

The supply current can then be obtained by the filter and load currents as in (150).

$$\begin{cases} i_{sa}(t) = i_{la}(t) + i_{fa}(t) \\ i_{sb}(t) = i_{lb}(t) + i_{fb}(t) \end{cases} \quad (150)$$

Equations (148) and (149) provide a state space representation of the SAF in continuous time domain. The Euler approximation is then used to obtain a discrete model of the system:

$$\begin{cases} i_{fa}(k+1) = \left(1 - \frac{R_f h}{L_f}\right) i_{fa}(k) - \frac{h}{L_f} Q_1 \underline{S}(k) V_{dc}(k) + \frac{h}{L_f} v_{sa}(k) \\ i_{fb}(k+1) = \left(1 - \frac{R_f h}{L_f}\right) i_{fb}(k) - \frac{h}{L_f} Q_2 \underline{S}(k) V_{dc}(k) + \frac{h}{L_f} v_{sb}(k) \\ V_{dc}(k+1) = V_{dc}(k) + \frac{h}{C} P_1 \underline{S}(k) i_{fa}(k) + \frac{h}{C} P_2 \underline{S}(k) i_{fb}(k) \end{cases} \quad (151)$$

Where h is the sampling time, k represents the discrete sampling instant and

$$Q_1 = \frac{1}{3}(2 \quad -1 \quad -1)$$

$$Q_2 = \frac{1}{3}(-1 \quad 2 \quad -1)$$

$$P_1 = (1 \quad 0 \quad -1)$$

$P_2 = (0 \quad 1 \quad -1)$

$\underline{S}(k) = [S_a(k) \ S_b(k) \ S_c(k)]^T$

8.3. SAF Model Predictive Control

The first control approach investigated in this paper for active filters applications is a FCS-MPC, where the choice of possible switching combinations is limited to 8, which are the output states available for a traditional two-level three-phase converter:

$$\underline{S}(k) \triangleq \left\{ \begin{bmatrix} 0 \\ 0 \\ 0 \end{bmatrix}, \begin{bmatrix} 0 \\ 0 \\ 1 \end{bmatrix}, \begin{bmatrix} 0 \\ 1 \\ 0 \end{bmatrix}, \begin{bmatrix} 0 \\ 1 \\ 1 \end{bmatrix}, \begin{bmatrix} 1 \\ 0 \\ 0 \end{bmatrix}, \begin{bmatrix} 1 \\ 0 \\ 1 \end{bmatrix}, \begin{bmatrix} 1 \\ 1 \\ 0 \end{bmatrix}, \begin{bmatrix} 1 \\ 1 \\ 1 \end{bmatrix} \right\} \tag{152}$$

Ideally, the FCS-MPC algorithm would determine and apply the best switching vector at the instant k, $\underline{S}(k)$, in a way that a predefined cost function is minimized at the instant $k+1$. When the values of states and input variables are available by sensing, the system model developed in (151) provides an estimate of the system state variables at the next sampling instant $k+1$. It is therefore possible to determine, at the instant k, the best value of the inverter state $\underline{S}(k)$ among the possible 8 by minimizing a cost function obtained combining these predicted values with predicted reference values. Nevertheless, in practice such calculations require some elaboration time, meaning that they cannot be completed according to the timing scenario that led to (151). Assuming that the above calculations can be completed within one sampling period of the system, it is possible to calculate the state variables values at the time instant $k+1$. Then, the best inverter output state at the instant $k+1$, $\underline{S}(k+1)$, that minimizes the defined cost function at the instant $k+2$ is calculated by moving (151) one step forward. Combining the system model at the time instants $k+1$ and $k+2$, and assuming that the supply voltages may be considered almost constant during a sampling period h of the control system (i.e. $\underline{v}_s(k)=\underline{v}_s(k+1)$) the following system is obtained:

$$\underline{X}(k+2) = A_2\left(\underline{S}(k+1)\right)\underline{X}(k) + B_2\underline{U}(k) \tag{153}$$

where the vectors are given by:

$$\underline{X}(k+2) = \left[i_{fa}(k+2)\ \ i_{fb}(k+2)\ \ V_{dc}(k+2)\right]^T$$
$$\underline{U}(k) \quad = [v_{sa}(k)\ \ v_{sb}(k)]^T \tag{154}$$

Whereas the matrices are the following:

$$A_2 = \begin{bmatrix} a11 & a12 & a13 \\ a21 & a22 & a23 \\ a31 & a32 & a33 \end{bmatrix}$$

$$B_2 = \begin{bmatrix} b11 & 0 \\ 0 & b22 \\ b31 & b32 \end{bmatrix}$$

$$a11 = \left(1 - \frac{R_f h}{L_f}\right)^2 - \frac{h^2}{L_f C} Q_1 \underline{S}(k+1) P_1 \underline{S}(k)$$

$$a12 = -\frac{h^2}{L_f C} Q_1 \underline{S}(k+1) P_2 \underline{S}(k)$$

$$a13 = -\frac{h}{L_f} Q_1 \left[\left(1 - \frac{R_f h}{L_f}\right)\underline{S}(k) + \underline{S}(k+1)\right]$$

$$a21 = -\frac{h^2}{L_f C} Q_2 \underline{S}(k+1) P_1 \underline{S}(k)$$

$$a22 = \left(1 - \frac{R_f h}{L_f}\right)^2 - \frac{h^2}{L_f C} Q_2 \underline{S}(k+1) P_2 \underline{S}(k)$$

$$a23 = -\frac{h}{L_f} Q_2 \left[\left(1 - \frac{R_f h}{L_f}\right)\underline{S}(k) + \underline{S}(k+1)\right]$$

$$a31 = \frac{h}{C} P_1 \left[\underline{S}(k) + \left(1 - \frac{R_f h}{L_f}\right)\underline{S}(k+1)\right]$$

$$a32 = \frac{h}{C} P_2 \left[\underline{S}(k) + \left(1 - \frac{R_f h}{L_f}\right)\underline{S}(k+1)\right]$$

$$a33 = 1 - \frac{h^2}{L_f C}\left[P_1 \underline{S}(k+1) Q_1 \underline{S}(k) + P_2 \underline{S}(k+1) Q_2 \underline{S}(k)\right]$$

$$b11 = b22 = \frac{h(2L_f - R_f h)}{{L_f}^2}$$

$$b31 = \frac{h^2}{L_f C} P_1 \underline{S}(k+1)$$

$$b32 = \frac{h^2}{L_f C} P_2 \underline{S}(k+1)$$

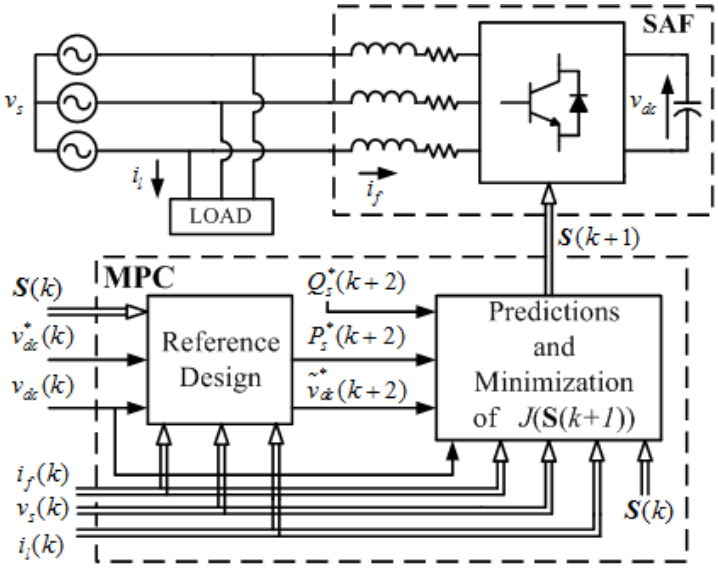

Figure 80 Schematic diagram of a FCS-MPC.

The vector in (154) represents the predicted values of active filter currents and voltage at the instant *k+2* and the supply voltages at the time instant *k*. The load currents i_{la} and i_{lb} are sensed in the active filter configuration. Given the high sampling frequency used in this FCS-MPC, it is a viable approximation to consider:

$$\begin{aligned} i_{sa}(k+2) &= i_{la}(k) + i_{fa}(k+2) \\ i_{sb}(k+2) &= i_{lb}(k) + i_{fb}(k+2) \end{aligned} \tag{155}$$

Hence the predicted system state is defined:

$$\underline{X_p}(k+2) = [i_{sa}(k+2)\ \ i_{sb}(k+2)\ \ V_{dc}(k+2)]^T \tag{156}$$

from which the control relevant variables (the active power P_s, the reactive power Q_s and the DC-Link voltage V_{dc}) are predicted as in (157)

$$\begin{aligned} P_{sp}(k+2) &= \underline{v_s^T}(k)\begin{bmatrix} 2 & 1 & 0 \\ 1 & 2 & 0 \end{bmatrix}\underline{X_p}(k+2) \\ Q_{sp}(k+2) &= \underline{v_s^T}(k)\begin{bmatrix} 0 & \sqrt{3} & 0 \\ -\sqrt{3} & 0 & 0 \end{bmatrix}\underline{X_p}(k+2) \\ V_{dcp}(k+2) &= [0 \quad 0 \quad 1]\underline{X_p}(k+2) \end{aligned} \tag{157}$$

Again, the grid voltages can be supposed approximately constant in two sampling periods due to their lower frequency when compared to the much higher sampling frequency of the SAF. The proposed control algorithm uses the above prediction model to select the switching functions $\underline{S}(k+1)$ which minimize a cost function of the form:

$$\begin{aligned} J\big(s(k+1)\big) = {} & \lambda_1\left|V_{dc}^*(k+2) - V_{dcp}(k+2)\right| + \\ & +\lambda_2\left|P_s^*(k+2) - P_{sp}(k+2)\right| + \\ & +\lambda_3\left|Q_s^*(k+2) - Q_{sp}(k+2)\right| \end{aligned} \tag{158}$$

Where x^* indicate reference values and $\boldsymbol{\lambda_1}$, $\boldsymbol{\lambda_2}$ and $\boldsymbol{\lambda_3}$ are weighting factors that allow a proper balance among deviations of the controlled variables. A block scheme of the complete active filter control for the case of FCS-MPC is shown in Figure 80.

8.4. Modulated Model Predictive Control

One of the major advantages of FCS-MPC is that several control targets, variables and constraints can be included in a single cost function and simultaneously

controlled with a single control law. In this way typical variables such as current, voltage, torque or flux can be controlled while achieving additional control requirements like as example, switching frequency reduction, common mode voltage reduction and reactive power control. In traditional FCS-MPC, at each sampling time, all the possible control actions are compared in terms of cost and only the best one is selected for the next sampling period. If the converter state is constant during a sampling period, the quantities under control are affected by an higher ripple as a consequence of the finite number of possible converter states. To overcome this limit, this paper proposes the introduction of a suitable modulation scheme. Consistently with the MPC approach, the cost-function is used for selecting the converter states and application times which minimize the equivalent cost in a sampling period. A symmetric PWM pattern with adjacent states has been preferred for reducing harmonics, ripple and losses. So each sampling period is composed of two zero states and two active states which are symmetrically split around the center of the sampling period. Using the predictions for the traditional FCS-MPC described in the previous section, it is possible to determine the optimum sector of the Space Vector plane by just using a different cost function:

$$J_{sect}(k+1) = d_0 J_0 + d_1 J_1 + d_2 J_2 \tag{159}$$

where J_i with $\mathrm{i} = 0,1,2$ are the cost functions (158) calculated assuming $s(k+1)$ equal respectively to the zero vector, the first active vector and the second active vector of the considered sector. The d_i are the duty-cycles for the zero and active vectors and are calculated according to the following equations:

$$\begin{aligned} d_1 &= \frac{J_2}{J_1 + J_2 + \frac{J_1 J_2}{J_0}} \\ d_2 &= \frac{J_1}{J_1 + J_2 + \frac{J_1 J_2}{J_0}} \\ d_0 &= 1 - (d_1 + d_2) \end{aligned} \tag{160}$$

Essentially the cost functions values J_i for each sector are calculated by using (153)-(158) and the corresponding application times are calculated from (160). The optimum sector is then determined by minimizing the cost function of (159) used for

determining the optimal reference duty cycles $\underline{d}(k+1) = [d_a(k+1)\ d_b(k+1)\ d_c(k+1)]^T$ which are then applied to the converter as represented in Figure 81.

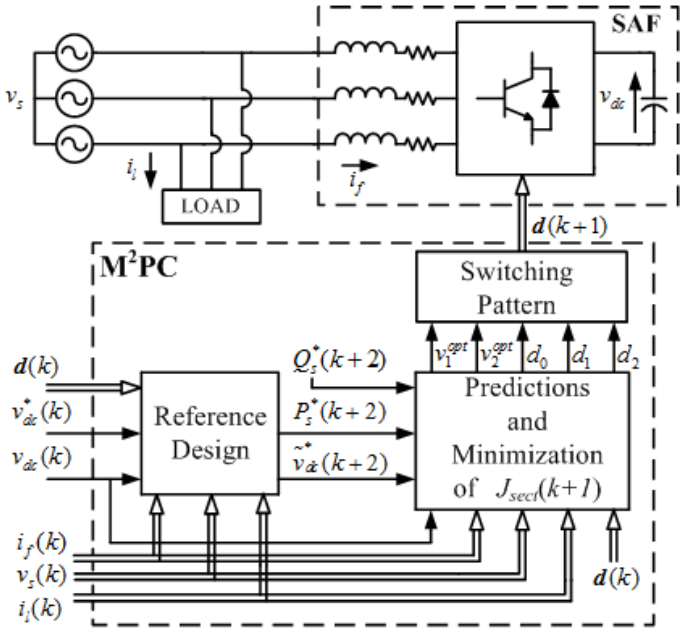

Figure 81 Schematic diagram of a FCS-M²PC.

8.5. References Prediction

Active power $P_s(k)$ and dc-link voltage $V_{dc}(k)$ are obviously coupled; therefore even reference signals for these two quantities will be function of each other. Given the reactive power reference $Q_s^*(k)$ and the dc-link voltage reference $V_{dc}^*(k)$ at the instant *k*, together with the knowledge of the current state of the system $\underline{X}(k)$, it is possible to calculate compatible references $P_s^*(k+2)$ and $\tilde{V}_{dc}^*(k+2)$. Since the dc-link capacitors compensate the reactive power fluctuations due to the non-linear load, the dynamic of the dc-link voltage control cannot be chosen arbitrarily large and needs to be much slower than the reactive power one. The required change in the active power flow to regulate the voltage at the desired value is given by:

$$P_{DC}(k+2) = \frac{C}{Nh}\left[{V_{dc}^*}^2(k+2) - {V_{dc}}^2(k+1)\right] \tag{161}$$

where N denotes the desired number of time steps required for reaching the desired value. The active power reference for the load is given by:

$$P_l^*(k+2) = \underline{v_s^T}(k)\begin{pmatrix}2 & 1\\ 1 & 2\end{pmatrix}\underline{i_{l1}}(k) \tag{162}$$

where $\underline{i_{l1}}(k) = [i_{la1}(k)\ i_{lb1}(k)]^T$ represents the vector of the first harmonics of the load current. Given the high sampling frequency used in this MPC, it is a viable approximation to consider $\underline{i_{l1}}(k) = \underline{i_{l1}}(k+2)$. The active power $P_l^*(k+2)$ is simply obtained by filtering (162) with a digital resonant filter having a resonance frequency equal to 50Hz. Finally, the total reference power at the supply side is therefore:

$$P_s^*(k+2) = P_l^*(k+2) + P_{DC}(k+2) \tag{163}$$

Equation (160), together with $Q_s^*(k+2) = 0$ and $V_{dc}^*(k+2)$ to ensure unity power factor operation of the system, constitute the reference set for the cost function (159). The minimization of active and reactive power errors allows also an automatic and fast synchronization with the grid as demonstrated by the presented results in the next section.

8.6. Experimental Results

In order to investigate the actual performances of the proposed control strategy by experimental testing, a prototype SAF was purposely built and a test rig was set up. According to the scheme of Figure 79, the SAF experimental prototype includes a standard 3-legs IGBT based VSI inverter, whose rated peak leg current is *15 A* whereas the rated DC bus voltage is *700 V*. The DC-Link is composed of a capacitors bank with *2200μF* capacity, whereas the AC terminals are connected to the mains PCC (Point of common coupling) via three filtering inductors whose equivalent series parameters are L_f*=4.75mH*, R_f*=0.4Ω*.

The control system is composed of a main board based on a TMS320C6713® digital signal processor (DSP) clocked at 225 MHz and of an auxiliary board equipped with a ProASIC3 A3P400® field programmable gate array (FPGA) clocked at 50 MHz. The DSP and FPGA boards may be noticed on top of the prototype SAF of Figure 82, shown without the AC side inductors. To reproduce a distorted current in the grid, a non-linear load constituted by a 3-phase diode bridge rectifier supplying a resistor having a rated power P_l*=5kW* has been considered.

Experimental tests were carried out using standard supply conditions 230Vrms 50Hz. Measurements were performed using a high quality digital scope (500 MHz LeCroy 6050) and the acquisition system embedded in the DSP board, which directly transfers data to a connected host PC; spectral data were obtained by numerical post-processing.

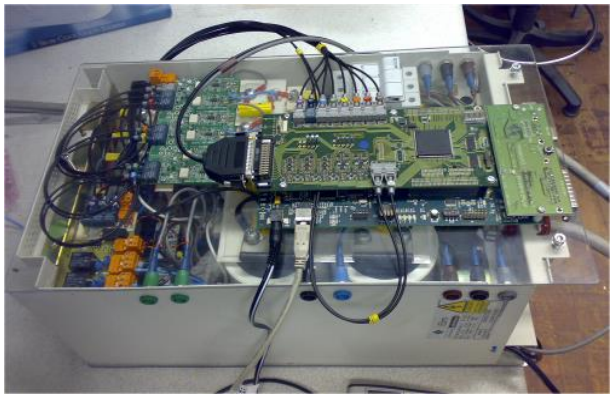

Figure 82 Top view of the experimental SAF prototype.

In order to compare the effectiveness of the proposed solution, two different MPC implementations have been tested, FCS-MPC and FCS-M2PC. The implemented control algorithm operates at fixed sampling frequency, f_s = 50kHz for the FCS-MPC and f_s = 20kHz for the FCS-M2PC. A steady-state test under full load P_l=5kW and a transient test for a 50% to 100% load variation are represented in Figure 83 for the FCS-MPC. At full power the load draws the distorted current in Figure 83 a) where the vertical axis measures 5A/div while the horizontal one 10ms/div; the mains current waveform as a consequence of SAF filtering action is shown in Figure 83 b) (5A/div) together with the mains voltage (100V/div). The SAF allows unity power factor operation and quasi sinusoidal current. However the mains current shows a superimposed high-frequency ripple due to limited number of possible control actions and the nature of the FCS-MPC control itself. The achieved benefits and therefore the effectiveness of the SAF were also confirmed in spectral terms by comparing the mains current spectrum and the load current spectrum in Figure 83 c), resulting in a reduction of THD from THD>29% to *THD<7%*, where the THD is calculated including up to the 40^{th} harmonic.

The load current during a step-up change of the rectifier load from 50% to 100% is represented in Figure 83 d) while the waveforms of mains voltage and current for

one of the phases during such transient are reported in Figure 83 e), presenting the same axis measures as Figure 83 a) and Figure 83 b). It may be noticed that the SAF exhibits a very fast dynamics with about half fundamental period to settle after the transient, hence ensuring the continuity of the compensation action. Figure 83 f) shows the DC-link voltage which demonstrates both dynamic and steady state performance with a ripple around 0.7%.

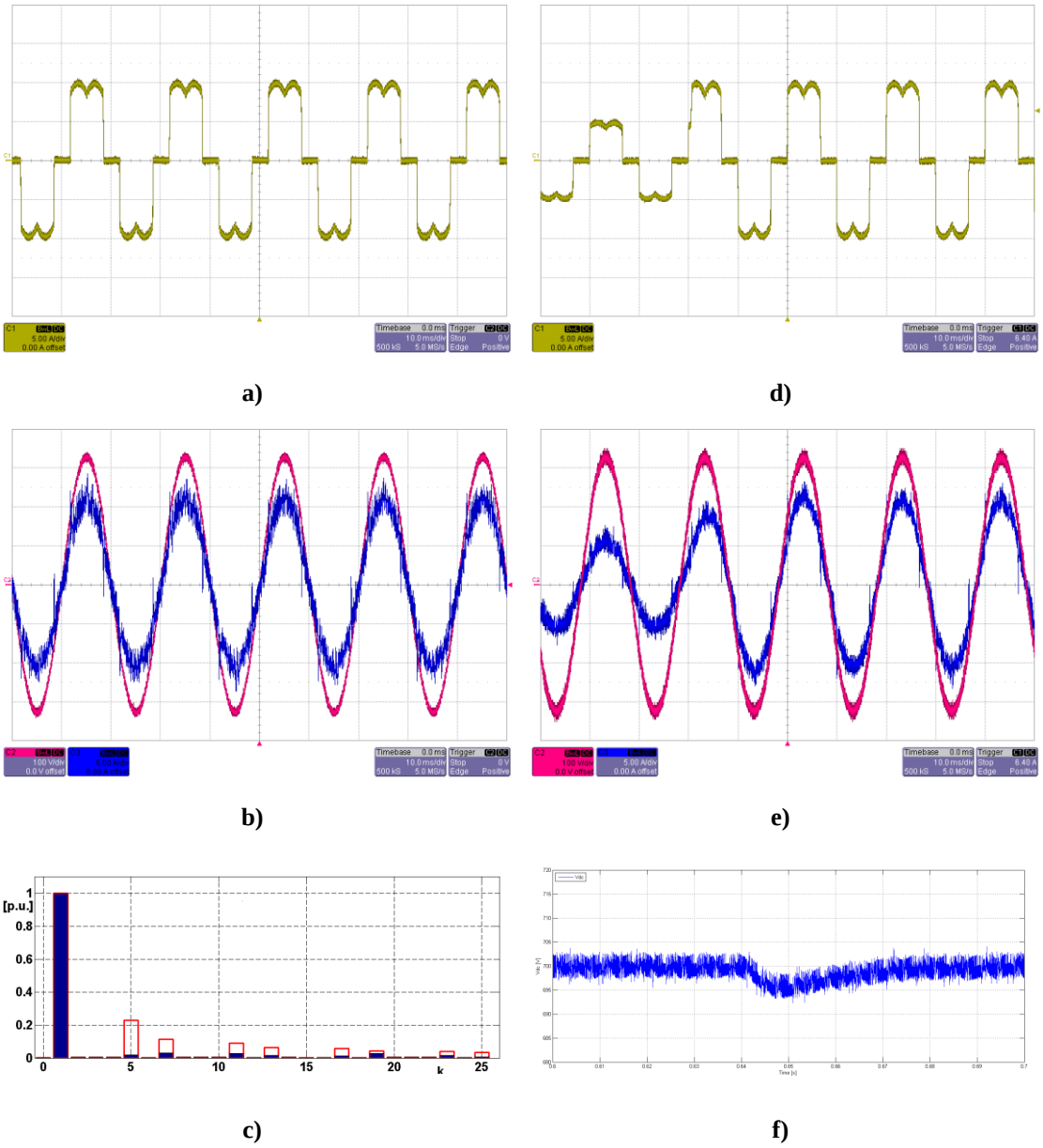

Figure 83 Steady state performance for FCS-MPC under full load [10 ms/div]:
a) Current in the nonlinear load [5V/div];
b) main currents [5A/div] and main voltage [100V/div];
c) Spectrum of currents in (a) and (b).
Transient performance for FCS-MPC during a 50% to 100% load variation [10ms/div]:

d) current in the nonlinear load [5A/div];
e) main current [5A/div] and mains voltage [100V/div];
f) DC-link voltage(700V) [5V/div].

Similar tests were performed for the M^{2}PC and are represented in Figure 84. As it can be noticed, the high frequency ripple in the main current is considerably reduced by the modulation. The performances of the M^{2}PC during the sudden changes in the load are comparable with the MPC case, but the harmonic content is slightly better Figure 84 b). It should be considered however that the sampling frequencies are different in the two cases (20KHz for the M^{2}PC and 50KHz for the MPC). The THD is reduced from 29% to less than 6% by the SAF with FCS-M^{2}PC. The performance during the load change remains good and, in overall terms, the power quality improvement achieved by means of the examined SAF results excellent, basically confirming the validity of the proposed solution and the viability of M^{2}PC for SAF control, grid synchronization structures and employing a single compact control loop regulating all system relevant quantities.

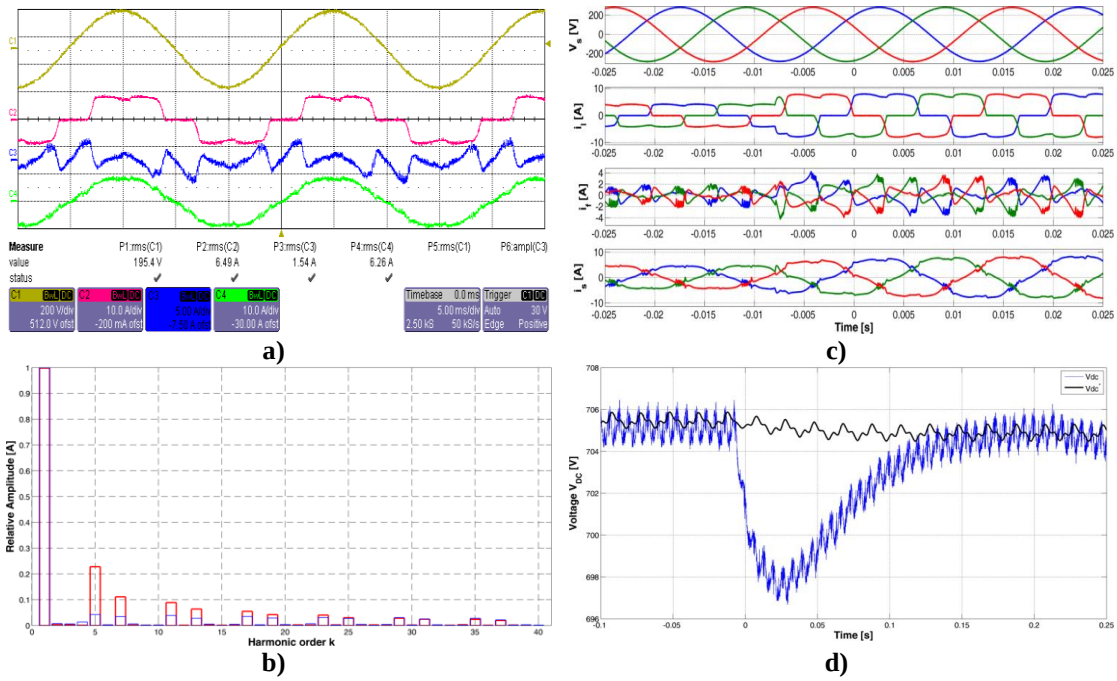

Figure 84 Steady state performance for FCS-M2PC under full load [5 ms/div]:
(a) mains voltage [200V/div], load current [10A/div], filter current [2A/div] and mains current [10A/div];
(b) Spectrum of load current (red) and mains current (blue) in (a).
Transient performance for FCS-M^{2}PC during a 50% to 100% load variation:
(c) mains voltages [200V/div], load currents [10A/div], filter currents [2A/div] and mains currents [10A/div], [5 ms/div];
(d) reference and measured DC-link voltages [2V/div], [50 ms/div].

8.7. Conclusions

Power quality control has become a critical issue in modern electrical networks. The new smart grids paradigm calls for a more dynamic, efficient and reliable distribution system where the quality of the transmitted energy is a primary feature. The use of active power compensators becomes therefore desirable and in particular active filters can be employed to reduce the impact of current harmonics on the grid itself. In this chapter, the development and the implementation of an improved Modulated Model Predictive Controller for a harmonic distortion reduction by means a SAF have been presented. It employs different predictors based on the developed system model to anticipate the values expected for various quantities considering the intrinsic control computational delay. Moreover, the higher current ripple typical of MPC has been considerably reduced by introducing a cost function-based modulation strategy without scarifying the dynamic performances. A SAF prototype implementing the FCS-MPC and the FCS-M^2PC have been described and validated. The experimental tests results, both in steady-state and transient conditions, have demonstrated that FCS-M^2PC is a viable and effective solution for the control of active power compensators, where different systems variables can be regulated with the aid of only a single control loop, with no grid synchronization devices.

Chapter 9

Conclusion and Open Issues

9.1. Conclusion

This thesis work has mainly focused on robust and model predictive control applied to DC/DC converter and shunt active filter. In particular the analyzing, modeling and control of two novel quadratic Boost converters and also, the predictive control of a shunt active filter have been proposed.

In Chapter 1, an overview about the DC/DC Boost converter applied on distributed generation systems have been given. Among the DC/DC converters, Boost topologies have attracted attention thanks to their inherent capacity to perform the maximum power point tracking. On the other hand, the traditional one-switch Boost converter reveals its limits for elevate value of boosting, since a high duty-cycle is needed. Anyway, it often cannot be adopted because of both the minimum off time of the power switch and the influence of the parasitic parameters.

In Chapter 2, among the several high gain step-up DC/DC converter topologies and the voltage boosting techniques, the class of the quadratic Boost converters has been presented. The QBCs are non-isolated single-switch topologies. They are very interesting solutions since the transformer increases cost, volume and losses. Moreover, the single-switch makes the driver a simple circuit and reduces the power losses. In this chapter, the operating principle, the ideal time domain waveforms and the design equations of two novel QBCs have been given. The *QBC1* presents a lower ripple of the input current than the *QBC2*. This feature is a benefit in the fuel cell generation because improve the reliability of the system. On the other side, the *QBC1* presents one power diode more; therefore, it has less efficiency than the *QBC2*.

In Chapter 3, the main modeling techniques of DC/DC switching converters have been presented. The SSA modeling uses the known information of the system and describes the average behavior of the system only in CCM. Usually, in order to simplify the writing of the converter equation, the power devices are assumed ideals

especially for more complex converters. Anyway, the non-linear SSA model can be used to design nonlinear model based controllers, whereas the small-signal model is used to design standard or advanced linear controllers. The analytical SSA model, the small-signal model and static gain of the two proposed QBCs have been presented. In all these analytical results, the ESR of the inductors and the capacitors has been evaluated. In the second part of the chapter, the theoretical framework of the Hammerstein model identification has been discussed. The output of the identification process is a numerical nonlinear model composed by a memory-less nonlinearity and a LTI system with unitary gain. Using the parametric identification approach, it is possible to model the power devices with its auxiliary circuits.

In Chapter 4, the Hammerstein model of the *QBC1* converter has been identified. Moreover, the comparison between the HM and SSA model of the *QBC1* converter confirms the validity of the two different modeling approaches.

In Chapter 5, the limits of the SSA modeling have been highlighted. The conclusion of the state evolution analysis is that the free evolution of the averaged model effectively represents the free evolution of the converter if and only if the product of the two dynamic matrices is commutative. Moreover, the first order approximation of the forced state evolution for the averaged model coincides with that one of the real system if the commutative property of the matrices is satisfied and the switching frequency is as smaller as possible. The commutative property of the dynamic matrices product has been investigated with negative results for the traditional Boost and the *QBC1*. All in all, the SSA model represents a good approximated averaged model of the converter if it works only in CCM.

The limits of the SSA modeling have been exceeded using the Hybrid modeling theory. Using the Hybrid formalism it is possible to obtain a general mathematical description of a switching converter. The Hybrid system theory has been successfully applied to a traditional Boost converter; the Boost Hybrid model is able to describe the continuous and discrete dynamics of the system in CCM or DCM without any constraint.

In Chapter 6, the sensitivity analysis versus parameters variation of the Boost converter, the *QBC1* and the *QBC2* has been treated. In the step-up converters, the presence of the input inductance assures a low ripple of the input current. In order to

increase the efficiency of these converters a low value of the parasitic resistance of the input inductance is desired. On the other hand, this dramatically increases the sensitivity of the static gain especially in the region of higher duty cycle, where the converter is required to be operated. The two proposed QBCs have a high sensitivity of the gain versus parameter variations for lower values of duty-cycle than the traditional Boost convert. This condition makes the control task more difficult in the case of the QBCs.

In Chapter 7, the design of a robust control law based on the SSA and HM model of the *QBC1* has been experimentally validated. The H_2 optimal robust controller is able to guarantee the voltage reference even if there are model and parameter variations. In the design of the robust controller, the use of the Hammerstein model gives better dynamics performances than the SSA model because the controller has a nonlinear gain.

In Chapter 8, the development and the implementation of an improved modulated model predictive controller for a harmonic distortion reduction by means a SAF have been presented. It employs different predictors based on the developed system model to anticipate the values expected for various quantities considering the intrinsic control computational delay. Moreover, the higher current ripple typical of MPC has been considerably reduced by introducing a cost function-based modulation strategy without scarifying the dynamic performances. A SAF prototype implementing the FCS-MPC and the FCS-M^2PC have been described and validated. The experimental tests results, both in steady-state and transient conditions, have demonstrated that FCS-M^2PC is a viable and effective solution for control of active power compensators, where different systems variables can be regulated with the aid of only a single control loop, with no grid synchronization devices.

9.2. Open Issues

In this thesis the analysis and control of two novel QBCs and, the predictive control of a shunt active filter have been illustrated. Anyway, several open problems are left as the subject of future researches. Future research will focus on: the control of a switching converter based on the Hybrid model, experimental validation of the

QBC2 in PV/WT MPPT applications, reducing of the *QBC2* input ripple using an interleaved topology plus sensor-less fault detection algorithms.

Publications by the author

International journals

[1] F. Alonge, M. Pucci, R. Rabbeni, and G. Vitale, "Identification and Robust Control of a Quadratic DC/DC Boost Converter by Hammerstein Model," *IEEE Trans. Ind. Appl.*, vol. 9994, no. c, pp. 1–1, 2015.

[2] L. Tarisciotti, A. Formentini, A. Gaeta, M. Degano, P. Zanchetta, R. Rabbeni, and M. Pucci, "Model Predictive control for Shunt Active Filters with Fixed Switching Frequency," *IEEE Trans. Ind. Appl.*, vol. 9994, no. c, pp. 1–1, 2016.

[3] F. Alonge, M. Pucci, R. Rabbeni, and G. Vitale, "Dynamic Modelling of a Quadratic DC/DC Single-Switch Boost Converter," *Electric Power System Research*, Accepted with minor revision.

International conferences

[4] R. Rabbeni, G. Vitale, G. Marsala, and M. Pucci, "Analysis and design of a dc-dc converter with high boosting and reduced current ripple for PEM FC," in *2011 IEEE Vehicle Power and Propulsion Conference, VPPC 2011*, 2011.

[5] R. Rabbeni, L. Tarisciotti, A. Gaeta, A. Formentini, P. Zanchetta, M. Pucci, M. Degano, and M. Rivera, "Finite states modulated model predictive control for active power filtering systems," in *2015 IEEE Energy Conversion Congress and Exposition, ECCE 2015*, 2015.

[6] F. Alonge, R. Rabbeni, M. Pucci, and G. Vitale, "Identification and robust control of a quadratic DC/DC boost converter by Hammerstein model," in *2014 IEEE Energy Conversion Congress and Exposition, ECCE 2014*, 2014.

[7] F. Alonge, M. Pucci, R. Rabbeni, G. Vitale, P. Facoltà, D. Energia, and M. Matematici, "Sensitivity analysis of a High Gain DC / DC boost converter including parasitic parameters," no. 12, 2014.

References

Akagi, H., 2005. The state-of-the-art of active filters for power conditioning. In *2005 European Conference on Power Electronics and Applications*. IEEE, p. 15 pp.-pp.P.15.

Alonge, F. et al., 2015. Dynamic Performance Enhancement of AC / DC PFC Boost Converters by Means of MRAS Observers. , pp.281–287.

Alonge, F., D'Ippolito, F. & Cangemi, T., 2008. Identification and robust control of dc/dc converter Hammerstein model. *IEEE Transactions on Power Electronics*, 23(6), pp.2990–3003.

Arivazhagan, R. & Prakash, S.L., 2011. Analysis of current-fed full bridge converter with modified auxiliary circuit. In *2011 INTERNATIONAL CONFERENCE ON RECENT ADVANCEMENTS IN ELECTRICAL, ELECTRONICS AND CONTROL ENGINEERING*. IEEE, pp. 357–362.

Axelrod, B., Berkovich, Y. & Ioinovici, A., 2008. Switched-capacitor/switched-inductor structures for getting transformerless hybrid DC-DC PWM converters. *IEEE Transactions on Circuits and Systems I: Regular Papers*, 55(2), pp.687–696.

Balestrino, A. et al., 2001. Automatic nonlinear auto-tuning method for Hammerstein modeling of electrical drives. *IEEE Transactions on Industrial Electronics*, 48(3), pp.645–655.

Beaty, R.C.D.M.F.M.S.S.H.W., 2004. Electrical Power Systems Quality , Second Edition. , p.525.

Bhaskar, M.S. et al., 2014. A Novel High Gain DC-DC Multilevel Boost Converter Using Voltage-Lift Switched-Inductor Cell. , (c).

Blaabjerg, F. et al., 2015. Power electronics - the key technology for renewable energy system integration. In *2015 International Conference on Renewable Energy Research and Applications (ICRERA)*. IEEE, pp. 1618–1626.

Blaabjerg, F. et al., 2006. Power Electronics in Renewable Energy Systems. In *2006 12th International Power Electronics and Motion Control Conference*. IEEE, pp. 1–17.

Buso, S., Malesani, L. & Mattavelli, P., 1998. Comparison of current control techniques for active filter applications. *IEEE Transactions on Industrial Electronics*, 45(5), pp.722–729.

Chen, S. et al., 2013. A Novel Switched-Coupled-Inductor DC-DC Step-Up Converter. , pp.1830–1833.

Chen, W.-C. et al., 2010. Current-fed DC-DC converter with ZCS for high voltage applications. In *The 2010 International Power Electronics Conference - ECCE ASIA -*. IEEE, pp. 58–62.

Choi, W. et al., 2007. Bridgeless Boost Rectifier With Low Conduction Losses and Reduced Diode Reverse-Recovery Problems. , 54(2), pp.769–780.

Choudhury, T.R. (KIIT U. & Byamakesh, N., 2015. Comparison and Analysis of Cascaded and Quadratic Boost Converter. , (5).

Ci-Ming Hong et al., 2009. Novel bidirectional DC-DC converter with high step-up/down voltage gain. In *2009 IEEE Energy Conversion Congress and Exposition*. IEEE, pp. 60–66.

Cirrincione, M. et al., 2009. Current harmonic compensation by a single-phase shunt active power filter controlled by adaptive neural filtering. *IEEE Transactions on Industrial Electronics*, 56(8), pp.3128–3143.

Cirrincione, M., Pucci, M. & Vitale, G., 2008. A Single-Phase DC Generation Unit With Shunt Active Power Filter Capability by Adaptive Neural Filtering. *IEEE Trans. Ind. Electron.*, 55(5), pp.2093–2110.

Coffa, S., Saggio, M. & Patti, A., 2016. SiC-and GaN-based power devices: Technologies, products and applications. *Technical Digest - International Electron Devices Meeting, IEDM*, 2016–Febru, p.16.8.1-16.8.5.

Cortés, P. et al., 2008. Direct power control of an AFE using predictive control. *IEEE Transactions on Power Electronics*, 23(5), pp.2516–2523.

Cortés, P. et al., 2008. Predictive control in power electronics and drives. *IEEE Transactions on Industrial Electronics*, 55(12), pp.4312–4324.

Cortés, P. et al., 2007. Predictive current control strategy with imposed load current spectrum. *EPE-PEMC 2006: 12th International Power Electronics and Motion Control Conference, Proceedings*, 23(2), pp.252–257.

Dempsey, E.J. & Westwick, D.T., 2004. Identification of Hammerstein Models with Cubic Spline Nonlinearities. *IEEE Transactions on Biomedical Engineering*, 51(2), pp.237–245.

Dionise, T. & Lorch, V., 2010. Voltage Distortion on an Electrical Distribution System. *IEEE Industry Applications Magazine*, 16(2), pp.48–55.

Elmer, T. et al., 2015. Fuel cell technology for domestic built environment applications: State of-the-art review. *Renewable and Sustainable Energy Reviews*, 42, pp.913–931.

Espí Huerta, J.M. et al., 2010. A synchronous reference frame robust predictive current control for three-phase grid-connected inverters. *IEEE Transactions on Industrial Electronics*, 57(3), pp.954–962.

Fairweather, A.J., Foster, M.P. & Stone, D.A., 2011. Battery parameter identification with Pseudo Random Binary Sequence excitation (PRBS). *Journal of Power Sources*, 196(22), pp.9398–9406.

Fang Lin Luo, 2001. Six self-lift dc-dc converters, voltage lift technique. *IEEE Transactions on Industrial Electronics*, 48(6), pp.1268–1272.

Fang Lin Luo & Hong Ye, 2003. Positive output super-lift converters. *IEEE Transactions on Power Electronics*, 18(1), pp.105–113.

Gaubert, J.-P. & Chanedeau, G., 2009. Evaluation of DC-to-DC converters topologies with quadratic conversion ratios for photovoltaic power systems. *2009 13th European Conference on Power Electronics and Applications*.

Geyer, T., Papafotiou, G. & Morari, M., 2009. Model Predictive Direct Torque Control—Part I: Concept, Algorithm, and Analysis. *IEEE Transactions on Industrial Electronics*, 56(6), pp.1894–1905.

Goebel, R., Sanfelice, R.G. & Teel, A.R., 2009. Hybrid dynamical systems. *IEEE Control Systems Magazine*, 29(2), pp.28–93.

Green, M.A. et al., 2015. Solar cell efficiency tables (Version 45). *Progress in Photovoltaics: Research and Applications*, 23(1), pp.1–9.

Haber, R. & Keviczky, L., 1999. *Nonlinear system identification : input-output modeling approach*, Kluwer Academic Publishers.

Haber, R. & Keviczky, L., 2012. *Nonlinear System Identification -- Input-output Modeling Approach Nonlinear System Parameter Identification.*, Springer Verlag.

Huber, L., Jang, Y. & Jovanović, M.M., 2008. Performance evaluation of bridgeless PFC boost rectifiers. *IEEE Transactions on Power Electronics*, 23(3), pp.1381–1390.

Hunter, I.W. & Korenberg, M.J., 1986. The identification of nonlinear biological systems: Wiener and Hammerstein cascade models. *Biological Cybernetics*, 55(2–3), pp.135–144.

Jintakosonwit, P., Fujita, H. & Akagi, H., 2002. Control and performance of a fully-digital-controlled shunt active filter for installation on a power distribution system. *IEEE Transactions on Power Electronics*, 17(1), pp.132–140.

Jurado, F., 2006. A method for the identification of solid oxide fuel cells using a Hammerstein model. *Journal of Power Sources*, 154(1), pp.145–152.

Kadri, R. et al., 2010. Performance analysis of transformless single switch quadratic boost converter for grid connected photovoltaic systems. In *The XIX International Conference on Electrical Machines - ICEM 2010*. IEEE, pp. 1–7.

Kouro, S. et al., 2009. Model Predictive Control #x2014;A Simple and Powerful Method to Control Power Converters. *Industrial Electronics, IEEE Transactions on*, 56(6), pp.1826–1838.

Kristinsson, K. & Dumont, G.A., 1992. System identification and control using genetic algorithms. *IEEE Transactions on Systems, Man, and Cybernetics*, 22(5), pp.1033–1046.

Kwan, K.H., So, P.L. & Chu, Y.C., 2007. A harmonic selective unified power quality conditioner using MVR with Kalman filters. *International Power Engineering Conference (IPEC)*, pp.332–337.

Lee, Y., Chou, Z. & Huang, S., 2013. Quadratic Boost Converter with Switched Capacitor and Coupled Inductor for PV System Applications. , (1), pp.38–43.

Leyva-Ramos, J. et al., 2009. Switching regulator using a quadratic boost converter for wide DC conversion ratios. *IET Power Electronics*, 2(5), p.605.

Li, H. & Chen, Z., 2007. Overview of different wind generator systems and their comparisons. *Renewable Power Generation, IET*, 1(1), pp.10–16.

Li, Q. & Lee, F.C., 2012. Winding AC resistance of low temperature co-fired ceramic inductor. *Conference Proceedings - IEEE Applied Power Electronics Conference and Exposition - APEC*, pp.1790–1796.

Lopez-santos, O., Martinez-salamero, L. & Member, S., 2016. Steady-State Analysis of Inductor Conduction Modes in the Quadratic Boost Converter. , 8993(c), pp.1–22.

Malesani, L., Mattavelli, P. & Buso, S., 1999. Robust dead-beat current control for PWM rectifiers and active filters. *IEEE Transactions on Industry Applications*, 35(3), pp.613–620.

Malinowski, M. et al., 2015. Optimized Energy-Conversion Systems for Small Wind Turbines: Renewable energy sources in modern distributed power generation systems. *IEEE Power Electronics Magazine*, 2(3), pp.16–30.

Mattavelli, P., 2001. A closed-loop selective harmonic compensation for active filters. *IEEE Transactions on Industry Applications*, 37(1), pp.81–89.

Miao, B., Zane, R. & Maksimovic, D., 2005. System Identification of Power Converters With Digital Control Through Cross-Correlation Methods. *IEEE Transactions on Power Electronics*, 20(5), pp.1093–1099.

Middlebrook, R.D. & Cuk, S., 1976. A general unified approach to modelling switching-converter power stages. In *Power Electronics Specialists Conference, 1976 IEEE*. pp. 18–34.

MIDDLEBROOK, R.D. & ĆUK, S., 1976. A General Unified Approach to Modelling Switching-Converter Power Stages. , 21(1), pp.3–5.

Millán, J., Godignon, P. & Pérez-Tomás, A., 2012. Wide Band Gap Semiconductor Devices for Power Electronics. *Automatika – Journal for Control, Measurement, Electronics, Computing and Communications*, 53(2), pp.107–116.

Mohan, N., Undeland, T. & Robbins, william, 1995. Mohan_Power_Electronics.pdf.

Morari, M. & Zafiriou, E., 1990. *Robust process control.*,

Moses, P.S. et al., 2010. Power quality of smart grids with Plug-in Electric Vehicles considering battery charging profile. In *2010 IEEE PES Innovative Smart Grid Technologies Conference Europe (ISGT Europe)*. IEEE, pp. 1–7.

Nava-Cruz, C. et al., 2016. Comparative study of two model-based controllers for a quadratic boost converter. , pp.132–137.

Nava-cruz, J.C. et al., 2015. Comparative evaluation of load observers for a quadratic boost converter.

de Novaes, Y.R., Rufer, A. & Barbi, I., 2007. A New Quadratic, Three-Level, DC/DC Converter Suitable for Fuel Cell Applications. In *2007 Power Conversion Conference - Nagoya*. IEEE, pp. 601–607.

O.Garcia et al., 2001. Power Factor Correction: A Survey. *Power Electronics Specialists Conference, 2001. PESC. 2001 IEEE 32nd Annual*, pp.8–13.

Papafotiou, G. et al., 2009. Model Predictive Direct Torque Control—Part II: Implementation and Experimental Evaluation. *IEEE Transactions on Industrial Electronics*, 56(6), pp.1906–1915.

Polman, A. et al., 2016. Photovoltaic materials: Present efficiencies and future challenges. *Science (New York, N.Y.)*, 352(6283), p.aad4424.

Pressman, A., 1997. *Switching Power Supply Design*, McGraw-Hill, Inc.

Püttgen, H.B., Macgregor, P.R. & Lambert, F.C., 2003. Distributed Generation: Semantic Hype or the Dawn of a New Era? *IEEE Power and Energy Magazine*, 1(1), pp.22–29.

Rabbeni, R. et al., 2011. Analysis and design of a dc-dc converter with high boosting and reduced current ripple for PEM FC. In *2011 IEEE Vehicle Power and Propulsion Conference, VPPC 2011*.

Ramakumar, R. & Chiradeja, P., 2002. Distributed generation and renewable energy systems. *IECEC 02 2002 37th Intersociety Energy Conversion Engineering Conference 2002*, pp.716–724.

Robert W., and D.M.E., 2002. *Fundamentals of Power Electronics Fundamentals of Power Electronics*,

Rodriguez, J. et al., 2007. Predictive Current Control of a Voltage Source Inverter. *IEEE Transactions on Industrial Electronics*, 54(1), pp.495–503.

Rossetto, L., Buso, S. & Spiazzi, G., 2000. Conducted EMI issues in a 600-W single-phase boost PFC design. *IEEE Transactions on Industry Applications*, 36(2), pp.578–585.

Rossetto, L., Spiazzi, G. & Tenti, P., 2000. Boost PFC with 100-Hz switching frequency providing output voltage stabilization and compliance with EMC standards. *IEEE Transactions on Industry Applications*, 36(1), pp.188–193.

Saadat, P. & Abbaszadeh, K., 2016. A Single Switch High Step up DC-DC Converter Based on Quadratic Boost. , 46(c), pp.1–9.

Salmeron, P. & Litran, S.P., 2010. Improvement of the Electric Power Quality Using Series Active and Shunt Passive Filters. *IEEE Transactions on Power Delivery*, 25(2), pp.1058–1067.

Sharaf, O.Z. & Orhan, M.F., 2014. An overview of fuel cell technology: Fundamentals and applications. *Renewable and Sustainable Energy Reviews*, 32, pp.810–853.

Singh, B., Al-Haddad, K. & Chandra, A., 1999. A review of active filters for power quality improvement. *IEEE Transactions on Industrial Electronics*, 46(5), pp.960–971.

Todeschini, G. & Emanuel, A.E., 2010. Wind energy conversion systems as active filters: design and comparison of three control methods. *IET Renewable Power Generation*, 4(4), p.341.

Uzunoglu, M. & Alam, M.S., 2007. Dynamic modeling, design and simulation of a PEM fuel cell/ultra-capacitor hybrid system for vehicular applications. *Energy Conversion and Management*, 48(5), pp.1544–1553.

Yang, H. et al., 2007. On-Chip High- Q Inductor Using Wafer-Level Chip-Scale Package Technology. , pp.3–6.

Yang, P. et al., 2012. A new quadratic boost converter with high voltage step-up ratio and reduced voltage stress. *Conference Proceedings - 2012 IEEE 7th International Power Electronics and Motion Control Conference - ECCE Asia, IPEMC 2012*, 2, pp.1164–1168.

Zahira, R. & Peer Fathima, A., 2012. A Technical Survey on Control Strategies of Active Filter for Harmonic Suppression. *Procedia Engineering*, 30, pp.686–693.

Zhang, N. et al., 2015. High-voltage-gain quadratic boost converter with voltage multiplier. *IET Power Electronics*, 8(12), pp.2511–2519.

Zhang, S., Xu, J. & Yang, P., 2012. A single-switch high gain quadratic boost converter based on voltage-lift-technique. *10th International Power and Energy Conference, IPEC 2012*, (51177140), pp.71–75.

Zmood, D.N., Holmes, D.G. & Bode, G.H., 2001. Frequency-domain analysis of three-phase linear current regulators. *IEEE Transactions on Industry Applications*, 37(2), pp.601–610.

UNIVERSITÀ
DEGLI STUDI
DI PALERMO